Study on Growth of High Quality Corundum Gallium Oxide on Sapphire Substrates

2020

Riena Jinno

Study on Growth of High Quality Corundum Gallium Oxide on Sapphire Substrates

By Riena Jinno

This thesis summarizes the study that has been conducted while the author has been in the doctoral course of the Graduate School of Engineering in Kyoto University, and was submitted for the Doctor of Engineering degree in Kyoto University.

In the thesis, a study on ultra wide-bandgap materials of metastable corundum gallium oxide (α-Ga_2O_3) is presented by exploiting its high quality growth and phase stability. The thesis is divided into seven chapters.

In chapter 1, a brief introduction of ultra wide-bandgap (UWBG) semiconductor materials and their promising characteristic as materials for power devices is given. Then, from the view point of power devices, the properties of α-Ga_2O_3 grown on sapphire is described. Especially, the advantages and issues of mist-chemical vapor deposition (mist-CVD), which has been used for the growth of α-Ga_2O_3, are reviewed, then, the necessity of the molecular beam epitaxy (MBE) growth is stressed. The purpose of this thesis is clarified by summarizing the fundamental technology to be solved toward applications of α-Ga_2O_3 based power devices.

In chapter 2, a reduction of carbon (C) impurity concentrations in mist-CVD grown α-Ga_2O_3 films is conducted. After the explanation of the mist -CVD system used in this study, properties of α-Ga_2O_3 thin film grown on sapphire substrates using gallium tri-chloride ($GaCl_3$) as a gallium precursor are shown and discussed. Dependences of growth rates of α-Ga_2O_3 films on hydrochloric acid (HCl) and growth temperatures (T_g) are investigated to reveal the reaction of forming α-Ga_2O_3. HCl enhances the growth rate by producing $GaCl^{2+}$ in the aqueous solution, leading to the maximum growth rate of 7.8 μm/h. The optimized T_g is 700 ºC (the supply limited progress), and atomic force microscopy (AFM) images shows the root-square-mean (RMS) roughness of 0.19 nm due to the high growth temperature. The impurity concentration of carbon in the film is successfully reduced below the detection limit level (1×10^{17} cm^{-3}).

In chapter 3, polymorphs of Ga_2O_3 grown on α-$(Al_xGa_{1-x})_2O_3$ is studied toward devices with a multilayer structure. When the α-$(Al_xGa_{1-x})_2O_3$ layers are annealed and the AFM images shows atomic steps, ε-Ga_2O_3 is grown on the layer at 500 ºC regardless of the Al composition x. On the other hand, α-Ga_2O_3 is obtained on the as grown

α-$(Al_xGa_{1-x})_2O_3$ layer at the same temperature. From these results, the dependence of polymorphs on surface morphology or termination is suggested. Growth temperatures higher than 700 ºC is revealed to be suitable for the growth α-Ga_2O_3 due to the longer diffusion length.

In chapter 4, an introduction of α-$(Al_xGa_{1-x})_2O_3$ graded buffer layer and epitaxial lateral overgrown (ELO) α-Ga_2O_3 are investigated aiming at the reduction of dislocation density in α-Ga_2O_3 layers. With the α-$(Al_xGa_{1-x})_2O_3$ graded buffer layer, the dislocations are concentrated in the buffer layer and the edge dislocation density is decreased nearly by two orders in magnitude. The epitaxial lateral overgrowth of α-Ga_2O_3 is demonstrated by using SiO_2 as a mask material. The selective area growth of α-Ga_2O_3 is successfully achieved at T_g>500 ºC due to longer diffusion lengths of source materials on the mask region. The ELO α-Ga_2O_3 on a-plane sapphire substrates with the stripes along m-axis shows the largest ratio of lateral and vertical growth rates (L/V ratio) of 0.96, resulting in the full coalescence. The generation of dislocations on the mask region is prevented, leading to the reduction the threading dislocation density on the center of the mask area to less than 1.6×10^7 cm^{-2}.

In chapter 5, growth of α-$(Al_xGa_{1-x})_2O_3$ on sapphire substrates is demonstrated using plasma-assisted molecular beam epitaxy (PAMBE). By using m-plane sapphire substrates, which is perpendicular to c-plane, single-phase α-$(Al_xGa_{1-x})_2O_3$ films are stabilized in the entire range of x by preventing a formation of c-plane facets, which is considered to enhance the growth of β-Ga_2O_3. Different phases/domains are not detected from both x-ray diffraction (XRD) measurement and cross-sectional scanning transmission electron microscopy (STEM) observations. However, stacking faults are observed in the α-Ga_2O_3 and Ga-rich α-$(Al_xGa_{1-x})_2O_3$ films due to the strain from the substrates having the large lattice mismatched to the films. The bandgap energy of the α-$(Al_xGa_{1-x})_2O_3$ films is in the wide range from 5.34 to 8.56 eV.

In Chapter 6, the phase stability of α-Ga_2O_3 on sapphire is explored. The phase transition temperature of α-Ga_2O_3 films to the β-phase increases as the film thickness decreases regardless of the growth conditions. The phase transition to the β-phase is revealed to be occurred from the surface of the film by transmission electron microscopy (TEM). α-Ga_2O_3 has a larger thermal expansion coefficient than sapphire, suggesting that α-Ga_2O_3 films on sapphire substrates have the tensile stress near the surface. β- Ga_2O_3 has the larger density than α- Ga_2O_3, therefore the tensile stress could convert α-Ga_2O_3 to β-Ga_2O_3.

In chapter 7, conclusions of this study and suggestions for future works are described.

Acknowledgements

During my Ph. D. life at Kyoto University, a lot of people supported and encouraged me in so many ways and I would like thank all of them here.

First of all, I would like to express my most sincere gratitude to Professor Shizuo Fujita for his continuous and attentive supervision, invaluable suggestions, and encouragement. He also taught me many skills required for a researcher and provided me opportunities to have a lot of experiences. Moreover, his passion for research has inspired me.

I am also deeply grateful to Professor Hirofumi Yamada and Associate Professor Mitsuru Funato for their careful and constructive comments and suggestions through regular discussions and refereeing my thesis. Their comments always led my work to the better direction and comprehensive study.

I have also greatly benefited from to Assistant Professor Kentaro Kaneko for his insightful comments. He also supported and gave me a lot of advice for my carrier as a researcher.

I would like to express my special gratitude to Professor Debdeep Jena for his kindness of being a host researcher for JSPS Overseas Challenge Program and invaluable discussion during my stay in Cornell University. He gave me the valuable opportunity to work on MBE, which I really wanted. Moreover, his insightful perspective based on physics has deeply impressed me. I am also grateful to Professor Huili Grace Xing for her thoughtful comments and suggestions, and attentive support for my stay.

I am very obliged to Dr. Kazuaki Akaiwa and Dr. Takayuki Uchida for their constructive suggestions and supports in my daily work. I would also like to thank Mr. Yoshito Ito, Mr. Kenta Suzuki, and Mr. Masashi Kitajima for their comments and instructing experimental procedures. I am much indebted to Dr. Yongjin Cho for his precise and valuable comments and thoughtful support for both my research and private life. If not for his help, I would not survive in Ithaca. My special thanks also goes to Dr. Vladimir Protasenko, Dr. Kazuki Nomoto for instructing experimental procedures and whole maintenance management of experimental systems. I would also thank Dr. Zongyang Hu and Mr. Wenshen Li for teaching me about device simulations. My gratitude goes to Mr. Jonathan McCandless, Mr. Vasanth Balakrishnan, Mr. Nicholas Tanen, Mr. Shao-Ting Ho, and Mr. Derek Rowe for their discussions and helps for MBE growths. I also thank Kevin Lee for conducting optical measurements.

I would thank Professor Takeyoshi Onuma for demonstrating experiments for my samples. I would also thank Dr. Yuichi Oshima for his comments and providing samples. I owe a very important debt to Ms. Celesta S. Chang for her STEM observations as a collaboration. Without her works, I would never write this thesis. Furthermore, I had a fun conversation with her about our research and daily lives.

I also would like to show my deepest gratitude to Professor Toshiyuki Kawaharamura, Assistant Professor Hiroyuki Nishinaka, Associate Professor. Takayoshi Oshima, Assistant Professor Takumi Ikenoue for their generous supports and precise comments on my research. I am also grateful to Associate Professor Kazuyuki Uno for his invaluable suggestions. With his advices, my work has progress in a good direction. My sincere gratitude goes to Assistant Professor Hironori Okumura for his valuable suggestions. I would also appreciate his kind and supportive attitude for my carrier.

Associate Professor Shigetaka Katori and his wife stopped by Ithaca and encouraged me at that time. I would appreciate their kindness.

I would like to express my gratitude to Dr. Takafumi Okuda, Dr. Mitsuaki Kaneko, Dr. Hajime Tanaka, Dr. Takuma Kobayashi, Mr. Takuya Maeda, Mr. Kazutaka Kanegae for having fruitful discussion and cheerful conversations throughout my Ph.D. life. I would also like to show my appreciation to Dr. Shuhei Ichikawa for sharing his experiences. His talk deeply impressed and encourage me a lot. My special appreciation goes to Ms. Anni Wu for her kind support in my daily life in Ithaca and sharing pleasant and precious time. I would also thank Mr. Masashi Uchida for spending a lot of time in our laboratory as well as in private.

My appreciation also goes to all of the members in our laboratory for their kindness and supports: Dr. Sam-dong Lee, Mr. Ryosuke Takagi, Mr. Shu Takemoto, Mr. Keiichi Tsumura, Mr. Masafumi Ono, Mr. Kyohei Ishii, Mr. Shinichi Kan, Mr. Yasuhisa Masuda, Mr. Nobuhiro Yoshimura, Mr. Shoma Hoshi, Mr. Hiroki Kitade, Mr. Tomoharu Akaishi, and Mr. Hitoshi Takane. I would also thank all members in Jena-Xing group.

This work was partly supported by the Japan Society for the Promotion of Science (JSPS) through the Grant-in-Aid for Research Fellow (993325) and Overseas Challenge Program for Young Researchers (1080033), the Kyoto University Foundation thorough support for international technological interaction.

Finally, I sincerely wish to thank my father, my mother, my grand-mother, and my brother, Dr. Sigeyoshi Usami, and all of my friends for their understanding, support and hurtful encouragement.

February, 2020

Riena Jinno

Contents

Chapter 1

Introduction

1.1 Background

Today, there are many things using “electricity” that exist in our daily lives as home electric appliances, transportation equipment, and so on. In late 1900’s, a lot of electrically driven products have been developed for example refrigerators, air conditioners, automobiles, and railway trains. These products have changed our lives more convenient and more comfortable. In 1960’s, personal computer appeared, which is essential for our lives now. In 2010’s, smart phone and tablet personal computer became widespread, allowing us to use internet even outside buildings. It has led to the “internet of things (IoT)” society, that is the interconnection via computing devices embedded in everyday objects, making them intelligent, programmable and capable of interacting with human. The IoT based technologies are used in manufacturing, assert management, smart homes, freight monitoring, and so on, changing what our lives are like. These developments of technologies, on the other hand, have increased the demand of electric energy.

On the other hand, energy conservation and prevention are seriously required to prevent global warming. Figure 1.1 shows the global greenhouse gas emissions from all sources. [1)] The Emission Gap Report 2019 reported that the total emissions grew 1.5 % per year in the last decade (2009 to 2018) without land-use change, reaching a record high of 55.3 $GtCO_2e^2$ in 2018. This means that the global greenhouse gas emission is still increasing and further efforts are necessary for us to reduce the emissions and save our earth. For Japan, it is required to reduce energy supply using fossil fuels. Japan are largely dependent on the fossil fuels such as oil, coal, and liguefied natural gas (LNG). Although renewable energy is increasing, the dependency of primary energy supply of Japan on the fossil fuels is 87.4 % in 2017 as shown in Fig. 1.2. [2)] Note that the dependency was 81.2 % before the Great East Japan Earthquake, which resulted in the shutdown of nuclear power plants. In order to decrease the dependency on the fossil fuels, it is necessary to save energy itself and increase the supply of renewable energy. Another important way is to improve energy consumption efficiency, which can decrease the amount of energy and reduce CO_2 emission, leading to a solution to global warming as well. Improving energy efficiency means that we can use

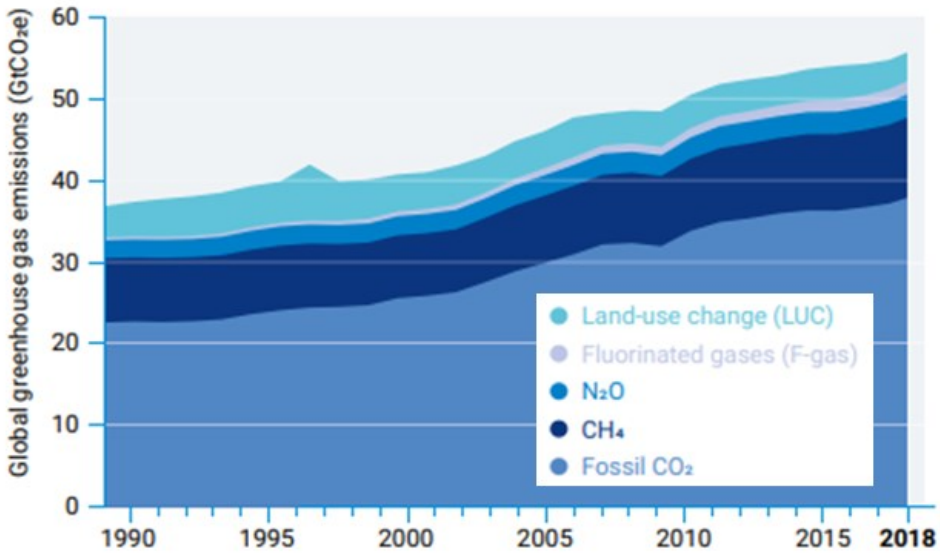

Figure 1.1. Global greenhouse gas emissions from all sources. [1)]

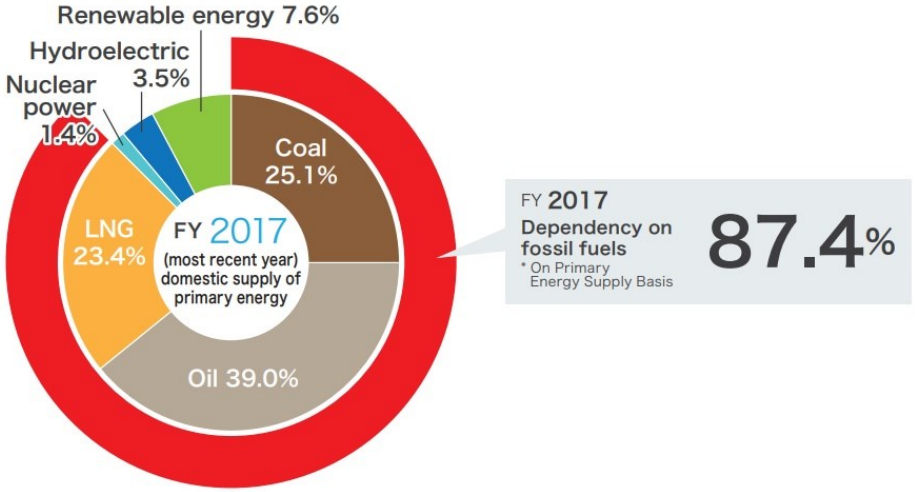

Figure 1.2. Composition of Primary Energy Supply of Japan in 2017. [2)]

more energy by the same amount of energy source, allowing us to continue our convenient and comfortable lives with approaching the problem of global warming.

Most energy is consumed as electric energy, therefore, it is especially important to enhance the efficiency of electric energy. The loss of electric energy is mainly produced during power conversion; electric power is transmitted from power plants to us through several power conversions by reducing high voltage generated in the plants to a certain voltage we want to use. In order to reduce the energy loss during the power conversions, semiconductor power devices have been playing an important role. The power devices allow power conversion by utilizing switching and rectifying functions of semiconductor materials, leading to high conversion efficiency. This technology is widely used in a lot of

applications; power transmission, railway trains, electric vehicles, home appliances such as air conditioners and refrigerators, AC adaptors, PCs, and many other electric devices. Therefore, the performance of the power devices is crucial for energy saving, and much effort has been mad to enhance the efficiency of the power devices. Power devices are also utilized to amplify powers of high-frequency signal inputs, which is essential for the development of advanced information society.

1.2 Ultra-Wide Bandgap Semiconductors

1.2.1 Wide Bandgap Materials

Silicon (Si) and gallium arsenide (GaAs) have been widely used as materials of power devices and have helped energy saving. However, performance of these devices is approaching to their physical limits of materials and we have paid much attentions to power devices based on wide bandgap (WBG) semiconductor materials such as silicon carbide (SiC) and gallium nitride (GaN). [3,4] Table 1.1 shows the basic properties of various compound semiconductor single crystals. [5] "Figures of Merit" (FOM) is widely used to evaluate the potential of materials although a single FOM cannot capture all aspects of device performance. Baliga FOM (BFOM) is defined as $\varepsilon\mu E_c^3$ for low frequency based on on-state loss, and μE_c^2 for high frequency based on sum of on-state loss and switching loss,

Table 1.1. Basic physical properties of various compound semiconductor single crystals. [5]

		Si	SiC	GaN	β-Ga_2O_3	α-Ga_2O_3
Bandgap E_g (eV)		1.1	3.3	3.4	4.5	5.3
Electron mobility μ ($cm^2/V\cdot s$)		1400	1000	1200	300	300 (estimation)
Breakdown electric field E_c (MV/cm)		0.3	2.5	3.3	7	10 (estimation)
Relative permittivity ε_s		11.6	9.7	9.0	10	10 (estimation)
Thermal conductivity (W/cm·K)		1.5	4.9	1.3	0.14	-
Baliga figure of merit Si =1	Low frequency ($\varepsilon\mu E_c^3$)	1	340	870	2307	6726 (estimation)
	High frequency (μE_c^2)	1	50	104	117	238 (estimation)

where ε is the permittivity, μ is the electron mobility, and E_c is the critical electric field. This FOM increases as the cube or square root of E_c, therefore, materials with larger E_c tend to show higher FOM. Materials with larger bandgaps experimentally have larger E_c, resulting in high FOM of WBG materials. As shown in Table 1.1, SiC and GaN show high FOM and can achieve significant performance improvement by replacing Si-based devices.

1.2.2 Ultra-Wide Bandgap Materials

As the WBG semiconductor-based devices have been explored and commercialized, the next generation of semiconductor materials has been expected at the following research stage; a new category was born in 2015, that is so-called "ultra" wide-bandgap (UWBG) materials that have bandgaps larger than that of GaN (E_g>3.4 eV). [6,7] Figure 1.3 shows the relationship between energy bandgap and bond length for various semiconductor materials where the UWBG materials are located in the region painted orange. Representative semiconductor materials in this category include aluminum nitride (AlN), diamond (C) and gallium oxide (Ga_2O_3). The borderline between semiconductor and insulator has shifted to the higher energy-side and now AlN is the semiconductor with the largest bandgap energy of ~6 eV. However, Ga_2O_3 allows bandgap engineering to ~8.8 eV by alloying with Al_2O_3, indicating the potential of a power device with the highest electric energy efficiency, although electric conductivity of the $(Al,Ga)_2O_3$ alloy is currently being researched.

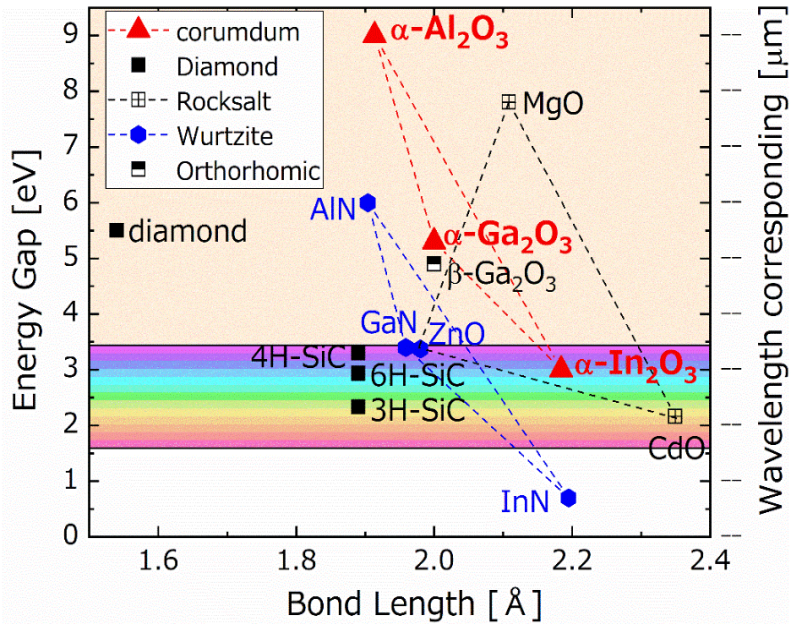

Figure 1.3. Relationship between energy bandgap and bond length for various compound semiconductors. The region of ultra-wide bandgap materials is drawn in orange.

1.3 Gallium Oxide

Ga_2O_3 has bandgap of around 5 eV, [8] and is expected to have much larger BFOM than those of SiC and GaN as described in Table 1.1. These estimates indicate the potential of Ga_2O_3 for high-power and high-voltage device applications. In addition, alloying with Al_2O_3 and In_2O_3 allows bandgap engineering from around 3 to 8.8 eV. Therefore, heterostructure devices are possible such as modulation-doped electron channels, quantum wells, and superlattices in the In_2O_3-Ga_2O_3-Al_2O_3 alloy system.

Ga_2O_3 takes five different polymorphs; corundum (α), monoclinic (β), defective spinel (γ), bixbite (δ), and orthorhombic (ε). The summary of synthesis and interconversion of the polymorphs of Ga_2O_3 and related phases is shown Fig. 1.4. [9] Note that ε-Ga_2O_3 with the space group *Pna2*$_1$ is sometimes called κ-Ga_2O_3 in the literature. Among the five different polymorphs of Ga_2O_3, the β-gallia structure is the thermodynamically most stable phase, while the others are metastable and convert to the β-phase upon heating at 500-700 ºC. Most studies on Ga_2O_3 are related to the β-Ga_2O_3 because high quality β-Ga_2O_3 free-standing substrates are available by several melting methods, [10–17] leading to demonstrations of both lateral and vertical devices using the homoepitaxial growth of β-Ga_2O_3.[18–24] Recently a formation of high mobility two-dimensional electron gas (2DEG) at β-$(Al_xGa_{1-x})_2O_3$/Ga_2O_3 interface has been reported through modulation doping and delta-doping using plasma-assisted molecular beam epitaxy (PAMBE). [25,26] As described above, the promising results have already been reported for the most stable β-Ga_2O_3.

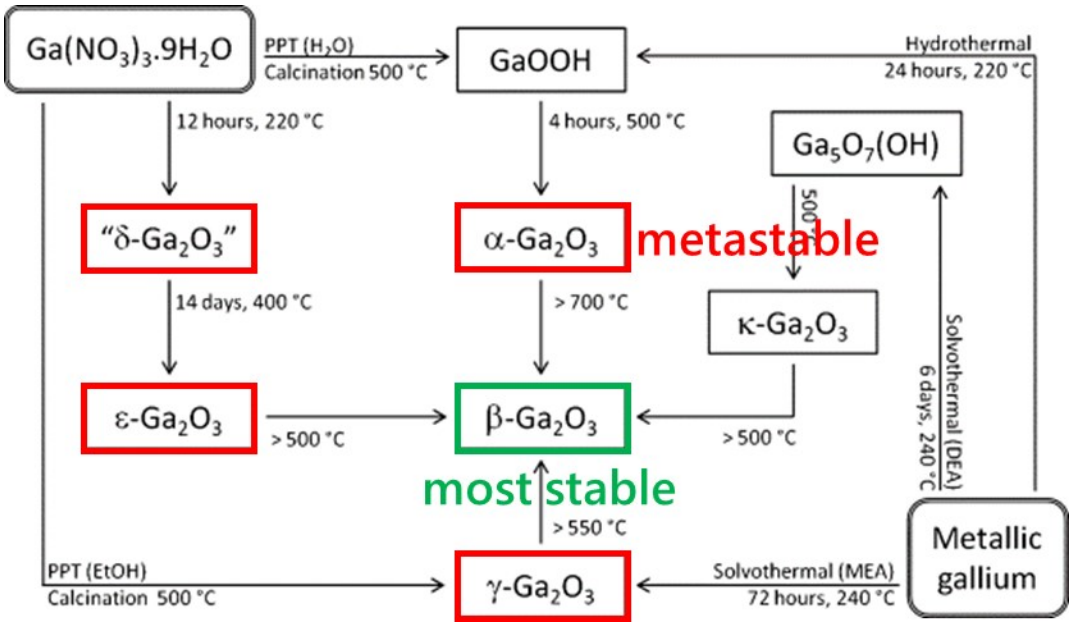

Figure 1.4. The interconversion of the polymorphs of Ga_2O_3 and related phases. [9]

On the other hand, the metastable phases such as α- and ε-phases have attracted much interests due to their unique characters in the recent years. ε-Ga_2O_3 is expected to have pyroelectric properties and large spontaneous polarization (0.23 C/m^2) as calculated by the Berry-phase approach. [27] Experimental results of dynamic hysteresis measurements show the presence of ferroelectricity of ε-Ga_2O_3 as well. [28] These properties suggest applications of human body sensors as well as high frequency devices. In this study, the author focuses on the α-phase and the detail will be described in the next section.

1.4 Corundum Gallium Oxide (α-Ga_2O_3)

The bandgap energy of α-Ga_2O_3 has been reported to be 5.3-5.6 eV, [29,30] while those of the other phases are in the range of 4.6-4.9 eV. The larger bandgap is an important physical property to achieve high power devices as explained in section 1.2. The greatest advantage of α-Ga_2O_3 is its good miscibility with Al_2O_3 and the bandgap engineering in the wide range of 5.6-8.8 eV by alloying with Al_2O_3. The ground-state crystal structures of Ga_2O_3 and Al_2O_3 are the monoclinic (β) and corundum (α), respectively. The difference of the most stable phases results in the solubility limit of Al_2O_3 in β- and ε-Ga_2O_3 while α- and γ-$(Al_xGa_{1-x})_2O_3$ are epitaxially grown in the entire range of x without a phase separation.[31–33] The highest Al contents of $(Al_xGa_{1-x})_2O_3$ epitaxial films are reported to be x~0.7 (E_g~6.1 eV) for the β-phase, [34] and x~0.65 (estimated E_g~6.5 eV) for the ε-phase.[35,36] Although γ-$(Al_xGa_{1-x})_2O_3$ are controlled in the entire range of x, the bandgap of γ-Al_2O_3 is as small as 6.97 eV, [33] which is 2 eV smaller than that of α-Al_2O_3 (E_g~8.8 eV). By forming an α-Ga_2O_3/$(Al_xGa_{1-x})_2O_3$ heterointerface, the large valence band offset of 3.24 eV has been predicted due to the large bandgap of α-Al_2O_3. [37] In face, the valence band offsets of 2.7 and 1.87 eV have been experimentally reported for α-Ga_2O_3/Al_2O_3 and α-Ga_2O_3/$(Al_{0.2}Ga_{0.8})_2O_3$ heterointerfaces as determined by X-ray photoelectron spectroscopy (XPS). [38,39] The large band offset suggests a potential of higher charge density 2DEG at the α-$(Al_xGa_{1-x})_2O_3$/Ga_2O_3 heterointerface with a higher breakdown voltage than the other materials.

1.5 Growth Methods of α-Ga_2O_3

Since α-Ga_2O_3 does not have its free-standing substrate yet, sapphire (α-Al_2O_3) substrates, which has the same corundum structure (α-phase), has been used to grow the epitaxial film of α-Ga_2O_3. Single-crystalline α-Ga_2O_3 films are successfully grown on sapphire substrates using mist chemical vapor deposition (CVD) [29,40–42] and halide vapor phase epitaxy (HVPE). [43–45] Recently, Chen *et al.* reported the growth of α-Ga_2O_3 on

nonpolar ZnO $(11\bar{2}0)$ substrates by the laser molecular beam epitaxy (MBE) technique.[46] In the following part, the author shows the features and current status of mist-CVD, HVPE, MBE and metal organic chemical vapor deposition (MOCVD), which are mainly used as the growth techniques for α-Ga_2O_3.

1.5.1 Mist-CVD

Interestingly, the epitaxial growth of α-Ga_2O_3 has been demonstrated on c-plane sapphire substrates for the first time using the mist-CVD method.[29] The schematic of the hot-wall type mist-CVD system is displayed in Fig. 1.5. A liquid solution including source materials is atomized by an ultrasonic vibrator and mist particles are transferred with the carrier and dilution gases to a substrate where a film is grown basically by a CVD mechanism on the substrate. In this system, the growth is usually operated under atmospheric pressure without a vacuum equipment. Therefore, the mist-CVD method is a safe, cost-effective, and low-energy-consumption growth method especially suitable for the growth of oxide materials since atmospheric oxygen is not treated as a severe contamination unlike the growth of II-VI and nitride materials. Gallium (III) acetyleacetonate [$Ga(C_5H_7O_2)_3$)] is generally used as a Ga precursor, which is dissolved in a deionized (DI) water or a mixed solution of a DI water and a methanol. Oxygen of Ga_2O_3 is originated from the DI water or $Ga(C_5H_7O_2)_3$, but it has not been clearly revealed yet.

Doping and alloy are available simply by dissolving source materials together and concentrations are controlled by the molar ratio to Ga in the source solution. α-$(Al,Ga,In)_2O_3$ can be grown by adding aluminum (III) acetyleacetonate [$Al(C_5H_7O_2)_3$)]

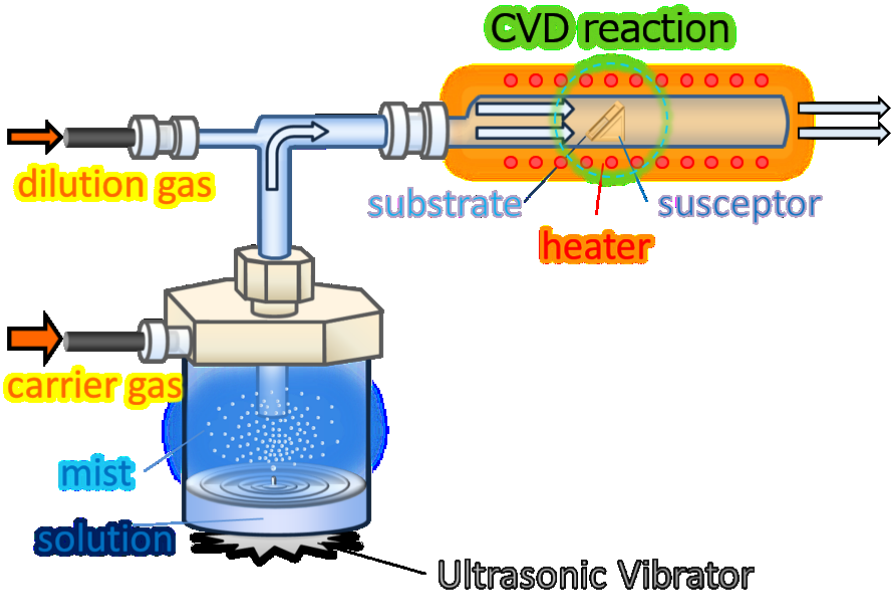

Figure 1.5. Schematic of a hot-wall type mist-CVD system.

and Indium (III) acetyleacetonate [$In(C_5H_7O_2)_3$)].[31,47] The α-$(Al_xGa_{1-x})_2O_3$ films has been grown on c-plane sapphire in the entire range of x without a phase separation, showing optical bandgap engineering from 5.3-8.8 eV.[31] n-type conductivity control is possible by doping donor impurity such as Sn, Si and Ge.[40,42,48,49] Akaiwa *et al.* reported the control of carrier concentration in the range of 10^{17}-10^{19} cm^{-3} by doping Sn with the maximum hall mobility of 24 cm^2/V s (n=2×10^{18} cm^{-3}) for c-plane and 65 cm^2/V s (n=1.2×10^{18} cm^{-3}) for m-plane. [50] Si-doped α-Ga_2O_3 has showed larger mobility of 31.5 cm^2/V s (n=3×10^{18} cm^{-3}) for c-plane reported by Uchida *et al*. [49]

By using acetyleacetonate precursors, the promising results has been achieved, as described above. However, the precursor including carbon (C) resulted in the high C impurity concentrations of 1×10^{19} cm^{-3} in the α-Ga_2O_3 film. [40] In addition, the threading dislocation density in the α-Ga_2O_3 film has been reported to be as high as 7×10^{10} cm^{-2} [51] due to the large mismatches to sapphire (3.54 and 4.81% along c- and a-axes, respectively).

1.5.2 HVPE

The structural quality of HVPE-grown α-Ga_2O_3 is similar to that of a mist-CVD-grown film, but the tilt angle tends to be larger (~100 arcsec) probably because of the unoptimized nucleation process. [43] A plane-view transmission electron microscopy (TEM) observation revealed that the dislocation density of the order of 10^{10} cm^{-2} in the α-Ga_2O_3 film grown on c-plane sapphire. [52] The largest advantage of HVPE growth is high growth rate exceeding 100 μm/h.[43] n-type conductivity control is possible by doping donor impurities, such as Ge. The electron mobility of a Ge-doped α-Ga_2O_3 film has been reported to be as high as 28 cm^2/V s when n =3×10^{19} cm^{-3}. [53]

1.5.3 MBE and MOCVD

In the studies on the growth of II-VI and III-V compound materials, MBE and MOCVD are dominant growth methods, providing high quality layers with excellent control of purity, uniformity, composition, and interface. The two epitaxial growth methods are used in the studies on the growth of β-Ga_2O_3 as well. On the other hand, the growth of α-Ga_2O_3 by these methods is still at the stage of investigating growth condition to grow single-phase α-Ga_2O_3. As shown in Fig.1.6, β-Ga_2O_3 has been reported to grow on the top of a three-monolayer-thick psuedomorphically grown layer of α-Ga_2O_3 on c-plane sapphire. [54] However, the growth of α-Ga_2O_3 by MBE and MOCVD are necessary to control composition and interface precisely and further study is desired.

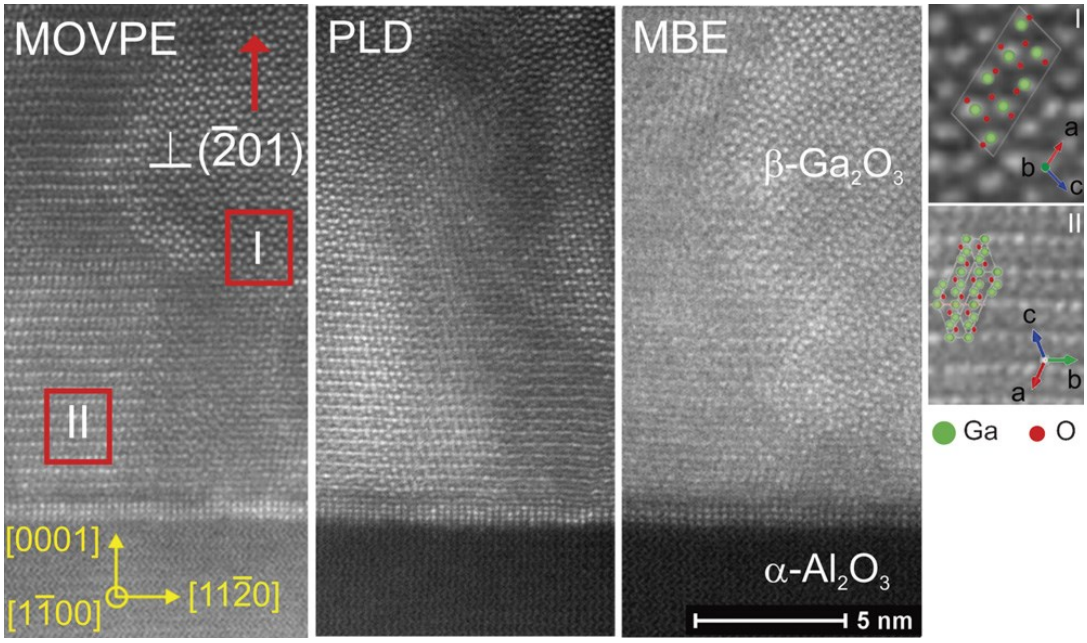

Figure 1.6. STEM HAADF images of typical β-Ga_2O_3 layers grown on c-plane sapphire substrates by MOCVD, PLD and MBE. Between the β-Ga_2O_3 layer and the sapphire, a three-atomic-layer thick interlayer of α-Ga_2O_3 is visible. [54)]

1.6 Aims and Outline of This Thesis

α-Ga_2O_3 has the advantage for high power heterostructure devices as described above. However, the study on α-Ga_2O_3 is still at the initial stage and there are several issues to be studied and solved. Most of the issues arise from the its metastable characteristic: control of polymorphs and high dislocation density in the epitaxial film related to the heteroepitaxial growth on foreign substrates, and the low thermal stability. α-Ga_2O_3 does not have its high-quality free-standing substrate and requires the growth on foreign substrates such as sapphire. The heteroepitaxial growth of α-Ga_2O_3 on sapphire substrates results in difficulty of controlling polymorphs and high dislocation densities of 10^{10} cm^{-2} in the α-Ga_2O_3 layer due to the large lattice mismatches (3.54 and 4.81% along c- and a-axes, respectively). [51)] As explained in Section 1.5, mist-CVD is a promising method for the growth of α-Ga_2O_3, but the mist-CVD grown α-Ga_2O_3 films have high impurity concentrations such as C induced by the source materials and atmospheric condition. Furthermore, the MBE and MOCVD growth of α-Ga_2O_3 films is worth studying in view of the importance of sharp heterointerfaces toward heterojunction device applications. The largest issue to be discussed is its thermal stability. In order to develop α-Ga_2O_3-based power devices, these problems have to been solved. In this study, the author aimed at the

growth of high quality α-Ga_2O_3 on sapphire substrates. Here, "high quality" is including "control of polymorphs", "low dislocation density", "low impurity concentration", and "high thermal stability".

This thesis is organized as follows:

Chapter 2. Growth of α-Ga_2O_3 film using $GaCl_3$ Precursor by Mist-CVD

Chapter 2 deals with the mist-CVD growth of α-Ga_2O_3 using $GaCl_3$ as a Ga precursor aiming at eliminating the C impurity in the α-Ga_2O_3 film. It presents the growth rate as a function of growth temperature and HCl/Ga concentrations in the source to discuss reactions for the formation of α-Ga_2O_3. Structural properties are characterized using x-ray diffraction (XRD) and atomic force microscopy (AFM). Impurity concentrations in the α-Ga_2O_3 films are studied by secondary ion mass spectrometry (SIMS) and their origins are discussed.

Chapter 3. Control of Crystal Structure of Mist-CVD grown α-Ga_2O_3 by α-$(Al_xGa_{1-x})_2O_3$ Layers

Chapter 3 focus on the control of the crystal phase of mist-CVD grown α-Ga_2O_3 on α-$(Al_xGa_{1-x})_2O_3$ layers. Dependence of polymorphs of Ga_2O_3 on growth temperature, surface morphology and Al contents of α-$(Al_xGa_{1-x})_2O_3$ layers are investigated using, AFM, XRD and transmission electron microscopy (TEM).

Chapter 4. Reduction of Dislocation Density in α-Ga_2O_3 films

Chapter 4 presents studies on reduction of dislocation densities in α-Ga_2O_3 films on sapphire substrates. Two ways are applied: quasi-graded α-$(Al_xGa_{1-x})_2O_3$ buffer layers and epitaxial lateral overgrowth technique. Detailed characterizations of epitaxial layers are given using XRD, TEM and secondary electron microscope (SEM).

Chapter 5. Growth of α-Ga_2O_3 and α-$(Al_xGa_{1-x})_2O_3$ on Sapphire Substrates by Plasma-Assisted Molecular Beam Epitaxy

Chapter 5 describes the growth of α-$(Al_xGa_{1-x})_2O_3$ by PAMBE. Aiming at the growth of single-α-phase Ga_2O_3 by PAMBE, m-plane sapphire is adopted as a substrate. Structural properties are discussed by characterizations of XRD, AFM and STEM. Optical bandgaps of the α-$(Al_xGa_{1-x})_2O_3$ films are obtained by transmittance measurement.

Chapter 6. Phase Transition Temperature of α-Ga_2O_3 Film on Sapphire Substrate

Chapter 6 discusses the phase transition temperature to the β-phase of α-Ga_2O_3 films grown on sapphire substrates. Film thickness dependence of the phase transition temperature is clarified. Detailed properties are discussed using XRD and TEM.

Chapter 7. Conclusion

Finally, the conclusion of the work is presented in Chapter 7. Subject to be investigated in the future study will also be discussed.

References

1) "*Emissions Gap Report 2019,"* United Nations Environment Programme*,* Nov 27, 2019.
2) "JAPAN'S ENEGY 2019", Ministry of Economy, Trade and Industru Agency for Natural Resources and Enegy, Jan 13, 2020.
3) T. Kimoto, Jpn. J. Appl. Phys. **54**, 040103 (2015).
4) S. Fujita, Jpn. J. Appl. Phys. **54**, 030101 (2015).
5) T. Shinohe, Chem. TIMES **254**, 8 (2019).
6) R.J. Kaplar, A.A. Allerman, A.M. Armstrong, M.H. Crawford, J.R. Dickerson, A.J. Fischer, A.G. Baca, and E.A. Douglas, ECS J. Solid State Sci. Technol. **6**, Q3061 (2017).
7) S. Fujita, M. Oda, K. Kaneko, and T. Hitora, Jpn. J. Appl. Phys. **55**, 1202A3 (2016).
8) S.J. Pearton, J. Yang, P.H. Cary, F. Ren, J. Kim, M.J. Tadjer, and M.A. Mastro, Appl. Phys. Rev. **5**, 011301 (2018).
9) H.Y. Playford, A.C. Hannon, E.R. Barney, and R.I. Walton, Chem. - A Eur. J. **19**, 2803 (2013).
10) N. Ueda, H. Hosono, R. Waseda, and H. Kawazoe, Appl. Phys. Lett. **70**, 3561 (1997).
11) E.G. Víllora, K. Shimamura, Y. Yoshikawa, K. Aoki, and N. Ichinose, J. Cryst. Growth **270**, 420 (2004).
12) N. Suzuki, S. Ohira, M. Tanaka, T. Sugawara, K. Nakajima, and T. Shishido, Phys. Status Solidi **4**, 2310 (2007).
13) E.G. Víllora, K. Shimamura, Y. Yoshikawa, T. Ujiie, and K. Aoki, Appl. Phys. Lett. **92**, 202120 (2008).
14) H. Aida, K. Nishiguchi, H. Takeda, N. Aota, K. Sunakawa, and Y. Yaguchi, Jpn. J. Appl. Phys. **47**, 8506 (2008).
15) Y. Tomm, P. Reiche, D. Klimm, and T. Fukuda, J. Cryst. Growth **220**, 510 (2000).
16) Z. Galazka, R. Uecker, K. Irmscher, M. Albrecht, D. Klimm, M. Pietsch, M. Brützam, R. Bertram, S. Ganschow, and R. Fornari, Cryst. Res. Technol. **45**, 1229 (2010).
17) A. Kuramata, K. Koshi, S. Watanabe, Y. Yamaoka, T. Masui, and S. Yamakoshi, Jpn. J. Appl. Phys. **55**, 1202A2 (2016).
18) M. Higashiwaki, K. Sasaki, A. Kuramata, T. Masui, and S. Yamakoshi, Appl. Phys. Lett. **100**, 013504 (2012).
19) M. Higashiwaki, K. Sasaki, T. Kamimura, M. Hoi Wong, D. Krishnamurthy, A. Kuramata, T. Masui, and S. Yamakoshi, Appl. Phys. Lett. **103**, 123511 (2013).
20) K. Konishi, K. Goto, H. Murakami, Y. Kumagai, A. Kuramata, S. Yamakoshi, and M. Higashiwaki, Appl. Phys. Lett. **110**, (2017).

21) M.H. Wong, C.-H. Lin, A. Kuramata, S. Yamakoshi, H. Murakami, Y. Kumagai, and M. Higashiwaki, Appl. Phys. Lett. **113**, 102103 (2018).
22) M.H. Wong, Y. Nakata, A. Kuramata, S. Yamakoshi, and M. Higashiwaki, Appl. Phys. Express **10**, 041101 (2017).
23) Z. Hu, K. Nomoto, W. Li, Z. Zhang, N. Tanen, Q.T. Thieu, K. Sasaki, A. Kuramata, T. Nakamura, D. Jena, and H.G. Xing, Appl. Phys. Lett. **113**, 122103 (2018).
24) W. Li, Z. Hu, K. Nomoto, R. Jinno, Z. Zhang, T.Q. Tu, K. Sasaki, A. Kuramata, D. Jena, and H.G. Xing, in *2018 IEEE Int. Electron Devices Meet.* (IEEE, 2018), pp. 8.5.1-8.5.4.
25) S. Krishnamoorthy, Z. Xia, C. Joishi, Y. Zhang, J. McGlone, J. Johnson, M. Brenner, A.R. Arehart, J. Hwang, S. Lodha, and S. Rajan, Appl. Phys. Lett. **111**, 023502 (2017).
26) Y. Zhang, A. Neal, Z. Xia, C. Joishi, J.M. Johnson, Y. Zheng, S. Bajaj, M. Brenner, D. Dorsey, K. Chabak, G. Jessen, J. Hwang, S. Mou, J.P. Heremans, and S. Rajan, Appl. Phys. Lett. **112**, 173502 (2018).
27) M.B. Maccioni and V. Fiorentini, Appl. Phys. Express **9**, 041102 (2016).
28) F. Mezzadri, G. Calestani, F. Boschi, D. Delmonte, M. Bosi, and R. Fornari, Inorg. Chem. **55**, 12079 (2016).
29) D. Shinohara and S. Fujita, Jpn. J. Appl. Phys. **47**, 7311 (2008).
30) A. Segura, L. Artús, R. Cuscó, R. Goldhahn, and M. Feneberg, Phys. Rev. Mater. **1**, 024604 (2017).
31) H. Ito, K. Kaneko, and S. Fujita, Jpn. J. Appl. Phys. **51**, 100207 (2012).
32) R. Kumaran, T. Tiedje, S.E. Webster, S. Penson, and W. Li, Opt. Lett. **35**, 3793 (2010).
33) T. Oshima, Y. Kato, M. Oda, T. Hitora, and M. Kasu, Appl. Phys. Express **10**, 051104 (2017).
34) B.W. Krueger, C.S. Dandeneau, E.M. Nelson, S.T. Dunham, F.S. Ohuchi, and M.A. Olmstead, J. Am. Ceram. Soc. **99**, 2467 (2016).
35) P. Storm, M. Kneiß, A. Hassa, T. Schultz, D. Splith, H. von Wenckstern, N. Koch, M. Lorenz, and M. Grundmann, APL Mater. **7**, 111110 (2019).
36) D. Tahara, H. Nishinaka, S. Morimoto, and M. Yoshimoto, Appl. Phys. Lett. **112**, 152102 (2018).
37) H. Peelaers, J.B. Varley, J.S. Speck, and C.G. Van de Walle, Appl. Phys. Lett. **112**, 242101 (2018).
38) T. Uchida, R. Jinno, S. Takemoto, K. Kaneko, and S. Fujita, Jpn. J. Appl. Phys. **57**, 040314 (2018).
39) T. Oshima, Y. Kato, E. Kobayashi, and K. Takahashi, 7 (2018).
40) K. Akaiwa and S. Fujita, Jpn. J. Appl. Phys. **51**, 070203 (2012).

41) T. Kawaharamura, G.T. Dang, and M. Furuta, Jpn. J. Appl. Phys. **51**, 040207 (2012).
42) K. Akaiwa, K. Kaneko, K. Ichino, and S. Fujita, Jpn. J. Appl. Phys. **55**, 1202BA (2016).
43) Y. Oshima, E.G. Víllora, and K. Shimamura, Appl. Phys. Express **8**, 055501 (2015).
44) D.-W. Jeon, H. Son, J. Hwang, A.Y. Polyakov, N.B. Smirnov, I. V. Shchemerov, A. V. Chernykh, A.I. Kochkova, S.J. Pearton, and I.-H. Lee, APL Mater. **6**, 121110 (2018).
45) A.Y. Polyakov, N.B. Smirnov, I. V. Shchemerov, E.B. Yakimov, V.I. Nikolaev, S.I. Stepanov, A.I. Pechnikov, A. V. Chernykh, K.D. Shcherbachev, A.S. Shikoh, A. Kochkova, A.A. Vasilev, and S.J. Pearton, APL Mater. **7**, 051103 (2019).
46) X. Chen, Y. Xu, D. Zhou, S. Yang, F. Ren, H. Lu, K. Tang, S. Gu, R. Zhang, Y. Zheng, and J. Ye, ACS Appl. Mater. Interfaces **9**, 36997 (2017).
47) N. Suzuki, K. Kaneko, and S. Fujita, J. Cryst. Growth **364**, 30 (2013).
48) M. Oda, R. Tokuda, H. Kambara, T. Tanikawa, T. Sasaki, and T. Hitora, Appl. Phys. Express **9**, 021101 (2016).
49) T. Uchida, K. Kaneko, and S. Fujita, MRS Adv. **3**, 171 (2018).
50) K. Akaiwa, K. Ota, T. Sekiyama, T. Abe, T. Shinohe, and K. Ichino, Phys. Status Solidi **1900632**, 1900632 (2020).
51) K. Kaneko, H. Kawanowa, H. Ito, and S. Fujita, Jpn. J. Appl. Phys. **51**, 020201 (2012).
52) Y. Oshima, K. Kawara, T. Shinohe, T. Hitora, M. Kasu, and S. Fujita, APL Mater. **7**, 022503 (2019).
53) E. Ahmadi and Y. Oshima, J. Appl. Phys. **126**, 160901 (2019).
54) R. Schewski, G. Wagner, M. Baldini, D. Gogova, Z. Galazka, T. Schulz, T. Remmele, T. Markurt, H. von Wenckstern, M. Grundmann, O. Bierwagen, P. Vogt, and M. Albrecht, Appl. Phys. Express **8**, 011101 (2015).

Chapter 2

High Purity α-Ga_2O_3 Thin Films Grown by Mist-CVD Using a $GaCl_3$ Precursor

2.1 Introduction

The growth of single-crystalline α-Ga_2O_3 films on sapphire substrates has been reported using the mist chemical vapor deposition (CVD) method,[1–7] which is a safe, simple, cost-effective, and environmentally friendly growth method. Gallium(III) acetylacetone [$Ga(C_5H_7O_2)_3$], that is also referred to as $Ga(acac)_3$, has been used as a gallium (Ga) precursor for the growth of α-Ga_2O_3 by the mist-CVD method. Although $Ga(acac)_3$ is a safe and water-soluble material, 15 carbon (C) atoms are included in the compound [Fig. 2.1(a)], resulting in the high impurity C concentration of about 10^{19} cm^{-3} in the α-Ga_2O_3 film.[2] C-related deep levels in GaN have been reported to cause the free-carrier compensation, which is responsible for the semi-insulating behavior of GaN film. [8,9] In the study on β-Ga_2O_3, C impurities have been predicted to be a shallow donor as simulated by the self-consistent hybrid functional approach.[10] On the other hand, C was found to be a deep DX-like center, as calculated by a *post hoc* band-edge correction.[11] Both cases are not preferable to control the electric conductivity of samples since shallow donors induce high background charge concentration and deep DX centers lead to Fermi-level pinning and compensation. The similar results are expected for α-Ga_2O_3 as well and the reduction of the C impurities is required. In this chapter, the author reports the growth of α-Ga_2O_3 thin films on sapphire substrates using the C-free gallium (III) tri-chloride ($GaCl_3$) source [Fig. 2.1(b)], aiming at eliminating the C impurity in the film. The origin of the other impurities is also discussed.

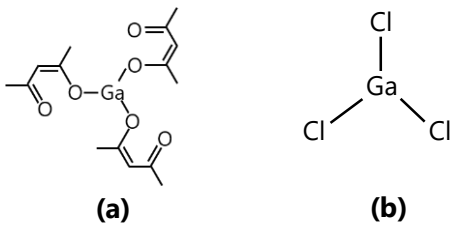

Figure 2.1. Structures of (a) gallium (III) acetylacetonate and (b) gallium tri-chloride.

2.2 Experimental Procedures

Ga_2O_3 thin films were grown on c-, a-, and r-plane sapphire substrates by the mist CVD method. $GaCl_3$ and deionized (DI) water (H_2O) were adopted as gallium and oxygen sources. The purity of the $GaCl_3$ precursor used in this study was 4N-5N. Hydrochloric acid (HCl) was used to enhance reactions of forming Ga_2O_3. $GaCl_3$ was dissolved in a mixed solution of DI water and HCl. Inert nitrogen (N_2) was used as both carrier and dilution gases. Dependences on the molar ratios of Ga ($GaCl_3$) [Ga] and HCl [HCl] in the source solution, and the growth temperature (T_g) were investigated.

2.3 Dependence on Growth Temperature

α-Ga_2O_3 films were grown on c-plane sapphire substrates at T_g between 500 and 800 ºC to investigate the T_g dependence. Note that T_g is the thermocouple temperature monitoring the outer wall of the quartz tube in the hot-wall type mist-CVD system. The simulating experiment revealed that T_g is about 100 ºC lower than a surface temperature of a sample. The growth condition is summarized in Table 2.1. The HCl concentration in the source was set at 0.18 mol/L, which was the same as that used for the $Ga(C_5H_7O_2)_3$ precursor. Film thicknesses and growth rates of the samples were in the ranges of 72-100 nm and 2.4-3.3 nm/min, respectively.

Figure 2.2 shows symmetry X-ray diffraction (XRD) 2θ/ω scan profiles in a logarithm scale for the α-Ga_2O_3 films as a function of T_g. Cu $K\alpha_1$ radiation (λ= 1.5406 Å) was used for the XRD analysis in this thesis. The dashed line lies in the theoretical position of the diffraction peak from α-Ga_2O_3 0006 (2θ= 40.2429º).[12] The profile exhibits that single-α-phase Ga_2O_3 films are obtained at the growth temperatures between 500 and 800 °C, although α-Ga_2O_3 has been reported to convert to β-Ga_2O_3 upon heating at atmospheric pressure at around 600 °C. [13–16] In the previous reports, the inclusion of β-phase was seen at the growth temperatures above 550 °C when $Ga(C_5H_7O_2)_3$ was used as

Table 2.1. Experimental conditions

Ga precursor	$GaCl_3$
Solvent	H_2O
HCl	0.18 mol/L
Ga concentration	0.125 mol/L
Growth temperature T_g	500-800 ºC
Carrier gas (flow rate)	N_2, 3.0 or 5.0 L/min
Dilution gas (flow rate)	N_2, 0.5 L/min

the gallium precursor, [1] almost agreeing with the phase transition temperature of 600 °C. However, the author has found that the phase transition temperature to the β-phase of α-Ga_2O_3 films grown on sapphire substrates depends on the film thicknesses: the phase transition temperature increases as the film thickness decreases. When the film thickness is in the range of 72-100 nm (this study), the α-Ga_2O_3 film can maintain the corundum (α) phase heating up to 680 ºC, which is expected to correspond to the growth temperature of 780 ºC, resulting in the growth of the α-Ga_2O_3 films at above 650 ºC in this chapter. The detail will be explained in Chapter 6.

For T_g≤575 ºC, the diffraction peak from α-Ga_2O_3 0006 is located on the red line, suggesting the films are completely relaxed. On the other hand, for T_g≥600 ºC, the α-Ga_2O_3 0006 reflex appears at 2θ/ω=40.19 (T_g=600 ºC), 40.15 (T_g=700 ºC), and 40.16º (T_g=800 ºC), which are slightly lower than the ideal position of 40.2429º. This indicates that the α-Ga_2O_3 films are not completely relaxed and subject to a slightly in-plane compressive stress when T_g is higher than 600 °C.

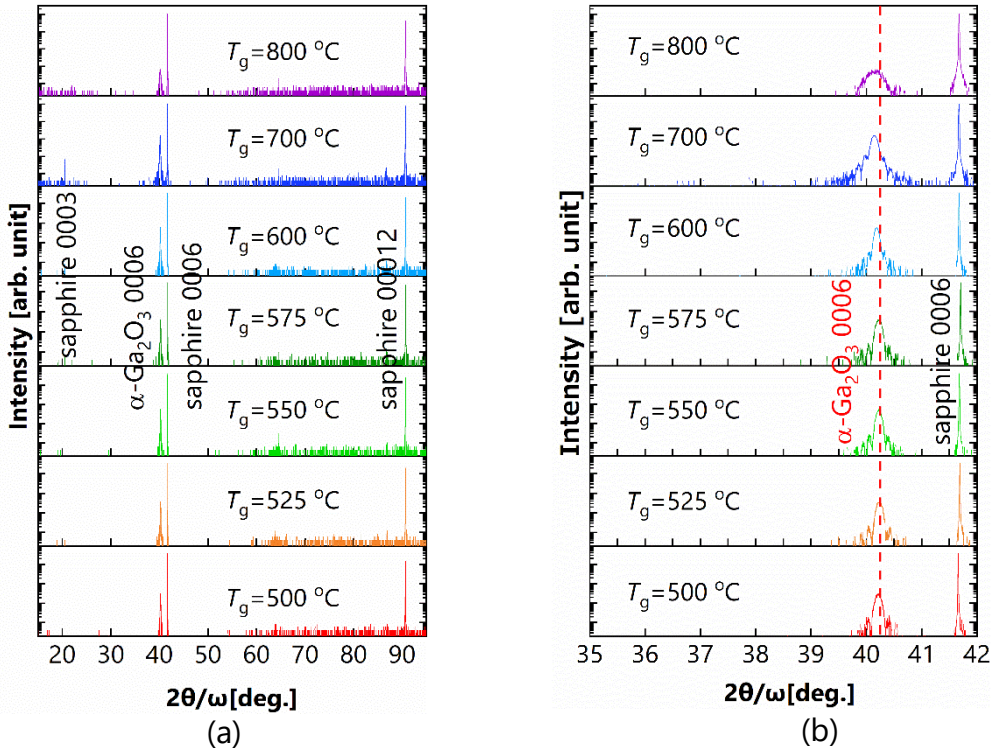

Figure 2.2. Symmetric XRD 2θ/ω scan profiles for the α-Ga_2O_3 films grown on c-plane sapphire substrates as a function of growth temperatures (T_g) shown in (a) wide and (b) narrow 2θ/ω ranges.

Figures 2.3(a)-(g) are surface atomic-force microscope (AFM) images of the α-Ga_2O_3 films grown at the growth temperature between 500 and 800 °C. When the growth temperature is lower than 600 ºC, grain sizes increase and the root mean square (RMS) roughness becomes smaller with increasing T_g. On the other hand, α-Ga_2O_3 films grown at T_g≥600 ºC have smooth surface morphologies without small grains [Fig. 2.3(e)-(f)]. The improvement of the surface morphology suggests that the diffusion length becomes longer as the growth temperature increases. The sample grown at 700 °C shows the smallest RMS roughness of 0.19 nm and atomic steps [Fig. 2.3(f)]. When the growth temperature is 800 °C,

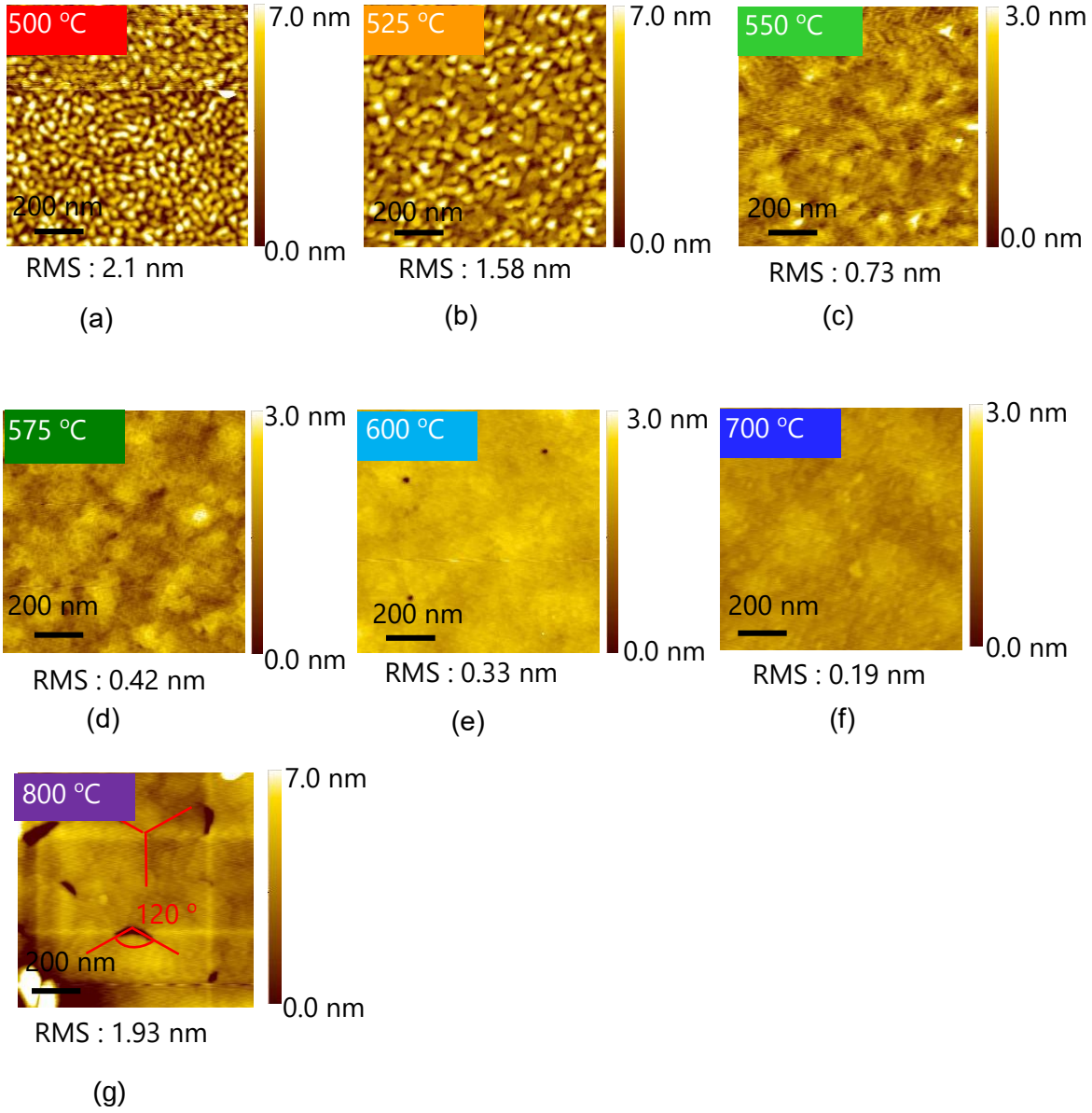

Figure 2.3. Surface AFM images of the α-Ga_2O_3 films grown on c-plane sapphire substrates as a function of growth temperatures. The growth temperatures are (a) 500, (b) 525, (c) 550, (d) 575, (e) 600, (f) 700, and (g) 800 ºC.

clacks are observed in the AFM image due to the difference of the thermal expansion coefficients between the film and substrate [Fig. 2.3(g)]. The angle between the clacks are 120°, which is derived from the three-fold symmetry of corundum structure. Although the cracks are introduced into the film, the XRD 2θ/ω scan profile revealed that the sample was still subject to the in-plane compressive stress. The α-Ga_2O_3 films grown at T_g≥600 ºC might not be completely relaxed since the higher growth temperatures slightly suppress the introduction of misfit dislocations at the interface between the film and substrate.

2.4 Dependence on HCl and Ga Molar Concentrations in Source Solution

In order to discuss the effect of HCl on the reactions for the formation of α-Ga_2O_3, growth rates of α-Ga_2O_3 films were investigated by changing [HCl] and [Ga] in the source solution. The growth conditions are summarized in Table 2.2. Figure 2.4(a) shows the growth rates of the α-Ga_2O_3 films grown at 600 and 700 ºC as a function of [HCl] in the source solution. The growth rate for T_g=700 ºC is higher than that for T_g=600 ºC at the entire range of [HCl] investigated. The difference arises from the reaction limit and this will be explained in Section 2.5. The growth rate for both T_g monotonically increases with the increase of [HCl], saturating around 2.4 mol/L. In this study, the source solution includes $GaCl_3$, H_2O and HCl. Aqueous solutions of gallium(III) salts has been reported to contain the hydrated gallium ion, $[Ga(H_2O)_6]^{3+}$.[17] When [HCl] was set at 0.18 mol/L, the growth rate was as low as 2.4-3.3 nm/min as shown in Section 2.3, suggesting that $[Ga(H_2O)_6]^{3+}$ does not contribute the formation of Ga_2O_3 and other gallium complexes seems to be composed by adding HCl, leading to the increase of the growth rate. $GaCl^{2+}$ could be the complex formed in the condition with HCl. The stability constant for the formation of $GaCl^{2+}$ in an aqueous solution has been reported to be $[GaCl^{2+}]/[Ga^{3+}][Cl^-]=1.02 \pm 0.05$ L/mol.[18] $[GaCl^{2+}]$, $[Ga^{3+}]$, and $[Cl^-]$ show the molar

Table 2.2. Experimental condition

Ga precursor	$GaCl_3$
Solvent	H_2O
HCl concentration [HCl]	0.6-3.6 mol/L
Ga concentration [Ga]	0.025-0.2mol/L
Growth temperature T_g	500-800 ºC
Carrier gas (flow rate)	N_2, 4.0 L/min
Dilution gas (flow rate)	N_2, 0.5 L/min

concentrations of $GaCl^{2+}$, Ga^{3+}, and Cl^- in the aqueous solution, respectively. The blue solid line in Fig. 2.4(a) depicts the calculated [$GaCl^{2+}$] as a function of the HCl concentration based on the stability constant. Here, HCl is assumed to be completely ionized. The calculated [$GaCl^{2+}$] increases with increasing [HCl] and the trends of [$GaCl^{2+}$] agree well with those of the growth rates of α-Ga_2O_3, indicating that the composition of $GaCl^{2+}$ yields to the formation of Ga_2O_3. From these results, HCl enhances the growth rate of α-Ga_2O_3 by forming $GaCl^{2+}$ in the solution. The larger [$GaCl^{2+}$] at lower HCl concentrations at [Ga] of 0.1 mol/L is observed probably because other equilibrium reactions are not taken into the account as well as chemical vapor reactions to form α-Ga_2O_3.

When the HCl concentration is set at 2.4 mol/L, the growth rates for T_g=600 and 700 ºC increase in proportion to the Ga concentration as shown in Fig. 2.4(b). The maximum growth rate reaches 7.8 μm/h when the growth temperature is 700 ºC, which is limited by the atomization process of the ultrasonic vibrators in the mist-CVD system; high concentrations of $GaCl_3$ and HCl make the source solution heavy and the atomization difficult, resulting in less supply of the sources and the reduction of the growth rate. This can be solved by improving the mist-CVD system in future.

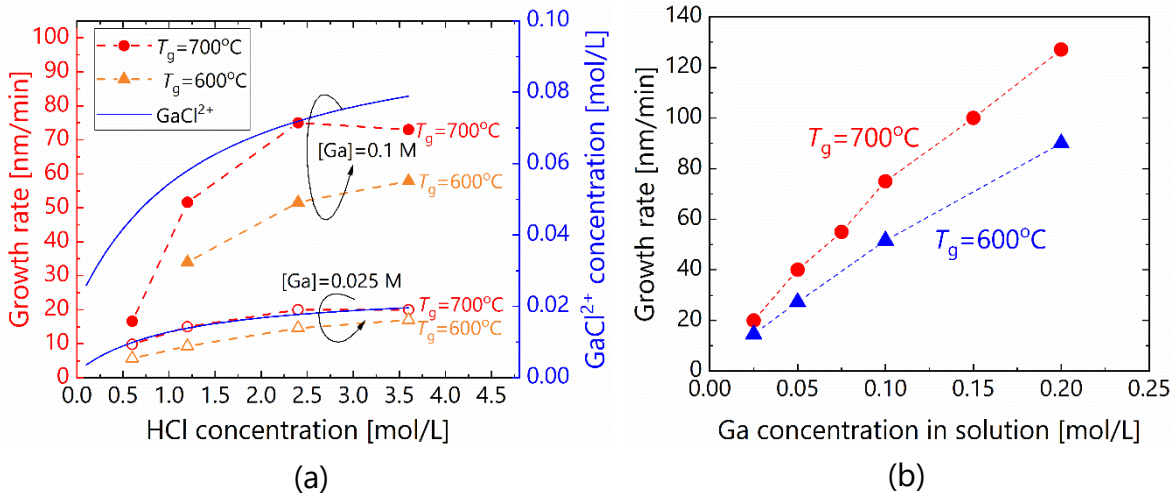

Figure 2.4. Growth rates as functions of the molar concentrations of (a) HCl and (b) Ga in the source solution. The blue solid line in (a) shows the calculated $GaCl^{2+}$ molar concentration. The HCl concentration was 2.4 mol/L for the samples shown in (b).

2.5 Dependence on Growth Temperature

When [HCl] and [Ga] are set at 2.4 and 0.10 mol/L, respectively, the growth temperature dependence of the growth rate shows the typical limited progresses of the CVD

reactions as shown in Fig. 2.5(a): (I) desorption (T_g>757 ºC), (II) supply limited (757≥T_g≥700 ºC), (III) reaction limited i (700>T_g≥650 ºC), and (IV) reaction limited ii (T_g<650 ºC). The growth rate is limited by the supply of the precursors when the growth temperature is between 700 and 757 ºC (II) while the desorption causes the decrease of the growth rate at higher than 757 ºC (I). The origin of the reaction limited-progress i (III) and ii (IV) could be the formation of gallium mono-chloride (GaCl) and $GaCl_3$, respectively. In this study, $GaCl_3$, H_2O, HCl and innert N_2 were used for the growth of α-Ga_2O_3. In Section 2.4, the contribution of $GaCl^{2+}$ to the formation of Ga_2O_3 was explained. $GaCl^{2+}$ is considered to turn into a gaseous phase just before the reaction at the substrates and can exit as GaCl and $GaCl_3$ by equilibrium reaction with HCl or Cl_2 gases. Therefore, the formation of the α-Ga_2O_3 in this system can be occurred as following reactions;

$$2GaCl\ (g) + 3H_2O\ (g) = Ga_2O_3\ (s) + 2HCl\ (g) + H_2\ (g) \quad (1)$$

$$2GaCl_3\ (g) + 3H_2O\ (g) = Ga_2O_3\ (s) + 2Cl_2\ (g) \quad (2)$$

(g) and (s) show the states of gas and solid. Nomura *et al.* has reported that for the reactions for the formation of β-Ga_2O_3, the equilibrium constant for Eq. (1) is larger than that for Eq. (2). [19] The differences in Helmholtz free energy between α- and β-Ga_2O_3 has been reported to be between 0.1-0.15 eV in the temperature range of 0-1400 K, suggesting that α-Ga_2O_3 has the similar trend of the equilibrium constants.[20] Therefore, the reaction for Eq. (1) can be mainly applied to the growth of α-Ga_2O_3. Oshima *et al.* has reported that the calculated partial pressure of $GaCl_3$ decreased with increasing temperature, while that of

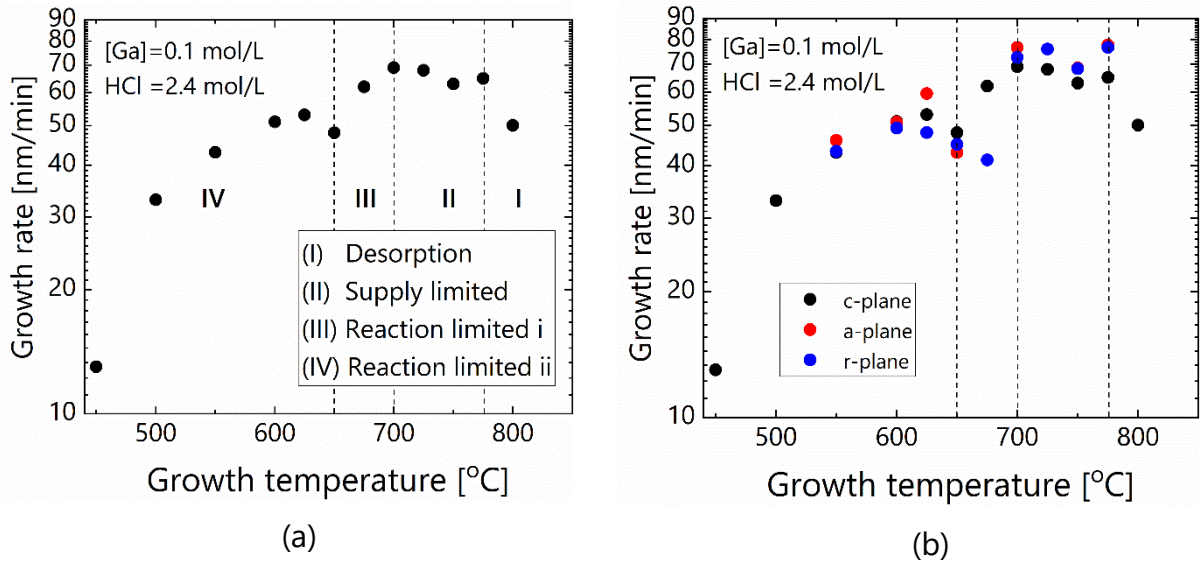

Figure 2.5. Growth rates as a function of growth temperatures for α-Ga_2O_3 grown on (a) c-plane and (b) a- and r-plane sapphire substrates. The Ga and HCl molar concentrations were 0.1 and 2.4 mol/L, respectively.

GaCl rose with temperature between 250 and 500 °C in the equilibria Ga+HCl=GaCl+1/2H_2 and GaCl+2HCl=$GaCl_3$+H_2. [21] Although the condition is different from that of this study, the reaction-limited progress ii (IV) is predicted to originate from the coverage of $GaCl_3$.

α-Ga_2O_3 films grown on a- and r-plane sapphire substrates show the same growth rate as the samples grown on c-plane sapphire substrates, indicating the progresses arises from the reaction of the source materials [Fig.2.5(b)].

2.6 Impurity Concentrations

In order to analyze the impurity concentration in the α-Ga_2O_3 films grown using the $GaCl_3$ source, the samples were subjected to secondary ion mass spectroscopy (SIMS) measurements. The $GaCl_3$ and HCl molar concentrations in the source solution were 0.1 and 2.4 mol/L. Figures 2.6(a)-(c) show the atomic densities of typical impurities [(a)

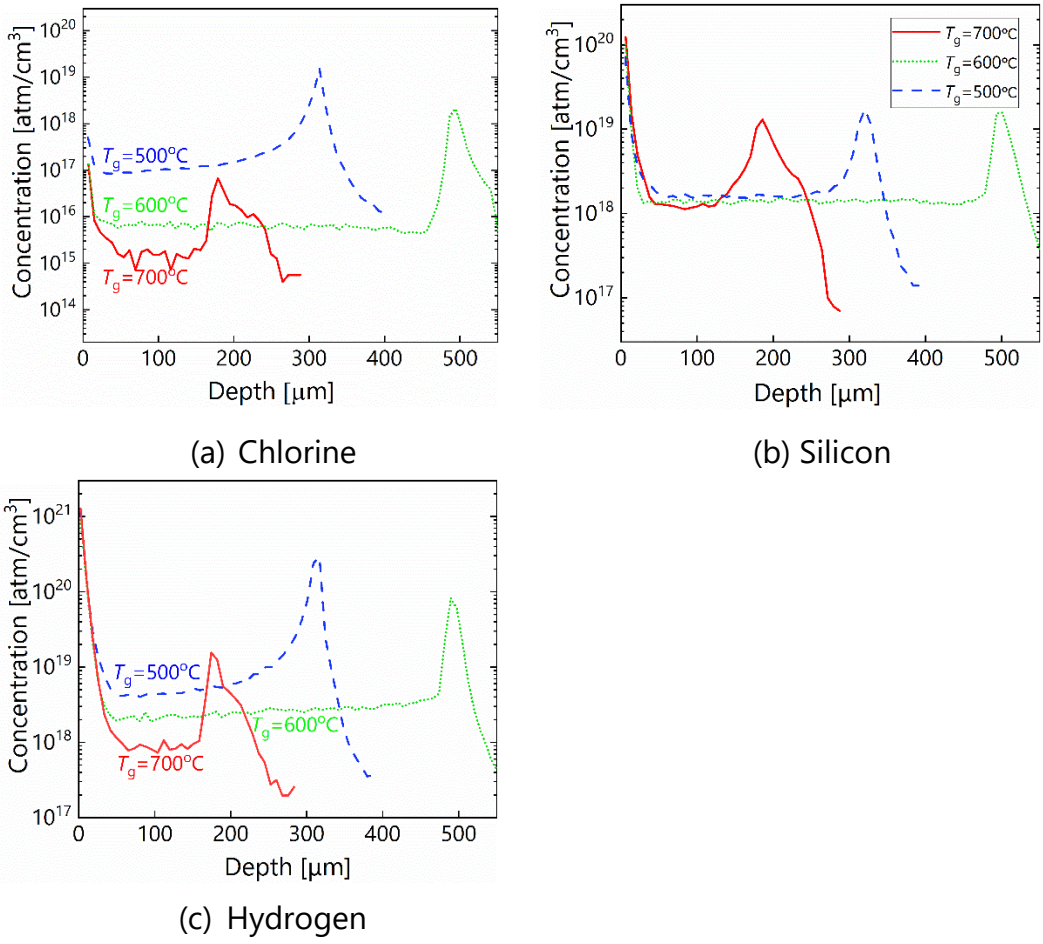

Figure 2.6. SIMS profiles on α-Ga_2O_3 films grown on c-plane sapphire at 500, 600 and 700 ºC. (a) Chlorine, (b) Silicon and (c) Hydrogen.

chloride (Cl), (b) silicon (Si) and (c) hydrogen (H)] along the depth direction in the α-Ga_2O_3 films grown on c-plane sapphire substrates at T_g=500, 600, and 700 °C. Table 2.3 summarizes the main impurity concentrations in these films and the mist-CVD grown α-Ga_2O_3 film using the $Ga(acac)_3$ precursor,[2)] and HVPE grown sample.[21)] As the growth temperature increases, the concentrations of Cl and H decrease. Despite using the HCl concentration of 2.4 mol/L, which is 24 times as high as that of the Ga source, the Cl impurity concentration is lower than the detection limit (10^{15} cm^{-3}) for T_g=700 °C, which is more than an order of magnitude lower than that in the HVPE grown sample. This is becuase the growth by HVPE used the growth temperature lower than 575 °C due to the rough morpholgies and the inclusion of the β-Ga_2O_3. The H concentration is decreased to 8×10^{17} cm^{-3} by increasing T_g, but the further effort to reduce hydrogen is required. On the other hand, the concentration of silicon impurity does not depend on the growth temperature. Si is included in the quartz tube, bottle and the $GaCl_3$ precursor (1 ppb). In general, the concentration of the Si impurity from the quartz tube depends on the growth temperature. Therefore, the residual Si in the α-Ga_2O_3 films arises from the source materials or N_2 gas. The α-Ga_2O_3 films are insulating, although the α-Ga_2O_3 films show the high concentration of Si, which can act as a shallow donor. This may be because the residual Si in the α-Ga_2O_3 films is interstitial and Si does not replace a Ga site. The SIMS measurement revealed that the concentrations of carbon impurity in the samples were reduced from 10^{19} cm^{-3} to the background level (<10^{17} cm^{-3}).

Table 2.3. Growth temperature dependence of impurity concentrations in the α-Ga_2O_3. The table refers to the impurity concentration in the α-Ga_2O_3 films grown by mist-CVD using the $Ga(acac)^3$ precursor, [2)] and by HVPE. [21)]

	Si	**H**	**C**	**Cl**
***T*g=500 ºC**	2×10^{18}	4×10^{18}	<DL(1×10^{17})	1×10^{17}
***T*g=600 ºC**	2×10^{18}	3×10^{18}	<DL(1×10^{17})	9×10^{15}
***T*g=700 ºC**	2×10^{18}	8×10^{17}	<DL(1×10^{17})	<DL (1×10^{15})
Ga(acac)3	1×10^{19}	2×10^{19}	1×10^{19}	-
HVPE	1×10^{16}	<DL(4×10^{17})	<DL(6×10^{17})	7×10^{16}

2.7 Summary

The author has demonstrated the growth of α-Ga_2O_3 by the mist-CVD method using $GaCl_3$ as a Ga precursor aiminng at elimination of residual C in α-Ga_2O_3 films. α-Ga_2O_3 was epitaxially grown on c-, a-, and r-plane sapphire substrates at the growth temperature between 500 and 800 ºC. The high growth temperature of 700 ºC enhanced the diffusion length, leading to the smooth surface morphology with the RMS roughness of 0.19 nm. The growth rate increased with the increase of the HCl concentration in the solusion, showing the maximum growth rate of 130 nm/min (7.8 μm/h) and the minimum growth rate of around a few nm/min. The wide range of the growth rate is preferable to control the heterointerface precisely as well as to grow thick template layers. The supply limited-progress was observed when the growth temperature was between 700 and 757 ºC. The C impurity concentration was succesfully decreased to the detection limit. The α-Ga_2O_3 grown at 700 ºC (the supply limited region) showed the lowest impurity concentration of H and Cl. However, the high Si impurity concentration of 2×10^{18} cm^{-3} remains to be solved. From the dependence on the growth temperature, the residual Si is likely to arise from source materials or N_2 gas, not from the quartz cube. By using purified materials, it will be solved in the future works. It is also necessary to study the electric conductivity of the α-Ga_2O_3 using the $GaCl_3$ precurosr and understand the role of the residual impurities.

References

1) D. Shinohara and S. Fujita, Jpn. J. Appl. Phys. **47**, 7311 (2008).
2) K. Akaiwa and S. Fujita, Jpn. J. Appl. Phys. **51**, 070203 (2012).
3) K. Akaiwa, K. Kaneko, K. Ichino, and S. Fujita, Jpn. J. Appl. Phys. **55**, 1202BA (2016).
4) R. Jinno, T. Uchida, K. Kaneko, and S. Fujita, Appl. Phys. Express **9**, 071101 (2016).
5) T. Kawaharamura, G.T. Dang, and M. Furuta, Jpn. J. Appl. Phys. **51**, 040207 (2012).
6) T. Uchida, K. Kaneko, and S. Fujita, MRS Adv. **3**, 171 (2018).
7) T. Kawaharamura, Dang, Giang T., and N. Nitta, Appl. Phys. Lett. **109**, 151603 (2016).
8) X.M. Shen, D.G. Zhao, Z.S. Liu, Z.F. Hu, H. Yang, and J.W. Liang, Solid. State. Electron. **49**, 847 (2005).
9) A. Armstrong, A.R. Arehart, D. Green, U.K. Mishra, J.S. Speck, and S.A. Ringel, J. Appl. Phys. **98**, 053704 (2005).
10) J.L. Lyons, D. Steiauf, A. Janotti, and C.G. Van de Walle, Phys. Rev. Appl. **2**, 064005 (2014).
11) S. Lany, APL Mater. **6**, 046103 (2018).

12) M. Marezio and J.P. Remeika, J. Chem. Phys. **46**, 1862 (1967)
13) R. Roy, V.G. Hill, and E.F. Osborn, J. Am. Chem. Soc. **74**, 719 (1952).
14) H.Y. Playford, A.C. Hannon, E.R. Barney, and R.I. Walton, Chem. - A Eur. J. **19**, 2803 (2013).
15) S.-D. Lee, K. Akaiwa, and S. Fujita, Phys. Status Solidi **10**, 1592 (2013).
16) S.-D. Lee, Y. Ito, K. Kaneko, and S. Fujita, Jpn. J. Appl. Phys. **54**, 030301 (2015).
17) W.W. Rudolph, C.C. Pye, and G. Irmer, J. Raman Spectrosc. **33**, 177 (2002).
18) D.F.C. Morris and B.D. Andrews, Electrochim. Acta **12**, 41 (1967).
19) K. Nomura, K. Goto, R. Togashi, H. Murakami, Y. Kumagai, A. Kuramata, S. Yamakoshi, and A. Koukitu, J. Cryst. Growth **405**, 19 (2014).
20) S. Yoshioka, H. Hayashi, A. Kuwabara, F. Oba, K. Matsunaga, and I. Tanaka, J. Phys. Condens. Matter **19**, 346211 (2007).
21) Y. Oshima, E.G. Víllora, and K. Shimamura, Appl. Phys. Express **8**, 055501 (2015).

Chapter 3

Control of Crystal Structure of Mist-CVD Grown α-Ga_2O_3 by α-$(Al_xGa_{1-x})_2O_3$ Layers

3.1 Introduction

Ga_2O_3 takes five different polymorphs (α, β, γ, δ, ε),[1,2] and the differences in free energy between each phases are smaller than 0.2 eV as calculated within the quasi-harmonic approximation (QHA).[3] Therefore, each phase can be grown by overcoming the small energy difference, leading to the difficulty of controlling the growth of Ga_2O_3 with a particular phase. For example, c-plane sapphire substrates, which is widely used to grow Ga_2O_3, offer the growth of β- and ε-Ga_2O_3 by molecular beam epitaxy (MBE) [4–6] and metal-organic chemical vapor deposition (MOCVD),[7,8] as well as the growth of α-Ga_2O_3 by mist-chemical vapor deposition (mist-CVD) [9] and halide vapor epitaxy (HVPE).[10] As described in Chapter 2, α-Ga_2O_3 is grown on c-plane sapphire substrates by the mist-CVD method at growth temperatures between 500 and 800 ºC, but the mist-CVD grown Ga_2O_3 on α-$(Al_xGa_{1-x})_2O_3$ has not been well understood. The controlled growth of α-Ga_2O_3 on α-$(Al_xGa_{1-x})_2O_3$ is essential for the α-Ga_2O_3 based heterostructure devices. In addition, α-$(Al_xGa_{1-x})_2O_3$ layers can be utilized as buffer layers reducing the high density dislocations caused by the large lattice mismatches between α-Ga_2O_3 and sapphire (4.6% for a-axis).[11] This chapter investigates the growth characteristics of the mist-CVD grown Ga_2O_3 on α-$(Al_xGa_{1-x})_2O_3$ layers to control the crystal structure of α-Ga_2O_3.

3.2 Experimental Procedures

All growth procedures were conducted using the hot-wall type mist CVD system. The growth conditions of α-$(Al_xGa_{1-x})_2O_3$ and α-Ga_2O_3 layers are summarized in Table 3.1. The Ga_2O_3 layers were grown using the carbon-free source of gallium tri-chloride ($GaCl_3$) as described in Chapter 2, while gallium(III) acetylacetone [$Ga(acac)_3$] and aluminum(III) acetylacetone [$Al(acac)_3$] were used as Ga and Al precursors for the growth of α-$(Al_xGa_{1-x})_2O_3$ layers since the growth of α-$(Al_xGa_{1-x})_2O_3$ using chloride sources is currently being researched. The α-$(Al_xGa_{1-x})_2O_3$ alloys were prepared by dissolving the source materials of $Ga(acac)_3$ and $Al(acac)_3$ together in deionized (DI) water and the alloy

composition was controlled from 0.17 to 0.86 by changing the molar ratios of Ga to Al in the source solution. [12] The growth temperature (T_g) of α-$(Al_xGa_{1-x})_2O_3$ was set at 450 (condition I) or 700 ºC (condition II). The growth of α-$(Al_xGa_{1-x})_2O_3$ at lower temperature can be utilized as a low temperature grown (LT) buffer layer for α-Ga_2O_3 like the LT GaN or AlN buffer layers, [13–15] while higher growth temperature produces the better crystal quality of α-$(Al_xGa_{1-x})_2O_3$ layer. Nitrogen (N_2) was used as both carrier and dilution gases for T_g= 450 ºC, while oxygen (O_2) was adopted for T_g= 700 ºC in order to prevent the carbonization of the surface of the samples. The carbonization arises from carbons (C) in the $Ga(acac)_3$ and $Al(acac)_3$ precursors, occurring at higher growth temperatures. The growth temperature of Ga_2O_3 was varied between 500 and 800 ºC. Since the growth rates of Ga_2O_3 and α-$(Al_xGa_{1-x})_2O_3$ are dependent on the growth temperature and the Al composition, the film thicknesses of those are stated in the following sections. The α-$(Al_xGa_{1-x})_2O_3$ layers were grown on c-plane sapphire substrates, and then the samples were annealed in an atmospheric furnace at 800 or 900 ºC for 30 min to improve surface morphology of the samples. The Ga_2O_3 layers were regrown on the α-$(Al_xGa_{1-x})_2O_3$ layers with/without the annealing process.

Table 3.1. Growth conditions of α-Ga_2O_3 and α-$(Al_xGa_{1-x})_2O_3$ layers.

	α-Ga_2O_3	**α-$(Al_xGa_{1-x})_2O_3$**	
		Condition I (LT)	Condition II (HT)
Al precursor	-	$Al(acac)_3$	$Al(acac)_3$
Al molar concentration		0.09 mol/L	0.04-0.12 mol/L
Ga precursor	$GaCl_3$	$Ga(acac)_3$	$Ga(acac)_3$
Ga molar concentration	0.05-0.1 mol/L	0.03 mol/L	0.02-0.04 mol/L
Carrier gas, flow rate	N_2, 3.0 L/min	N_2, 3.0 L/min	O_2, 5.0 L/min
Dilution gas, flow rate	N_2, 0.5 L/min	N_2, 0.5 L/min	O_2, 0.5 L/min
Growth time	30 min	1 h	30 min
Growth temperature T_g	500-800 ºC	450 ºC	700 ºC

3.3 Dependence on Growth Temperature of Ga_2O_3 Grown on α-$(Al_xGa_{1-x})_2O_3$

3.3.1 Low Temperature Growth of α-$(Al_{0.4}Ga_{0.6})_2O_3$

A low temperature grown α-$(Al_xGa_{1-x})_2O_3$ layer can be applied to buffer layers reducing the high dislocation density in α-Ga_2O_3 films grown on sapphire substrates. The LT buffer layer generally requires an annealing process. α-$(Al_xGa_{1-x})_2O_3$ with an intermediate Al composition has been reported to be more thermally stable than α-Ga_2O_3 or α-$(Al_xGa_{1-x})_2O_3$

with a lower Al content, maintaining the corundum structure at temperatures up to 900 ºC.[16] Therefore, a LT α-$(Al_{0.4}Ga_{0.6})_2O_3$ layer was investigated at first. The LT α-$(Al_{0.4}Ga_{0.6})_2O_3$ layers were grown at 450 ºC as shown in the condition I of Table 3.1. A symmetric X-ray diffraction (XRD) 2θ/ω scan profile confirms that the α-$(Al_{0.4}Ga_{0.6})_2O_3$ layer maintains the corundum structure after annealing at 900 ºC as previously reported [Fig. 3.1]. Figures 3.2(a) and 3.2(b) show surface atomic force microscopy (AFM) images of the α-$(Al_{0.4}Ga_{0.6})_2O_3$ film grown at 450 ºC before and after annealing at 900 ºC, respectively. The α-$(Al_{0.4}Ga_{0.6})_2O_3$ layer grown at 450 ºC has small grains with diameters of 20-50 nm and a root-mean-square (RMS) roughness of 1.67 nm. On the other hand, after annealing at 900 ºC, the surface morphology is markedly improved, and the RMS roughness of α-$(Al_{0.4}Ga_{0.6})_2O_3$ is reduced to 0.56 nm. In addition, a step-terrace structure is observed for the sample after annealing at 900 ºC. The step height of the α-$(Al_{0.4}Ga_{0.6})_2O_3$ layer is 0.45 nm, corresponding with the two molecular layers of α-$(Al_{0.4}Ga_{0.6})_2O_3$. The result suggests that a flattening process occurred during the annealing process although a significant improvement of the crystal quality of the film is not observed from the result of the XRD measurement.

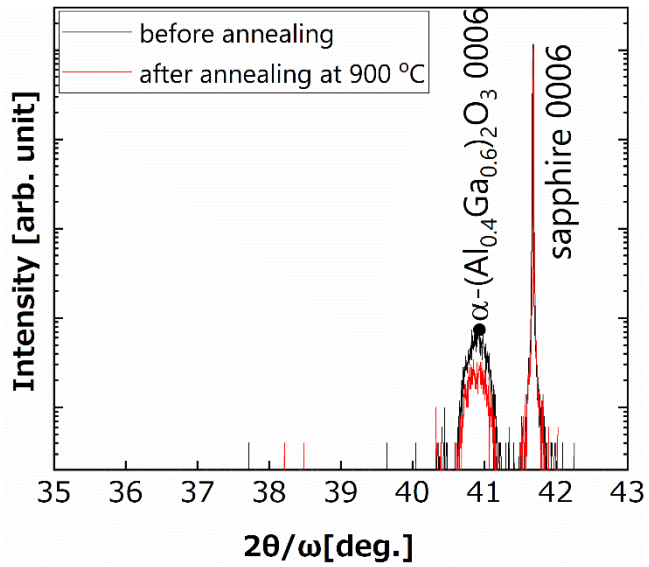

Figure 3.1 Symmetric XRD 2θ/ω scan profiles of the α-$(Al_{0.4}Ga_{0.6})_2O_3$ grown at 450 ºC before (black) and after (red) annealing at 900 ºC.

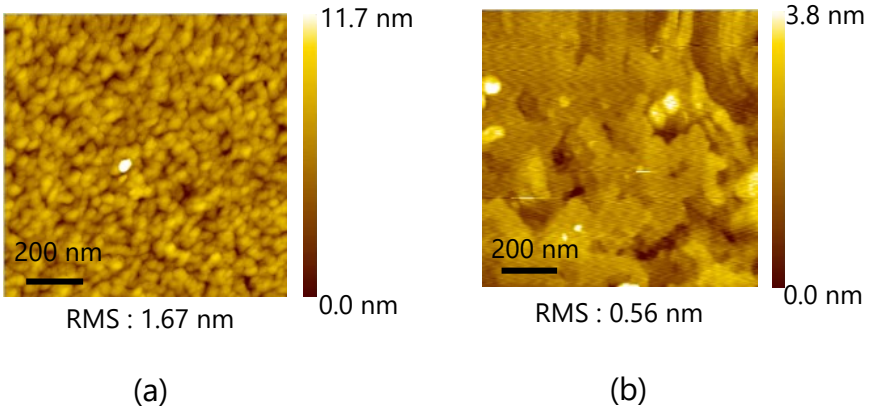

Figure 3.2 Surface AFM images of the LT α-$(Al_{0.4}Ga_{0.6})_2O_3$ layers grown at 450 ºC (a) before and (b) after annealing at 900 ºC.

3.3.2 Growth of Ga_2O_3 on LT α-$(Al_{0.4}Ga_{0.6})_2O_3$ Layer

Figure 3.3 shows the XRD 2θ/ω scan profiles for Ga_2O_3 with the α-$(Al_{0.4}Ga_{0.6})_2O_3$ LT layers annealed at 900 ºC. The profiles for T_g≤600 ºC are dominated by diffraction peaks from ε-Ga_2O_3 0002, 0004, 0006 and 0008 reflexes at 2θ= 19.17, 38.90, 59.95 and 83.55º. On the other hand, the samples grown at T_g≥600 ºC show α-Ga_2O_3 0006 reflex at 2θ= 40.12º.

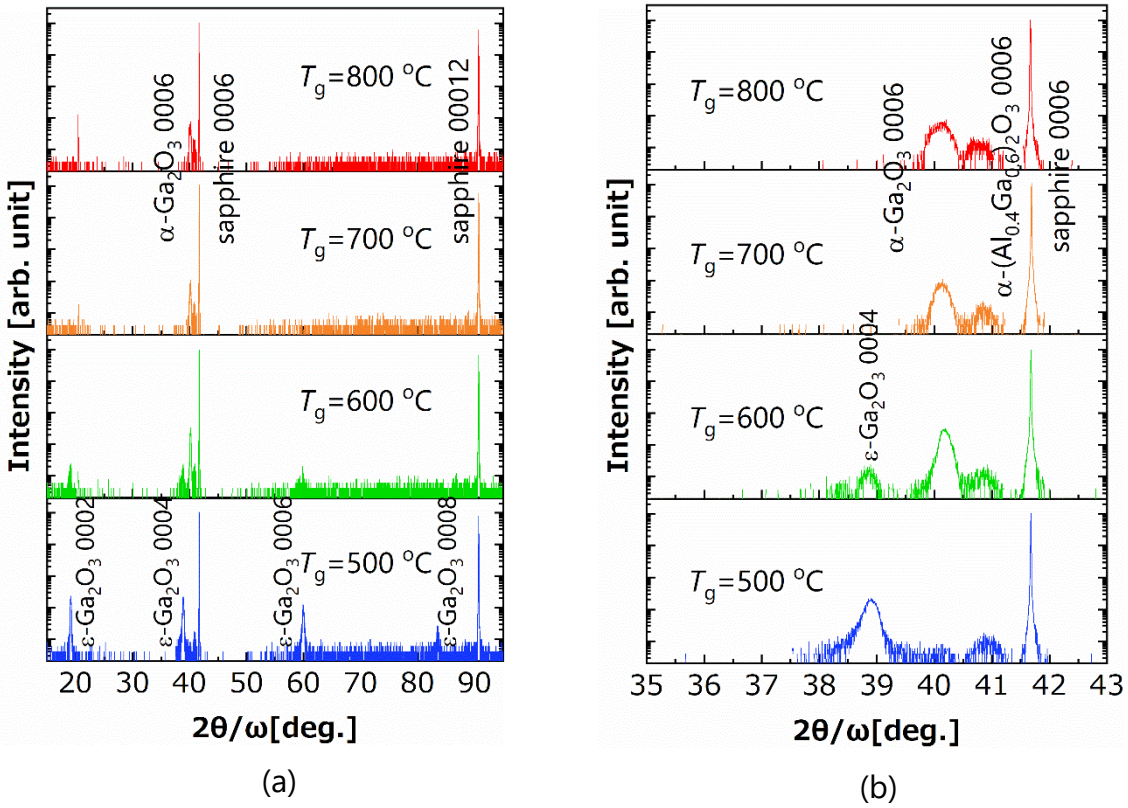

Figure 3.3 Symmetric XRD 2θ/ω scan profiles of Ga_2O_3 with the α-$(Al_{0.4}Ga_{0.6})_2O_3$ layers annealed at 900 ºC as a function of the growth temperature of Ga_2O_3.

It was predicted that α-Ga_2O_3 would be pseudmorphically grown on the α-$(Al_{0.4}Ga_{0.6})_2O_3$ layer when T_g was lower than 600 ºC as α-Ga_2O_3 is generally grown on sapphire at around 500 ºC. However, ε-Ga_2O_3 is grown at $T_g \leq 600$ ºC, while α-Ga_2O_3 is obtained at $T_g \geq 600$ ºC. This result can be assumed as follows. The epitaxial relationship between ε-Ga_2O_3 and sapphire has been reported to be ε-Ga_2O_3 $[10\bar{1}0]$|| sapphire $[11\bar{2}0]$, which yields a lattice mismatch of ca. 4.1% obtained by the distance between cations [Fig.3.4].[8)]*[1] Based on this ideas, the lattice mismatch between the α-$(Al_{0.4}Ga_{0.6})_2O_3$ layer and ε-Ga_2O_3 is estimated to be 1.2%, while α-Ga_2O_3 has a lattice mismatch of 2.2%. Therefore, when the growth temperature is lower than 600 ºC, it seems that Ga and O atoms align so that the lattice mismatch is minimized, and thus form the ε-phase. On the other hand, α-Ga_2O_3 is grown by inheriting the arrangement of the α-$(Al_{0.4}Ga_{0.6})_2O_3$ layer at high temperature. As a result, ε-Ga_2O_3 and α-Ga_2O_3 are grown below and above 600 ºC, respectively.

Transmission electron microscopy (TEM) observations of Ga_2O_3 grown at 500 ºC (ε-Ga_2O_3) and 700 ºC (α-Ga_2O_3) were carried out to determine the crystal structure of Ga_2O_3 and epitaxial relationships between Ga_2O_3 and α-$(Al_{0.4}Ga_{0.6})_2O_3$ layers in detail.

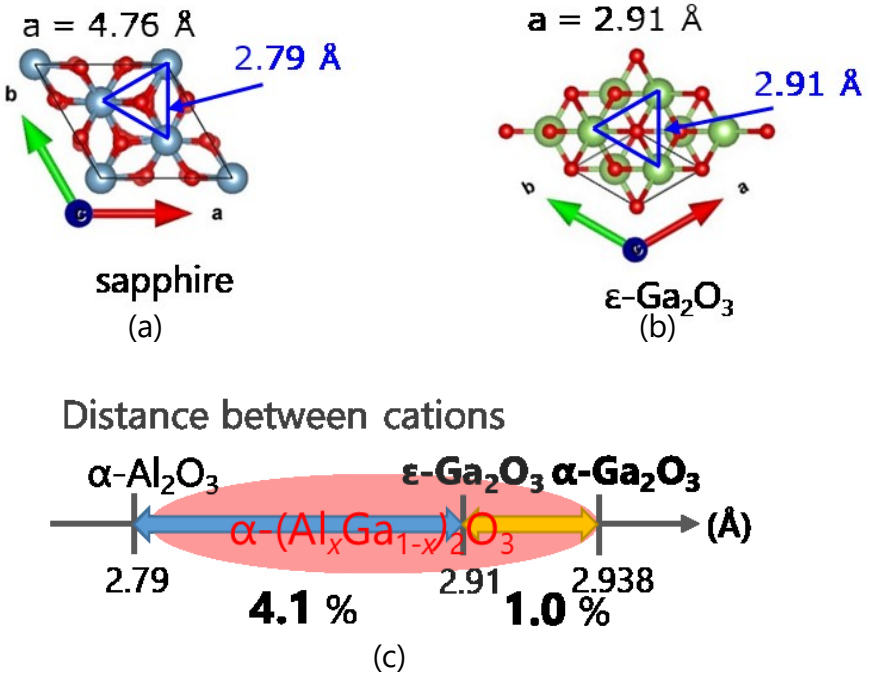

Figure 3.4 Schematic of (a) sapphire (α-Al_2O_3) and (b) ε-Ga_2O_3 atomic arrangements viewed along the c-axis. Red, green and blue balls represent oxygen, gallium and aluminum atoms, respectively. (c) shows the lattice mismatches between sapphire, α- and ε-Ga_2O_3 based on the distance between cations.

[1] Although ε-Ga_2O_3 has been revealed to have the orthorhombic structure with $Pna2_1$ now, [17,18)] the ε-phase was considered to have the hexagonal $P6_3mc$ space group symmetry at that time.

Figure 3.5(a) shows the electron diffraction pattern for the α-Ga_2O_3/α-$(Al_{0.4}Ga_{0.6})_2O_3$ layer/sapphire substrate observed along the $\langle 11\bar{2}0 \rangle$ zone axis. The diffraction spots for the α-Ga_2O_3 main layer and the α-$(Al_{0.4}Ga_{0.6})_2O_3$ layer are situated inside of those of sapphire, which indicates that both the α-Ga_2O_3 and α-$(Al_{0.4}Ga_{0.6})_2O_3$ layers have the corundum structure and are single crystals. The α-Ga_2O_3 main layer has the same crystal orientation as the α-$(Al_{0.4}Ga_{0.6})_2O_3$ layer and the epitaxial relationships between them are α-Ga_2O_3 (0006)||α-$(Al_{0.4}Ga_{0.6})_2O_3$ (0006) and α-Ga_2O_3 $[11\bar{2}0]$||α-$(Al_{0.4}Ga_{0.6})_2O_3$ $[11\bar{2}0]$. The diffraction spots for α-Ga_2O_3, α-$(Al_{0.4}Ga_{0.6})_2O_3$, and sapphire are clearly separated far from the origin. However, near the origin, these spots appear to be overlapped because the diffraction intensity is strong, and the distance between the spots for the epitaxial layers and the substrate is close. Figure 3.5(b) shows a cross-sectional TEM image taken at the α-Ga_2O_3/α-$(Al_{0.4}Ga_{0.6})_2O_3$ layer/sapphire substrate. The film thickness of α-Ga_2O_3 is ca. 30 nm. As shown in Figure 3.5(b), dislocations are present at the α-$(Al_{0.4}Ga_{0.6})_2O_3$/sapphire and α-Ga_2O_3/α-$(Al_{0.4}Ga_{0.6})_2O_3$ interfaces and a significant reduction of the dislocation density in the α-Ga_2O_3 layer is not occured by the introduction of the LT α-$(Al_{0.4}Ga_{0.6})_2O_3$ layer.

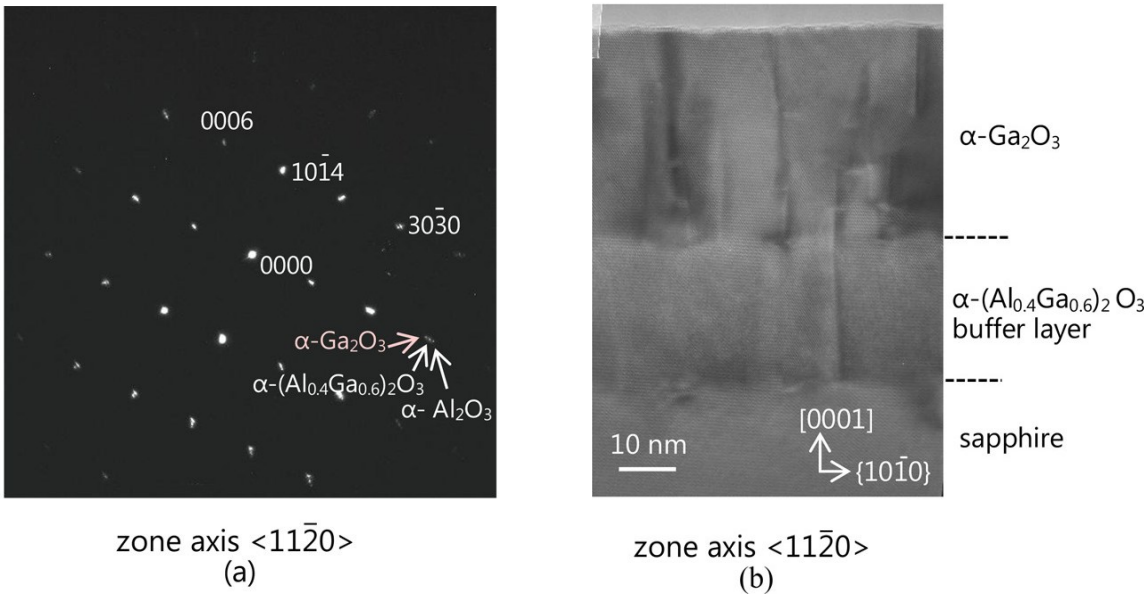

Figure 3.5 (a) Diffraction spots for α-Ga_2O_3/α-$(Al_{0.4}Ga_{0.6})_2O_3$ layer/sapphire interface viewed along the $\langle 11\bar{2}0 \rangle$ direction. (b) Cross-sectional TEM image of α-Ga_2O_3/α-$(Al_{0.4}Ga_{0.6})_2O_3$ layer/sapphire interface observed along the $\langle 11\bar{2}0 \rangle$ direction .

Figure 3.6(a) shows an electron diffraction pattern for ε-Ga_2O_3/α-$(Al_{0.4}Ga_{0.6})_2O_3$ layer/sapphire substrate viewed along the $\langle 10\bar{1}0 \rangle$ zone axis of sapphire. As shown in Fig. 3.6(a), the epitaxial relationships between the ε-Ga_2O_3 main layer and the α-$(Al_{0.4}Ga_{0.6})_2O_3$ buffer layer are ε-Ga_2O_3 (002)||α-$(Al_{0.4}Ga_{0.6})_2O_3$ (0003) and ε-Ga_2O_3 [200], [310] ||α-$(Al_{0.4}Ga_{0.6})_2O_3$ [$11\bar{2}0$]. Here, ε-Ga_2O_3 is taken as orthorhombic. The relationship between the orthorhombic and hexagonal structures of ε-Ga_2O_3 has been reported by Nishinaka *et al.* [17] The diffraction spots for ε-Ga_2O_3, α-$(Al_{0.4}Ga_{0.6})_2O_3$, and sapphire near the origin appear to be overlapped, as shown in Fig. 3.6(a). The diffraction spots also exhibited streaks along the $\langle 002 \rangle$ direction. It is assumed that these streaks are the result of defects along the $\langle 002 \rangle$ direction in the ε-Ga_2O_3 layer.

Figures 3.6(b) and 3.6(c) show cross-sectional TEM images of ε-Ga_2O_3/ α-$(Al_{0.4}Ga_{0.6})_2O_3$ layer/sapphire substrate and an enlarged TEM image of ε-Ga_2O_3, respectively. The ε-Ga_2O_3 film thickness is ca. 100 nm. The crystal structure of ε-Ga_2O_3 is confirmed from Fig. 3.6(c). However, horizontal lines are observed in the TEM image of the ε-Ga_2O_3 layer with color contrasts. For the growth of ε-Ga_2O_3 on hexagonal structure, three rotational domains have been reported to be occurred due to the orthorhombic structure. [17,18] The horizontal defects seem to arise from stacking faults because of the three

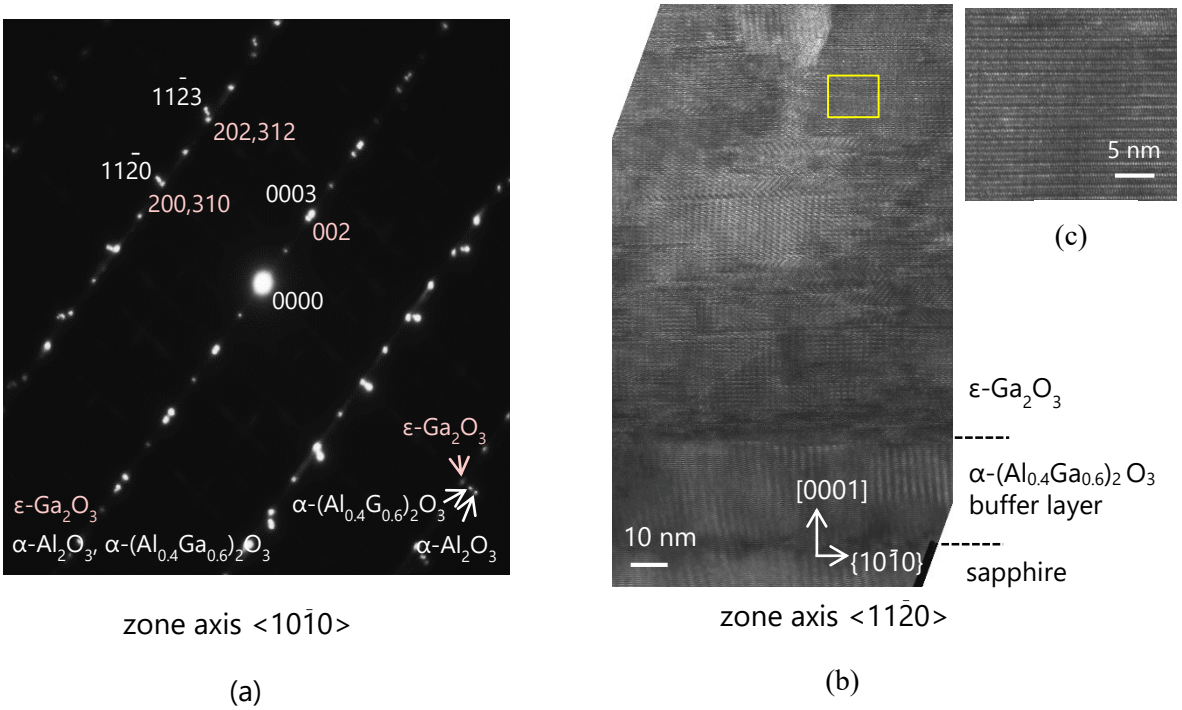

Figure 3.6 (a) Diffraction spots for ε-Ga_2O_3/α-$(Al_{0.4}Ga_{0.6})_2O_3$ layer/sapphire interface viewed along the $\langle 10\bar{1}0 \rangle$ direction. (b) Cross-sectional TEM image of ε-Ga_2O_3/α-$(Al_{0.4}Ga_{0.6})_2O_3$ layer/sapphire interface observed along the $\langle 11\bar{2}0 \rangle$ direction. (c) Enlarged image of the framework shown in (b).

rotational domains. The white streaks along the ⟨002⟩ direction in the electron diffraction pattern are considered to originate from these stacking faults.

3.4 Dependence on Annealing Process of α-$(Al_xGa_{1-x})_2O_3$ Layer

Based on the distance between cations, ε-Ga_2O_3 matches to α-$(Al_xGa_{1-x})_2O_3$ whose Al concentration is around 0.2, as shown in Fig.3.4. If crystal structures of Ga_2O_3 depend on the lattice mismatches to α-$(Al_xGa_{1-x})_2O_3$ layers, ε-Ga_2O_3 is predicted to be grown on

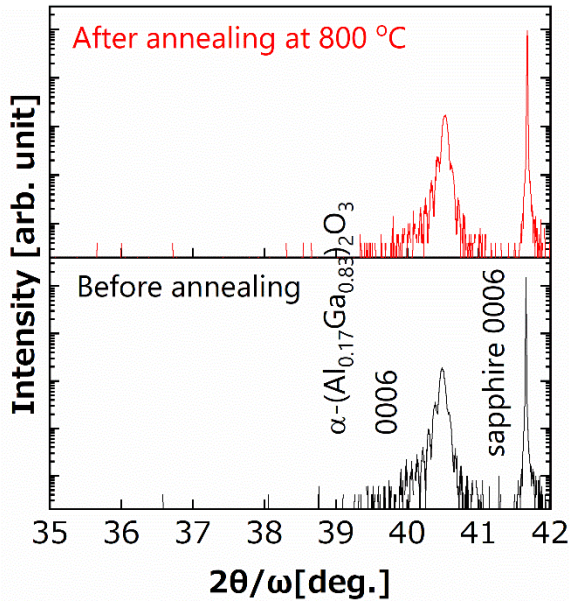

(a)

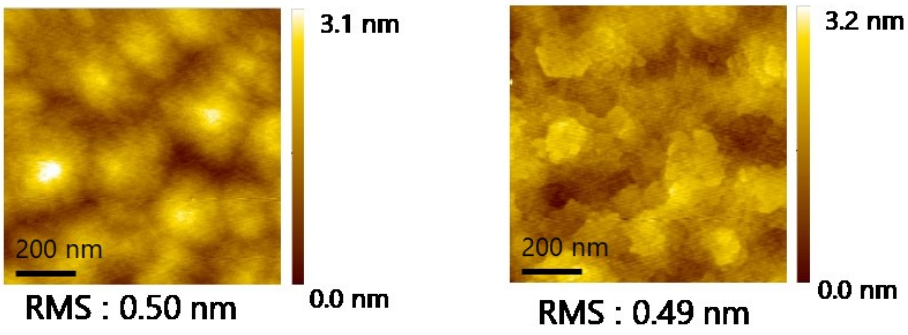

(b) Before annealing (c) After annealing

Figure 3.7 (a) Symmetric XRD 2θ/ω scan profiles of the α-$(Al_{0.17}Ga_{0.83})_2O_3$ grown at 700 ºC before (black) and after (red) annealing at 800 ºC. Surface AFM images of the α-$(Al_{0.17}Ga_{0.83})_2O_3$ layers (b) before and (c) after annealing at 800 ºC.

α-$(Al_xGa_{1-x})_2O_3$ layers regardless of the annealing process. This section explores an effect of the annealing process on the crystal structure of Ga_2O_3.

α-$(Al_{0.17}Ga_{0.83})_2O_3$, which is almost lattice-matched to ε-Ga_2O_3, is grown on a c-plane sapphire substrate at 700 ºC, as shown in the growth condition II of Table 2.1. The phase transition temperature of Ga-rich α-$(Al_xGa_{1-x})_2O_3$ is around 800 ºC, lower than that of the α-$(Al_{0.4}Ga_{0.6})_2O_3$. Therefore, the α-$(Al_{0.18}Ga_{0.82})_2O_3$ films was annealed at 800 ºC to prevent the phase transition to the β-phase. [16)]

A symmetric XRD 2θ/ω scan profile reveals that the α-$(Al_{0.17}Ga_{0.83})_2O_3$ layer maintains the corundum structure after annealing at 800 ºC [Fig. 3.7(a)]. As shown in Fig. 3.7(b), the high growth temperature of 700 ºC improves the surface roughness of the α-$(Al_{0.18}Ga_{0.82})_2O_3$ film as grown and the RMS roughness of the sample is as small as 0.50 nm. Although the annealing process does not change the RMS roughness of the sample (0.49 nm), the step-terrace structure, which is also observed in the AFM image of the annealed LT α-$(Al_{0.4}Ga_{0.6})_2O_3$ layer [Fig. 3.1(b)], is confirmed by the surface AFM image [Fig. 3.7(c)].

Ga_2O_3 films were regrown on the α-$(Al_{0.17}Ga_{0.83})_2O_3$ layer before and after annealing at T_g= 500 ºC, which is the temperature that ε-Ga_2O_3 was obtained on the annealed α-$(Al_{0.4}Ga_{0.6})_2O_3$ layer. Figure 3.8 shows symmetric XRD 2θ/ω scan profiles of the Ga_2O_3 on the α-$(Al_{0.17}Ga_{0.83})_2O_3$ layer before and after annealing. As expected, ε-Ga_2O_3 is grown on the α-$(Al_{0.17}Ga_{0.83})_2O_3$ layer after annealing as well as on the annealed LT

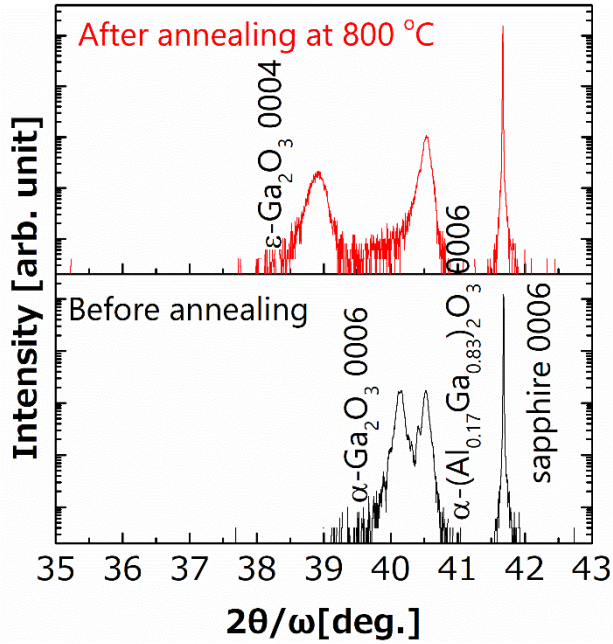

Figure 3.8 Symmetric XRD 2θ/ω scan profiles of Ga_2O_3 on the α-$(Al_{0.17}Ga_{0.93})_2O_3$ layers.

α-$(Al_{0.4}Ga_{0.6})_2O_3$ layer. On the other hand, although α-$(Al_{0.17}Ga_{0.83})_2O_3$ is lattice-matched to ε-Ga_2O_3, α-Ga_2O_3 is obtained on the α-$(Al_{0.17}Ga_{0.83})_2O_3$ layer without the annealing process, indicating the annealing process influences on the crystal phase of Ga_2O_3 on the α-$(Al_{0.17}Ga_{0.83})_2O_3$ layer by changing the surface morphology or the surface termination structure of the α-$(Al_{0.17}Ga_{0.83})_2O_3$ layer.

3.5 Dependence on Al Contents of Annealed α-$(Al_xGa_{1-x})_2O_3$ Layer

This section investigates the dependence of Ga_2O_3 polymorphs on Al compositions of annealed α-$(Al_xGa_{1-x})_2O_3$ layers. The Al composition was changed between 0.17 and 0.86. The α-$(Al_xGa_{1-x})_2O_3$ samples were grown at T_g= 700 ºC in the growth condition II of Table 2.1, and then were annealed at 800 ºC. Ga_2O_3 films were regrown on the annealed α-$(Al_xGa_{1-x})_2O_3$ layers at T_g= 500 ºC. Symmetric XRD 2θ/ω profiles exhibit that ε-Ga_2O_3 films are grown on the annealed α-$(Al_xGa_{1-x})_2O_3$ layers and the dependence of the polymorphs on the Al composition is not observed [Fig. 3.9]. From these results, the crystal structure of Ga_2O_3 is strongly correlated with the surface structure, not with lattice mismatches when the growth temperature is 500 ºC.

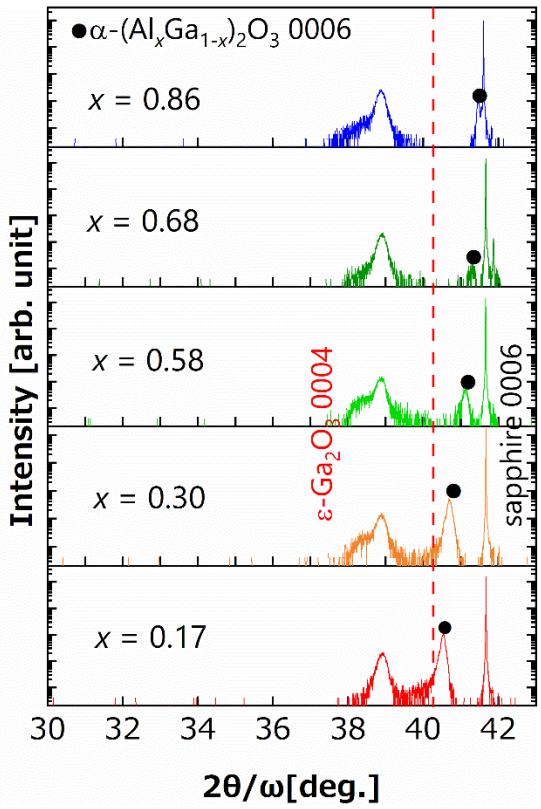

Figure 3.9 Symmetric XRD 2θ/ω scan profiles of Ga_2O_3 on the α-$(Al_xGa_{1-x})_2O_3$ layers annealed at 800 ºC as a function of the Al composition *x*.

3.6 Discussion

It was predicted that α-Ga_2O_3 is grown by inheriting the structure of α-$(Al_xGa_{1-x})_2O_3$ layers in any growth conditions. However, ε-Ga_2O_3 was grown on the annealed α-$(Al_xGa_{1-x})_2O_3$ layers at growth temperature of Ga_2O_3 lower than 600 ºC. On the other hand, α-Ga_2O_3 layers were obtained when the growth temperatures were higher than 600 ºC or α-$(Al_xGa_{1-x})_2O_3$ films were not exposed to the annealing process. The schematics of the formation model of α- and ε-Ga_2O_3 are shown in Fig.3.10. With the annealing process, the α-$(Al_xGa_{1-x})_2O_3$ layers had the surface morphology with the step-terrace structure. The step-terrace structure would cause the crystal structure of overgrown Ga_2O_3 to be determined by the diffusion length. When the growth temperature is lower than 600 ºC, the diffusion length is considered to be shorter than half the terrace width for α-$(Al_xGa_{1-x})_2O_3$. Therefore, Ga_2O_3 grows in the three-dimensional nucleus growth mode, and it seems that Ga and O atoms align so that the lattice mismatch is minimized, and thus form the ε-phase. When the diffusion length is so long that atoms can reach the step edges, the same crystal structure as the α-$(Al_xGa_{1-x})_2O_3$ layer seems to be stable for the epitaxial layer, leading to the growth of α-Ga_2O_3 along the step edges at higher growth temperatures. As a result, ε-Ga_2O_3 and α-Ga_2O_3 are grown on α-$(Al_xGa_{1-x})_2O_3$ annealed below and above 600 ºC, respectively. In fact, the result of Chapter 2 revealed that the α-Ga_2O_3 films on sapphire substrates have small grains with the diameter of 50-200 nm for T_g<600 ºC and smooth surface morphology for T_g≥600 ºC, supporting the longer diffusion length at higher growth temperatures. On the other hand, the step-terrace structure was not observed in the surface morphology of as grown α-$(Al_xGa_{1-x})_2O_3$ layers even when the RMS roughness is as small as the annealed layer. Therefore, atoms can be easily incorporated into edges and kinks on the surface with inheriting the the structure of α-$(Al_xGa_{1-x})_2O_3$ layers, leading to the formation of α-Ga_2O_3. However, α-Ga_2O_3 is grown on a sapphire substrate showing steps at T_g=500 ºC. This may be caused by the large lattice mismatch of 4.6 % or sapphire could have the different surface terminations from the α-$(Al_xGa_{1-x})_2O_3$ layers after annealing. In addition to the surface morphology, it is also possible that surface termination of α-$(Al_xGa_{1-x})_2O_3$ films were changed by the annealing process. The termination of the surfaces is required to be investigate in detail in future.

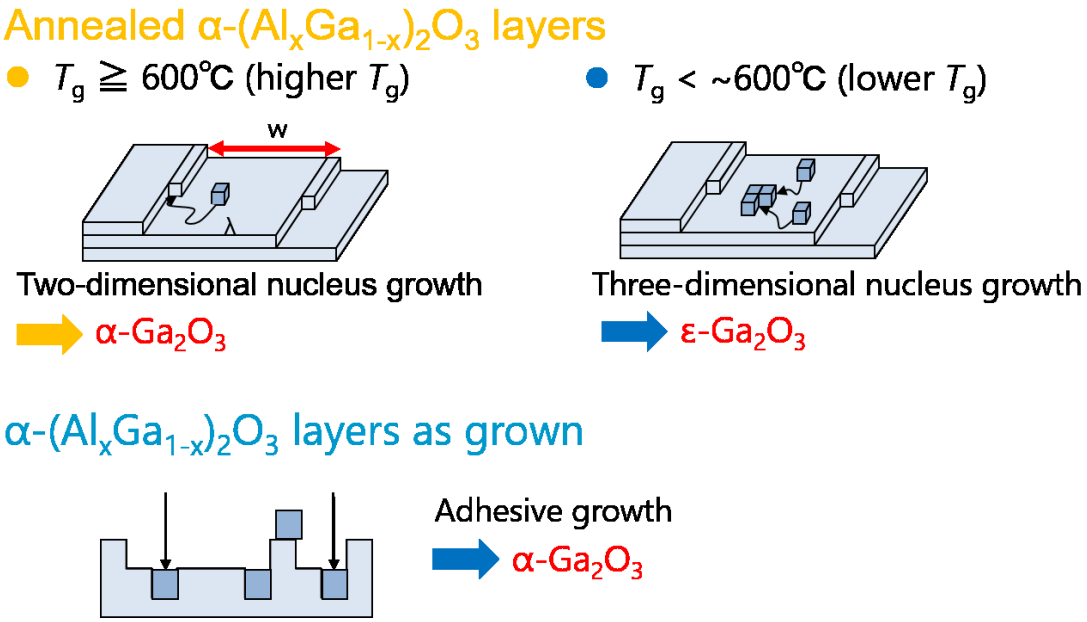

Figure 3.10 Schematics model for formation of α- and ε-Ga_2O_3 at higher and lower temperatures.

3.7 Summary

This chapter explored that crystal phases of Ga_2O_3 layers grown on α-$(Al_xGa_{1-x})_2O_3$ layers. The surface morphology of the α-$(Al_xGa_{1-x})_2O_3$ layers after annealing at 800-900 ºC showed a step-terrace structure, leading to the growth of ε-Ga_2O_3 at lower growth temperature than 600 ºC. On the other hand, longer diffusion lengths yield by higher growth temperature, or kinks on the surface of as grown α-$(Al_xGa_{1-x})_2O_3$ layers allow atoms to reach the edges on the surface, resulting in the formation of α-Ga_2O_3, which has the same structure as the α-$(Al_xGa_{1-x})_2O_3$ layer. From these results, α-Ga_2O_3 can be conrolled on α-$(Al_xGa_{1-x})_2O_3$ by using higher growth temperature.

References

1) R. Roy, V.G. Hill, and E.F. Osborn, J. Am. Chem. Soc. **74**, 719 (1952).
2) H.Y. Playford, A.C. Hannon, E.R. Barney, and R.I. Walton, Chem. - A Eur. J. **19**, 2803 (2013).
3) S. Yoshioka, H. Hayashi, A. Kuwabara, F. Oba, K. Matsunaga, and I. Tanaka, J. Phys. Condens. Matter **19**, 346211 (2007).
4) T. Oshima, T. Okuno, and S. Fujita, Jpn. J. Appl. Phys. **46**, 7217 (2007).
5) M. Kracht, A. Karg, J. Schörmann, M. Weinhold, D. Zink, F. Michel, M. Rohnke, M. Schowalter, B. Gerken, A. Rosenauer, P.J. Klar, J. Janek, and M. Eickhoff, Phys. Rev. Appl. **8**, 054002 (2017).
6) X. Bi, Z. Wu, Y. Huang, and W. Tang, AIP Adv. **8**, 025008 (2018).
7) Y. Lv, J. Ma, W. Mi, C. Luan, Z. Zhu, and H. Xiao, Vacuum **86**, 1850 (2012).
8) F. Mezzadri, G. Calestani, F. Boschi, D. Delmonte, M. Bosi, and R. Fornari, Inorg. Chem. **55**, 12079 (2016).
9) D. Shinohara and S. Fujita, Jpn. J. Appl. Phys. **47**, 7311 (2008).
10) Y. Oshima, E.G. Víllora, and K. Shimamura, Appl. Phys. Express **8**, 055501 (2015).
11) K. Kaneko, H. Kawanowa, H. Ito, and S. Fujita, Jpn. J. Appl. Phys. **51**, 020201 (2012).
12) H. Ito, K. Kaneko, and S. Fujita, Jpn. J. Appl. Phys. **51**, 100207 (2012).
13) H. Amano, N. Sawaki, I. Akasaki, and Y. Toyoda, Appl. Phys. Lett. **48**, 353 (1986).
14) K. Hiramatsu, S. Itoh, H. Amano, I. Akasaki, N. Kuwano, T. Shiraishi, and K. Oki, J. Cryst. Growth **115**, 628 (1991).
15) I. Akasaki, H. Amano, Y. Koide, K. Hiramatsu, and N. Sawaki, J. Cryst. Growth **98**, 209 (1989).
16) S.-D. Lee, Y. Ito, K. Kaneko, and S. Fujita, Jpn. J. Appl. Phys. **54**, 030301 (2015).
17) H. Nishinaka, H. Komai, D. Tahara, Y. Arata, and M. Yoshimoto, Jpn. J. Appl. Phys. **57**, 115601 (2018).
18) I. Cora, F. Mezzadri, F. Boschi, M. Bosi, M. Čaplovičová, G. Calestani, I. Dódony, B. Pécz, and R. Fornari, CrystEngComm **19**, 1509 (2017).

Chapter 4

Reduction of Dislocation Density in α-Ga_2O_3 Films on Sapphire Substrates

4.1 Introduction

Since α-Ga_2O_3 does not have its high quality substrates yet due to its thermodynamically metastable character, the heteroepitaxial growth of α-Ga_2O_3 is essential for α-Ga_2O_3 based power devices. In general, sapphire (α-Al_2O_3) is used as the substrate for the growth of α-Ga_2O_3 since both materials have the same corundum structure. However, the α-Ga_2O_3 films grown on the sapphire substrate have high density dislocations, which arises from the lattice mismatches to the substrates (3.54 and 4.81% along c- and a-axes, respectively). Especially the edge dislocation density has been reported as 7×10^{10} cm^{-2} by the method of Ham. [1] In this chapter, the author describes the reduction of dislocation density in the α-Ga_2O_3 films on sapphire substrates by two ways: an introduction of α-$(Al_xGa_{1-x})_2O_3$ multilayers as buffer layers and the epitaxial lateral overgrowth technique.

4.2 Method of Reducing Dislocation Densities in α-Ga_2O_3 Film on Sapphire Substrate

4.2.1 Quasi-Graded α-$(Al_xGa_{1-x})_2O_3$ Buffer Layer

Using buffer layers allows a reduction of dislocation densities by confining strains and misfit dislocations originated from lattice mismatches between substrates and films within the buffer layers. The study on the group III-V and II-VI semiconductors has developed several types of the buffer layers such as low/high temperature buffer layers, [2,3] strained super lattice buffer layers, [4] and compositionally graded buffer layers. [5–9] For the heteroepitaxial growth of α-Ga_2O_3 on sapphire, the compositionally graded-buffer and strained super lattice buffer are available by utilizing an α-$(Al_xGa_{1-x})_2O_3$ alloy, which has an intermediate lattice length. [10] Here, the author combines the both buffer layers and proposes “compositionally quasi-graded buffer layer”. Figure 4.1 shows the schematic of the compositionally graded and the quasi-graded buffer layers. The graded buffer layer gradually changes an Al composition of α-$(Al_xGa_{1-x})_2O_3$ from Al-rich (substrate) to Ga-rich (film) so that the lattice length is gradually changed from a substrate to a film and the

introduction of dislocations is expected to be suppressed. The quasi-graded buffer layer controls the average composition and lattice length of the buffer layer by the thickness ratios of Al-rich/Ga-rich layers instead of the real composition as the digital alloy does. The buffer layer is expected to enhance the controllability of changing the Al composition and prevent the dislocation from propagating upward α-Ga_2O_3.

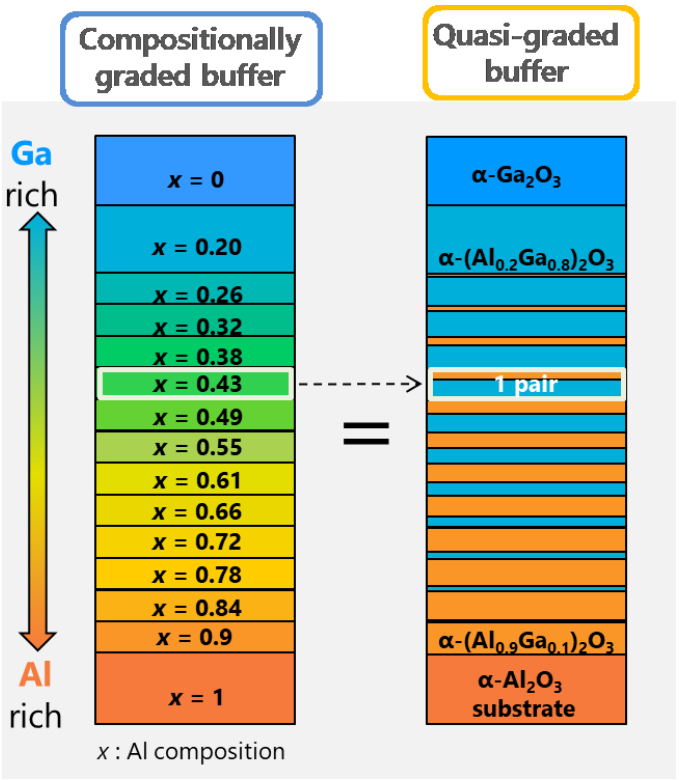

Figure 4.1. Schematics of the compositionally graded and quasi-graded buffer

4.2.2 Epitaxial Lateral Overgrowth of α-Ga_2O_3

The epitaxial lateral overgrowth technology has been used as one of the most promising ways to reduce the density of dislocations in GaN. [11–15] The growth models of epitaxial lateral overgrowth of GaN are shown Fig. 4.2.[15] In the process, a part of highly dislocated layer is masked with a dielectric mask such as SiO_2 and SiN, and after that the growth is restarted. The mask filters the dislocations under it, being covered by the laterally grown GaN, which is defect-free. Hiramatsu *et al.* has proposed two typical models as shown in Fig. 4.2; in one model (A), the dislocation concentrates only on the window area and, in the other model (B), only in the coalescence region in the center of the mask,[15] that is so-called facet-controlled epitaxial lateral over growth (FACELO). The inclined facet in the Model B has allowed a dramatic decrease of the dislocation density in GaN to the order of

10^6 cm^{-2}. The Model B includes two-step processes with different growth conditions so that the lateral growth rate is increased and the mask is easily buried. In Model A, a ratio of lateral and vertical growth rates (*L*/*V* ratio) is important to reduce the dislocation density effectively since the larger *L*/*V* ratio is preferable for a small fill factor (ratio of the stripe window to the patterned period), resulting in a small area of the highly dislocated region above the window area. Therefore, facet structures and *L*/*V* ratio are crucial parameters in the technology, which are controlled by growth conditions such as reactor pressure and growth temperature for FACEL of GaN via low-pressure MOVCVD. [14)]

The dislocation density in α-Ga_2O_3 is also expected to be reduced by using the epitaxial lateral overgrowth process. This chapter explores the epitaxial lateral overgrown (ELO) α-Ga_2O_3 via mist-CVD, which has achieved promising results of α-Ga_2O_3. [10,16–18)] The mist-CVD growth is considered occur in a non-equilibrium state due to using mist particles and an atmospheric pressure. In addition, only an oxygen rich condition is available because of atomizing a liquid solution including source atoms. These indicate that, unlike MOCVD, it is difficult to control facet structures and the *L*/*V* ratio dramatically by only growth conditions such as a VI/III ratio and growth temperature in the mist-CVD process. Therefore, the ELO α-Ga_2O_3 on various substrate orientations with different stripe directions are investigated in order to control the facet structures and the *L*/*V* ratio.

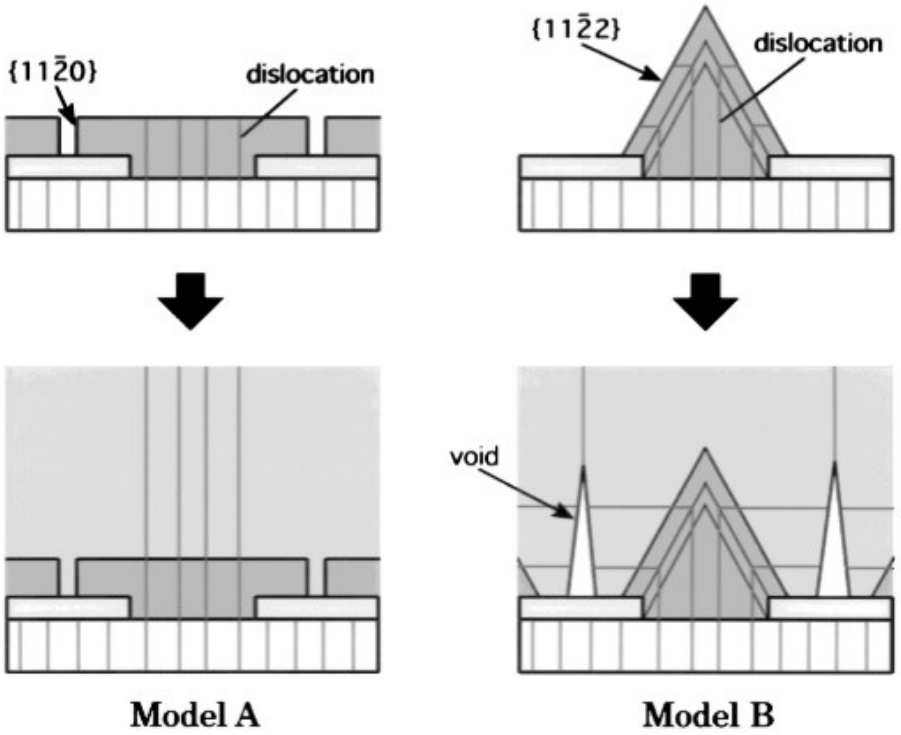

Figure 4.2. Schematics of the epitaxial lateral overgrowth (ELO) and FACELO (Facet Controlled ELO) of GaN. Two different types of models, A and B, are shown. [15)]

4.3 α-Ga_2O_3 Layers on Sapphire Substrates with α-$(Al_xGa_{1-x})_2O_3$ Quasi-Graded Buffer Layer

4.3.1 Experimental Procedures

The schematic structure of buffer layers on a c-plane sapphire substrate is illustrated in Fig. 4.3. Although α-Al_2O_3/Ga_2O_3 multiple layers are ideal as the buffer layer, the growth temperature of α-Al_2O_3 is higher than that of α-Ga_2O_3, which could lead to an inclusion/growth of β-Ga_2O_3. The growth temperature difference is not preferable for the growth of multiple layers as well since it requires temperature raising/lowering frequently. On the other hand, α-$(Al_xGa_{1-x})_2O_3$ can be grown at the same growth temperature with a reasonable crystal quality and was adopted as materials of the buffer layers. The buffer layers consist with alternatives of α-$(Al_{0.9}Ga_{0.1})_2O_3$ and α-$(Al_{0.2}Ga_{0.8})_2O_3$ layers, where the thickness of α-$(Al_{0.9}Ga_{0.1})_2O_3$ was gradually decreased while that of α-$(Al_{0.2}Ga_{0.8})_2O_3$ was gradually increased from the position close to the sapphire substrate to the α-Ga_2O_3 main layer.

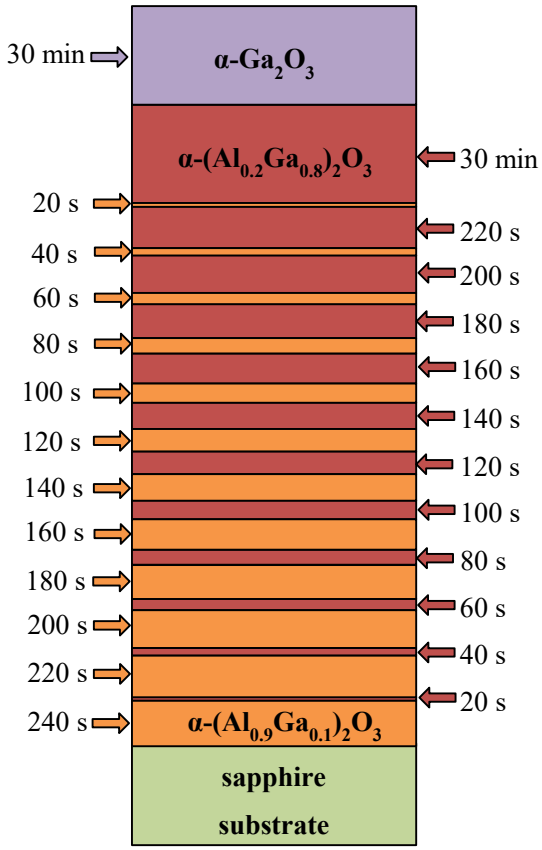

Figure 4.3. Sample structure and growth sequence of the constituent layers.

Prior to the growth of the sample, the sapphire substrate was annealed in air at 1050ºC for 12 hours to obtain atomically flat surface, and then washed in acetone, methanol, and deionized (DI) water in an ultrasonic cleaner. The α-Ga_2O_3 main layer and the α-$(Al_xGa_{1-x})_2O_3$ buffer layers were grown by the mist CVD method. Gallium(Ⅲ) acetylacetonate [$Ga(acac)_3$] and aluminum(Ⅲ) acetylacetonate [$Al(acac)_3$] were used as the precursors for Ga and Al, respectively, which were solved in DI water. The growth conditions of α-Ga_2O_3 and α-$(Al_xGa_{1-x})_2O_3$ (x = 0.2 and 0.9) layers are summarized in Table 4.1. Here, the molar concentrations of Ga and Al (mol/L) are shown as [Ga] and [Al], respectively, which were determined so that the growth rate of α-$(Al_xGa_{1-x})_2O_3$ reached ca. 5 nm/min. Since the incorporation rate of Al from the source precursor into the film was lower than that of Ga, the liquidus composition ratio of [Al]/([Ga]+[Al]) was higher than the solidus composition of Al (x). The growth of α-$(Al_xGa_{1-x})_2O_3$ multiple layers was carried out at 700 ºC, then, following the growth of α-Ga_2O_3 at 470 ºC. Nitrogen (N_2) was used as both carrier and dilution gases for the growth of α-Ga_2O_3. On the other hand, oxygen (O_2) was used for the growth of α-$(Al_xGa_{1-x})_2O_3$, for preventing carbonization of the surface of the α-$(Al_xGa_{1-x})_2O_3$, as explained in Chapter 3. The growth times of α-$(Al_xGa_{1-x})_2O_3$ buffer layers and α-Ga_2O_3 main layer are shown in Fig.4.3. The author designed the buffer layer structure taking double layers of α-$(Al_{0.9}Ga_{0.1})_2O_3$/α-$(Al_{0.2}Ga_{0.8})_2O_3$ as a basic pair, which was grown in 4 min (the thickness of 20 nm). 12 pairs of α-$(Al_{0.9}Ga_{0.1})_2O_3$/α-$(Al_{0.2}Ga_{0.8})_2O_3$ layers were formed on sapphire increasing the growth time of α-$(Al_{0.2}Ga_{0.8})_2O_3$ layers by 20 seconds from 0 to 220 seconds while decreasing the growth time of α-$(Al_{0.9}Ga_{0.1})_2O_3$ layers by 20 seconds from 240 to 20 seconds. Then, an α-$(Al_{0.2}Ga_{0.8})_2O_3$ layer was grown on the 12 pairs of α-$(Al_{0.9}Ga_{0.1})_2O_3$/α-$(Al_{0.2}Ga_{0.8})_2O_3$ layers for 30 minutes (the thickness of 150 nm), followed by the growth of an α-Ga_2O_3 main layer for 30 minutes (the thickness of 150 nm).

Table 4.1. Experimental conditions.

	α-Ga_2O_3	α-$(Al_{0.2}Ga_{0.8})_2O_3$	α-$(Al_{0.9}Ga_{0.1})_2O_3$
[Al]		0.09 mol/L	0.14 mol/L
[Ga]	0.020 mol/L	0.03 mol/L	0.02 mol/L
Carrier gas, flow rate	N_2, 1.0 L/min	O_2, 5.0 L/min	O_2, 5.0 L/min
Dilution gas, flow rate	N_2, 0.5 L/min	O_2, 0.5 L/min	O_2, 0.5 L/min
Growth temperature	470ºC	700ºC	700ºC

4.3.2 X-ray Diffraction Measurement

Figure 4.4 shows the reciprocal space map for $\bar{1}\bar{1}29$ reflection. The author attributed the three intense reflection patterns to those from the sapphire substrate, the α-$(Al_{0.9}Ga_{0.1})_2O_3$ layer (on the right side of sapphire), the thick α-$(Al_{0.2}Ga_{0.8})_2O_3$ layer on the buffer layers (below the α-Ga_2O_3 main layer), and the α-Ga_2O_3 main layer judging from their positions although some layers in the buffer may be too weak to be detected. The dashed line intersects the theoretical positions of sapphire and α-Ga_2O_3 $\bar{1}\bar{1}29$ reflections. Apparently, the α-Ga_2O_3 and α-$(Al_{0.2}Ga_{0.8})_2O_3$ layers are lattice-relaxed with respect to the sapphire substrate and the α-Ga_2O_3 layer seems to be subject to slight in-plane compressive strain. On the other hand, in-plane tensile stress acts on the α-$(Al_{0.9}Ga_{0.1})_2O_3$ layer, being strained by the α-$(Al_{0.2}Ga_{0.8})_2O_3$ and α-Ga_2O_3 layers.

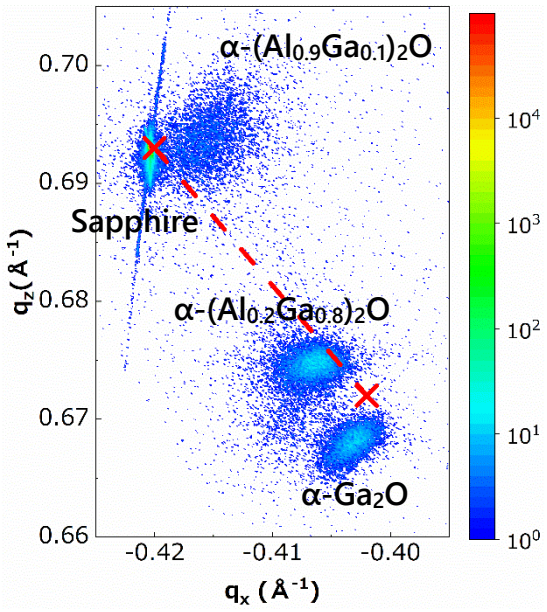

Figure 4.4. Reciprocal space map for x-ray $\bar{1}\bar{1}29$ reflections from the sample with buffer layers.

4.3.3 Transmission Electron Microscopy Observation

Figure 4.5(a) depicts the electron-beam diffraction pattern at the [α-Ga_2O_3/α-$(Al_xGa_{1-x})_2O_3$ buffer layers/sapphire substrate] region observed along the $\langle 10\bar{1}0 \rangle$ axis. The diffraction spots of α-Ga_2O_3 and α-$(Al_{0.2}Ga_{0.8})_2O_3$ appear to be overlapped because the difference in lattice constants between α-Ga_2O_3 and α-$(Al_{0.2}Ga_{0.8})_2O_3$ is small (about 0.7 and 1.0% along c- and a-axes, respectively). Anyway, the diffraction spots of α-Ga_2O_3 [and probably those of α-$(Al_{0.2}Ga_{0.8})_2O_3$] are clearly

situated inside of those of sapphire, indicating that the α-Ga_2O_3 film has the corundum structure and is a single crystal film. The cross-sectional transmission electron microscope (TEM) image at the [α-Ga_2O_3/α-$(Al_xGa_{1-x})_2O_3$ buffer layers/sapphire substrate] region observed along the $\langle 11\bar{2}0\rangle$ zone axis is shown in Fig. 4.5(b). The sample structure consisting of periodic multilayers of α-$(Al_{0.9}Ga_{0.1})_2O_3$ and α-$(Al_{0.2}Ga_{0.8})_2O_3$, as shown in Fig. 4.3, is actually fabricated. The thickness of a unit pair of α-$(Al_{0.9}Ga_{0.1})_2O_3$/α-$(Al_{0.2}Ga_{0.8})_2O_3$ are recognized as about 20 nm, which is nearly same as designed.

Cross-sectional TEM images under two-beam conditions were taken to discuss the dislocation structure of the buffer layers and the α-Ga_2O_3 main layer. Figure 4.6 shows the dark field images of the [α-Ga_2O_3/α-$(Al_xGa_{1-x})_2O_3$ buffer layers/sapphire substrate] region. Figures 4.6(a) and 4.6(b) were observed along the $\langle 11\bar{2}0\rangle$ zone axis with diffraction vector **g** = 0006 and $10\bar{1}0$, respectively. In the image for **g** =$10\bar{1}0$ [Fig. 4.6(b)], edge dislocations are observed and the density of them in the α-Ga_2O_3 thin film is estimated to be 8×10^7 cm^{-2}, while in the image for **g** = 0006 [Fig. 4.6(a)], the density of screw dislocation is calculated as 3×10^8 cm^{-2} using the method of Ham. [49] Figures 4.6(c) and 4.6(d) show cross-sectional TEM images observed along the $\langle 10\bar{1}0\rangle$ zone axis with **g** = 0003 and $11\bar{2}0$, respectively. The 0003 diffraction spot is observed as an extinct spot forbidden by the c-

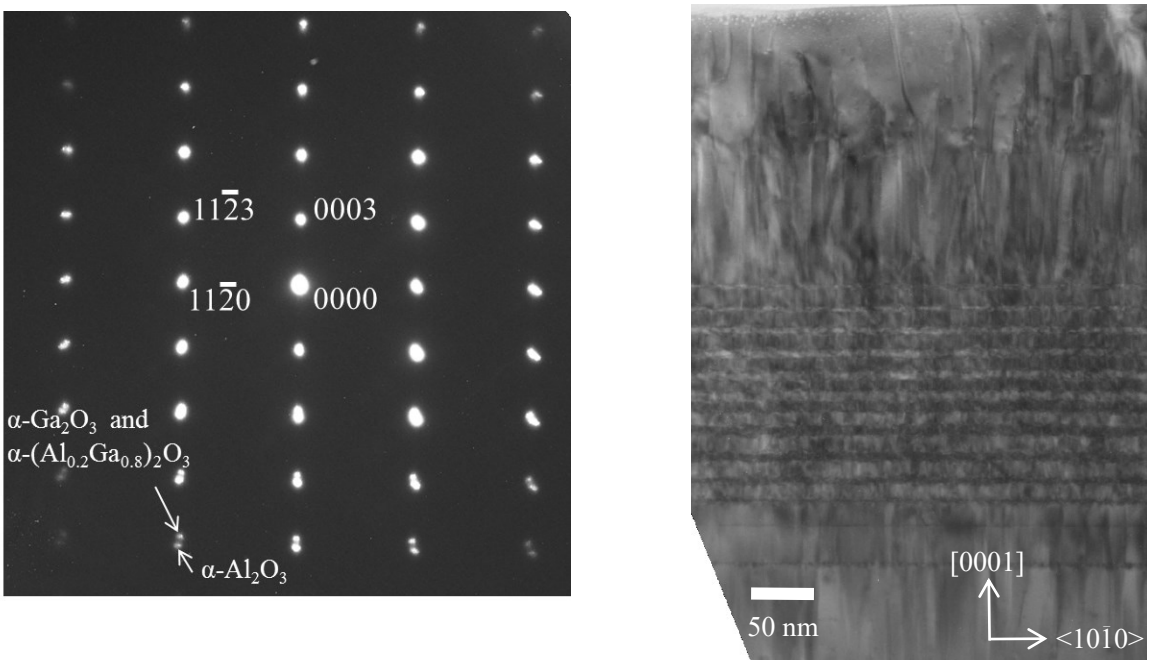

(a) $\langle 10\bar{1}0\rangle$ zone axis (b) $\langle 11\bar{2}0\rangle$ zone axis

Figure 4.5. Transmission electron beam diffraction spots for the [α-Ga_2O_3/α-$(Al_xGa_{1-x})_2O_3$ buffer layers/sapphire] region viewed along $\langle 10\bar{1}0\rangle$ (a) and cross-sectional TEM image of the sample viewed along $\langle 11\bar{2}0\rangle$ zone axis (b).

glide symmetry, that is, $11\bar{2}3 + \bar{1}\bar{1}20 = 0003$ in the $\langle 10\bar{1}0 \rangle$ zone, [50] as shown in Fig. 4.5(a). Therefore, **g** = 0003, which is the closest to the origin, was used. As shown in Fig. 4.6(c), few screw dislocations are confirmed in the α-Ga_2O_3 main layer. By enhancing the contrast of the image in Fig. 4.6(c), the screw dislocations are apparently observed and the density of them is similar to that in the image viewed along the $\langle 11\bar{2}0 \rangle$ zone axis for **g** = 0006 [Fig. 4.4(a)]. On the other hand, in the image for **g** = $11\bar{2}0$ [Fig. 4.6(d)], the dark and bright areas apparently appear owing to the strain. The edge dislocation density in the α-Ga_2O_3 main layer is approximated as 6×10^8 cm^{-2}. In all the obtained images, most of bright-dark contrast areas and lines are seen in the α-$(Al_xGa_{1-x})_2O_3$ buffer layers. It indicates that much dislocations are confined in the buffer layers.

Cross-sectional TEM images showed that the density of dislocations observed along the $\langle 10\bar{1}0 \rangle$ zone axis with **g** = $11\bar{2}0$ [Fig. 4.6(d)] was higher than those observed with **g** = 0003 [Fig. 4.4(c)] or along the $\langle 11\bar{2}0 \rangle$ zone axis [Figs. 4.6(a) and 4.6(b)]. This result is similar to that obtained for the α-Ga_2O_3 directly grown on c-plane sapphire substrates, [30] but it should be noted that the edge dislocation density in the α-Ga_2O_3 thin films was reduced to 6×10^8 cm^{-2} (in the present study) from 7×10^{10} cm^{-2} (in the previous study,[30] in α-Ga_2O_3 directly on sapphire). The graded-buffer layers may concentrate dislocations in the α-$(Al_xGa_{1-x})_2O_3$ buffer layers by gradually changing the average lattice length from the substrate to the α-Ga_2O_3 layer, resulting in the reduction of the edge dislocations in the α-Ga_2O_3 thin films. On the other hand, in the α-Ga_2O_3 thin films on the α-$(Al_xGa_{1-x})_2O_3$ buffer layers, screw dislocations were evidently observed and their density was 3×10^8 cm^{-2}, which was in contrast to the α-Ga_2O_3 grown directly on sapphire where the screw dislocation density was under 10^7 cm^{-2}. In this study, the screw dislocations in the main α-Ga_2O_3 layer probably arise from tilting lattice happened at the heterointerfaces of the multiple layers. On the other hand, for the α-Ga_2O_3 directly grown on sapphire, α-Ga_2O_3 is grown semi-coherently on sapphire with the periodic structure along the $\langle 1\bar{1}00 \rangle$ direction, corresponding to the matching of 20 α-Ga_2O_3 cells and 21 α-Al_2O_3 cells, preventing the generation of screw dislocations.

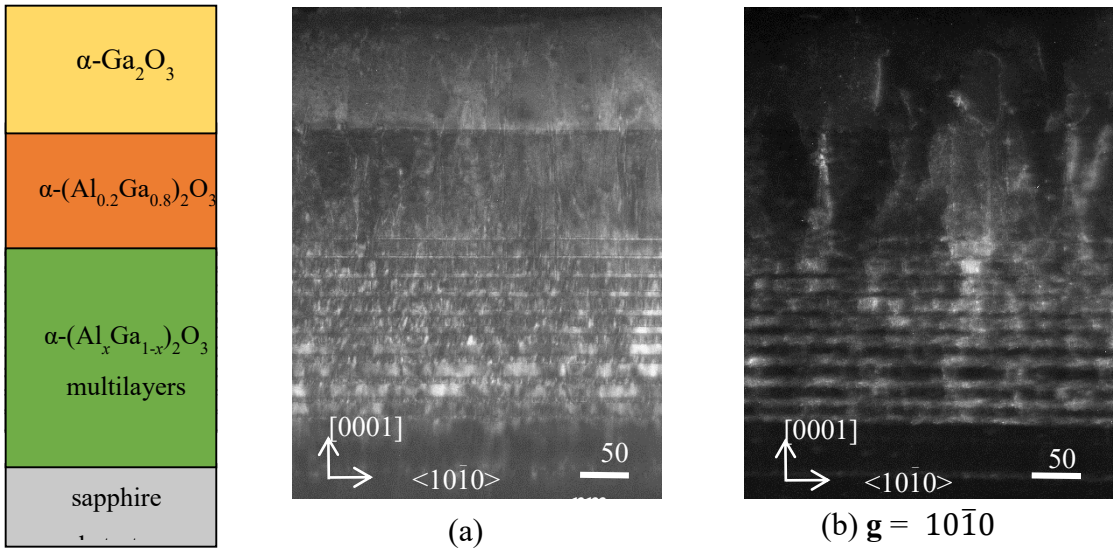

Figure 4.6. Dark-field TEM images observed under two-beam diffraction condition at the [α-Ga_2O_3/α-$(Al_xGa_{1-x})_2O_3$ buffer layers/sapphire] interface. (a) and (b) were taken with the ⟨11$\bar{2}$0⟩ zone axis and titled to diffraction vector **g** = 0006 (a) or 10$\bar{1}$0 (b) . (c) and (d) were with the ⟨10$\bar{1}$0⟩ zone axis and tilted to **g** = 0003 (c) and 11$\bar{2}$0 (d).

4.4 Epitaxial Lateral Overgrowth of α-Ga_2O_3

4.4.1 Experimental Procedures

SiO_2 was adopted as the dielectric mask material for the ELO α-Ga_2O_3. A striped-patterned SiO_2 mask was used to investigate the relation between the direction of stripes with respect to the crystal orientation, and the facet structure and L/V ratio of the ELO α-Ga_2O_3. α-Ga_2O_3 is able to be heteroepitaxially grown on sapphire substrates without nucleation layers by mist-CVD and HVPE unlike GaN. Therefore, the SiO_2 mask was formed directly on sapphire substrates by using a photolithography. The width of stripe windows was 5 μm with a periodicity of 10 μm, as shown in Fig. 4.7. The growth of α-Ga_2O_3 was conducted on c-, m- and a-plane sapphire substrates patterned by the SiO_2 mask whose stripes were along c-, m- and/or a-axes by the mist-CVD method. The growth condition is summarized in Table 4.2. Gallium tri-chloride ($GaCl_3$), which allows the higher growth rate than $Ga(acac)_3$, was adopted as a Ga precursor. The mist-CVD growth of α-Ga_2O_3 using $GaCl_3$ is explained in Chapter 2 in detail. Epitaxial c-, m-, and a-plane α-Ga_2O_3 films were grown on c-, m-, and a-plane sapphire substrates with the in-plane orientations of the films corresponded with those of the substrates. The growth temperature (T_g) was changed between 500 and 700 °C. Nitrogen was used as both carrier and dilution gases.

Table 4.2. Experimental conditions

Substrate	**c-plane sapphire**	**A- and m-plane sapphire**
Ga precursor	$GaCl_3$	
Solvent	H_2O	
HCl	2.4 mol/L	
Ga concentration	0.1 mol/L	0.02 mol/L
Growth temperature T_g	500-700 ºC	600 ºC
Carrier gas (flow rate)	N_2, 4.0 L/min	
Dilution gas (flow rate)	N_2, 0.5 L/min	

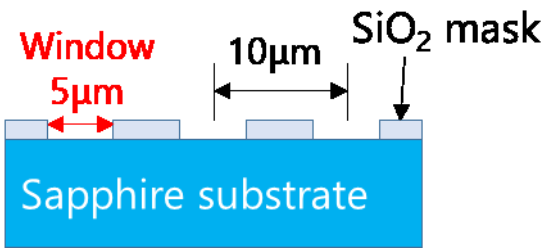

Figure 4.7. Schematic of the SiO_2 mask on a sapphire

4.4.2 Temperature Dependence of SAG α-Ga_2O_3

Scanning electron microscopy (SEM) was used to investigate selective area growth characteristics of the α-Ga_2O_3 on the patterned substrates, facet structures of the selective area grown (SAG) α-Ga_2O_3 and the *L*/*V* ratios. At first, temperature dependence of selective growth was investigated. Figures 4.8(a)-(c) are plane view and cross-sectional SEM images of the SAG α-Ga_2O_3 on c-plane sapphire substrates with the stripe along the $\langle 11\bar{2}0\rangle$, where the α-$Ga_2O_3$ layers were grown at the growth temperature (T_g) of (a) 500, (b) 600, and (c) 700 °C. The α-Ga_2O_3 is selectively grown on the window areas at T_g= 600 and 700 °C, while depositions are observed on the SiO_2 mask at T_g= 500 °C, as shown in Fig. 4.8(a), revealing that the growth temperature higher than 500 °C is required for the SAG α-Ga_2O_3 at the present growth condition. However, the α-Ga_2O_3 grown at 700 °C hs a rough surface morphology with cracks, as shown in Fig. 4.8(c), due to the larger difference in thermal expansion coefficients of α-Ga_2O_3 and sapphire at the higher temperature. [19)]

Figure 4.9 shows symmetric X-ray diffraction (XRD) 2θ/ω scan profiles of the SAG α-Ga_2O_3 on the c-plane sapphire substrate with the $\langle 11\bar{2}0\rangle$-oriented stripe mask. The samples grown at 500 and 600 °C show the α-Ga_2O_3 and sapphire 0006 related reflex, while the sample grown at 700 °C exhibits small peaks from β-Ga_2O_3 $\bar{2}01$ related reflex besides those from α-Ga_2O_3. The α-Ga_2O_3 layers with a micrometer order thickness were obtained at T_g≥600 °C, which is higher than the reported phase transition temperature. This is because the α-Ga_2O_3 is stabilized on the patterned substrates due to less strain in the SAG

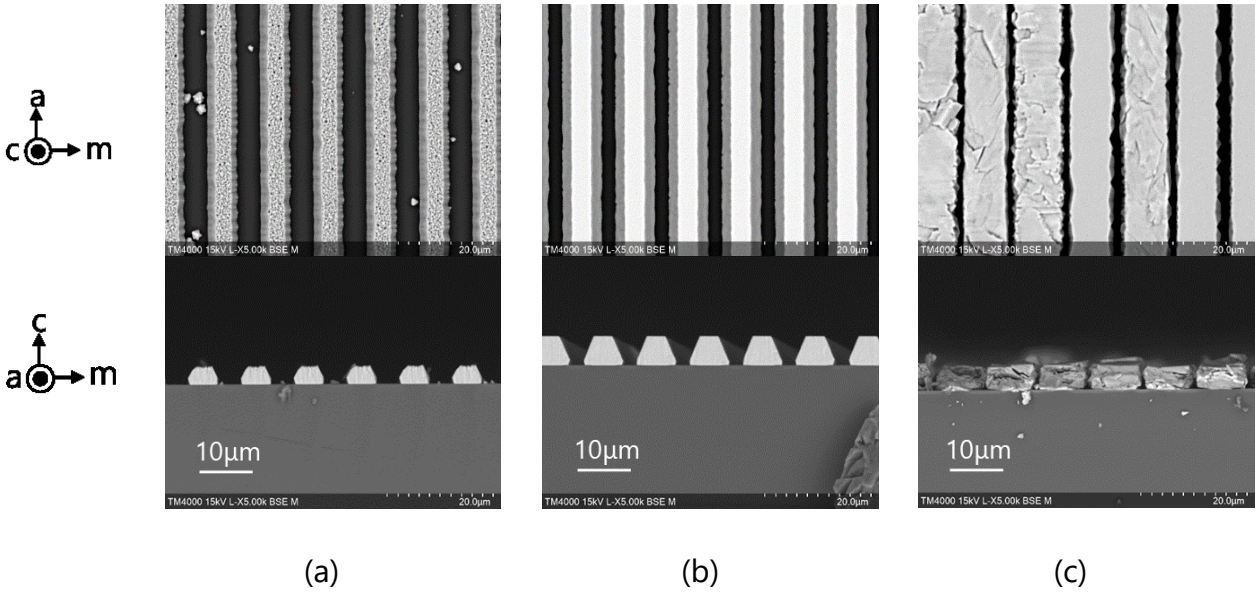

Figure 4.8. Bird's-eye (upper) and cross-sectional (lower) SEM images of ELO Ga_2O_3 on c-plane sapphire with the $\langle 11\bar{2}0\rangle$ stipe grown at (a) 500 °C, (b) 600 °C and (c) 700 °C, respectively.

α-Ga_2O_3 layers. The detail will be discussed in Chapter 6. The same dependence on the growth temperatures was observed for the SAG α-Ga_2O_3 on m- and a-plane sapphire substrates.

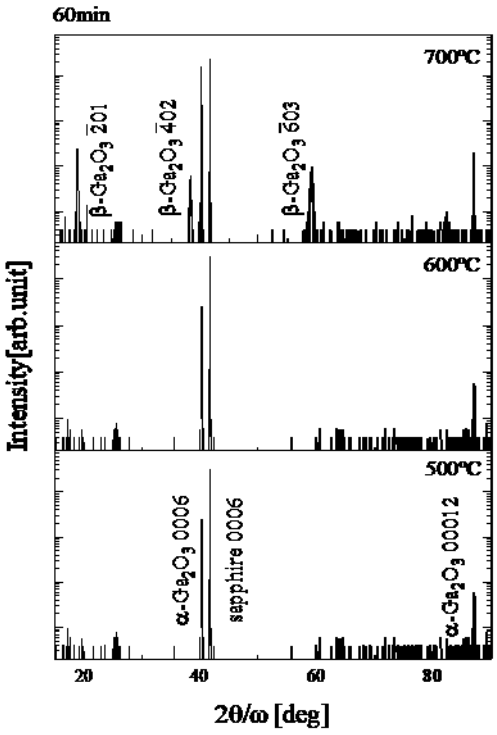

Figure 4.9. Symmetric XRD 2θ/ω scan profiles of the SAG α-Ga_2O_3 on c-plane sapphire with the opening stripes along <11$\bar{2}$0> axis as a function of growth temperatures.

In order to investigate the mechanism of the selective area growth of α-Ga_2O_3 on sapphire substrates using the SiO_2 mask, GaO_x was deposited on quartz (SiO_2) glass substrates.[1] Note that the composition of the film is shown here as GaO_x, since amorphous gallium oxide is formed on SiO_2 and the Ga/O ratio may not always be the stoichiometric value (2/3). The Ga concentration and growth time were set at 0.02 mol/L and 5 min, respectively, which were smaller than those used for the SAG α-Ga_2O_3 (0.1 mol/L and 1 hour) to see the initial nucleation of GaO_x on the substrates. Bird's eye SEM images for the GaO_x on quartz show the nucleation of GaO_x on the quartz glass substrates at T_g between 500 and 700 ºC [Fig. 4.10(a)-(c)], while no depositions on the SiO_2 mask were observed for the SAG α-Ga_2O_3 at T_g= 600 and 700 ºC [Fig. 4.8(b) and 4.8(c)]. These results indicate

[1] Since amorphous gallium oxide is formed on SiO_2, the Ga/O ratio may not always be the stoichiometric value (2/3); so the composition of the film is shown here as GaO_x,

that GaO_x can be deposited on SiO_2, thus, the SAG of α-Ga_2O_3 is not happened by the desorption characteristic of α-Ga_2O_3 on SiO_2. Figure 4.11 explains the expected mechanism of the selective area growth of the α-Ga_2O_3 on the SiO_2 mask. When the SiO_2 mask is patterned on a sapphire substrate, the source materials can diffuse on the SiO_2 mask at enough high temperature (T_g>500 ºC) and all the sources are incorporated into the facet on the window area of the sapphire, following the lateral growth [Fig. 4.11(b)]. In the present study, source materials seem to have enough long diffusion length to reach the window area at T_g>500 ºC, yielding the SAG α-Ga_2O_3. On the other hand, GaO_x is deposited on the quartz glass substrate due to the enough supply to form the initial nucleus. When the growth temperature and growth time are 600 ºC and 1 h, respectively, the cross-sectional area of the SAG α-Ga_2O_3 (the periodicity of 10 μm) is approximated to be 30 μm^2, as estimted from Fig. 4.8(b). The area corresponds with the area of α-Ga_2O_3 on sapphire substrate

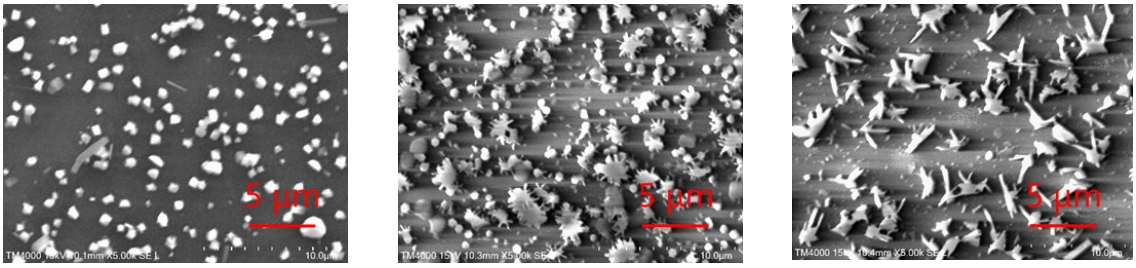

(a) T_g=500 ºC (b) T_g=600 ºC (c) T_g=700

Figure 4.10. Plane-view SEM images of GaO_x on SiO_2 glass substrates grown at (a) 500 ºC, (b) 600 ºC and (c) 700 ºC, respectively.

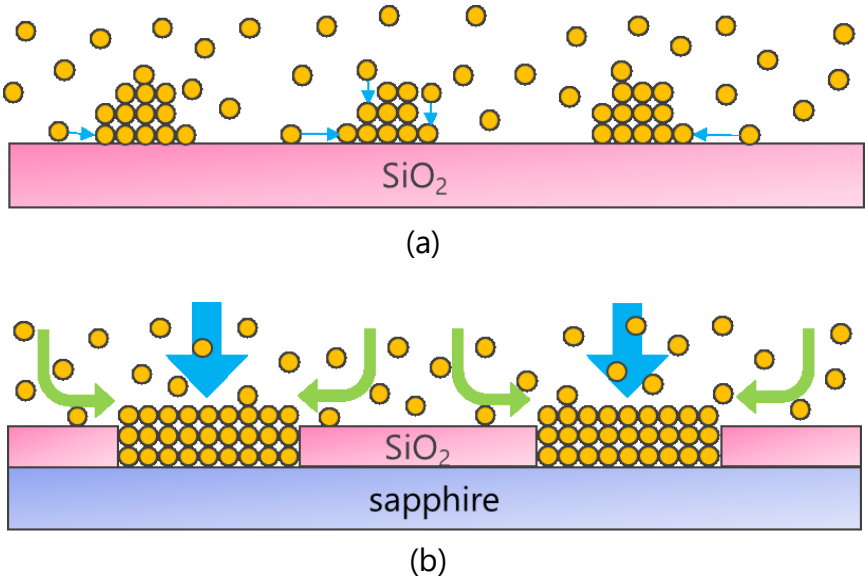

Figure 4.11. Schematics of growth behaviors of (a) GaO_x on SiO_2 and (b) selective area growth of α-Ga_2O_3 on sapphire substrates with a SiO_2 mask.

without patterns as calculated based on the growth rate of 50 nm/min [Fig.2.5 in Chapter 2]. These results support that all sources supplied on the mask region is incorporated into the facets at T_g>500 ºC by the enough long diffusion lengths on the SiO_2 mask.

4.4.3 Dependence of SAG α-Ga_2O_3 on Orientation of Substrates

Due to the cracks introduced before a coalescence of the facets at 700 °C and the deposition on the mask at 500 °C with the mask/window width of 5/5 μm, the growth temperature around 600 °C is suitable for the ELO α-Ga_2O_3. In order to investigate the dependence of facet structures on the mask direction with respect to the orientation of sapphire substrates, α-Ga_2O_3 was grown at 600 °C on c-, m-, and a-plane sapphire substrates with the stripes along c-, m-, and/or a-axes.

C-plane Substrates with the A- and M-axes Stripes

Figures 4.12(a) and 4.12(b) show bird's-eye and cross-sectional SEM images of the SAG α-Ga_2O_3 grown on c-plane sapphire substrates with the $\langle 11\bar{2}0\rangle$ and $\langle 10\bar{1}0\rangle$ stripes, respectively. Triangular stripes with $\{10\bar{1}1\}$ and $\{10\bar{1}2\}$ facets were formed for the $\langle 11\bar{2}0\rangle$ stripe, while a rectangular cross section with a (0001) top facet and $\{11\bar{2}0\}$ sidewalls is observed for the $\langle 10\bar{1}0\rangle$ stripe. The triangle facet can be utilized for the

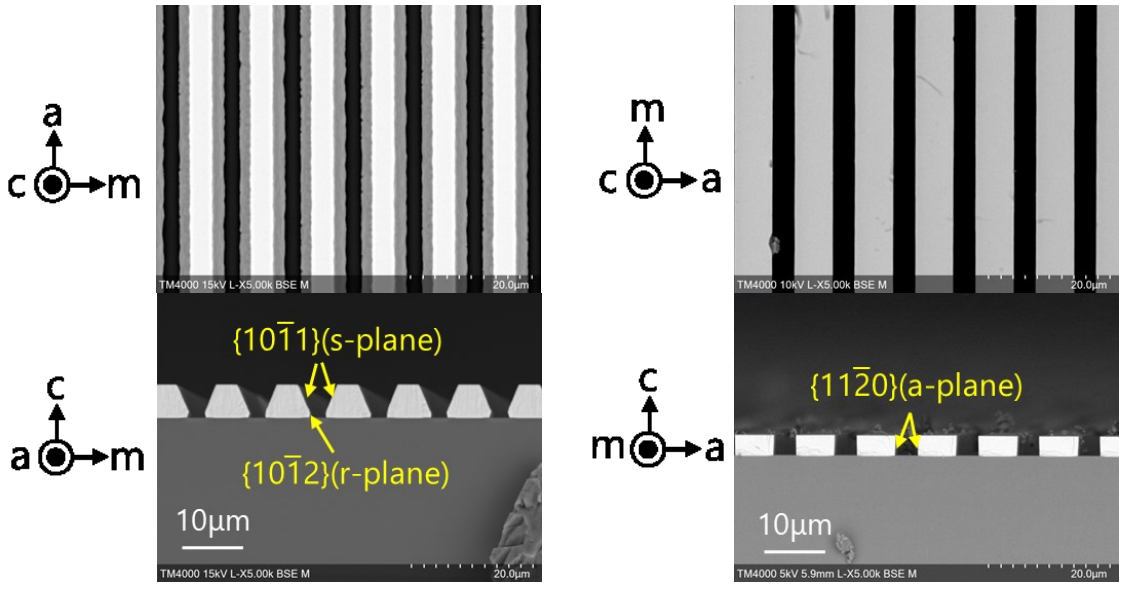

(a) $\langle 11\bar{2}0\rangle$ stripe (b) $\langle 10\bar{1}0\rangle$ stripe

Figure 4.12. Bird's-eye (upper) and cross-sectional (lower) SEM images of the SAG Ga_2O_3 on c-plane sapphire grown at 600 ºC with (a) the $\langle 11\bar{2}0\rangle$ and (b) $\langle 10\bar{1}0\rangle$ stripes.

FACELO. Hiramatsu *et al.* reported that the dislocation density was dramatically dropped to the order of 10^{-6} cm^{-2} in the FACELO process: bending of the dislocations by controlling the facet structure from the inclined triangular one to a flat one. [15] The facet structures of α-Ga_2O_3 on c-plane sapphire with stripes along $\langle 11\bar{2}0 \rangle$ can be changed a triangle to a flat one as well by changing the growth temperature from 600 to 700 °C [Fig.4.8(b) and 4.8(c)]. Therefore, this will be a promising condition to reduce the dislocation density in α-Ga_2O_3 effectively by one process. However, the small *L*/*V* ratio of 0.23 causes the difficulty of the coalescence with the mask width of 5 μm because of the introduction of cracks or exfoliations before the coalescence. Here, the *L*/*V* ratio was determined as shown in Fig. 4.13. The smaller widths of openings and masks will enable the coalescences and lead to the reduction of the dislocation density in future works.

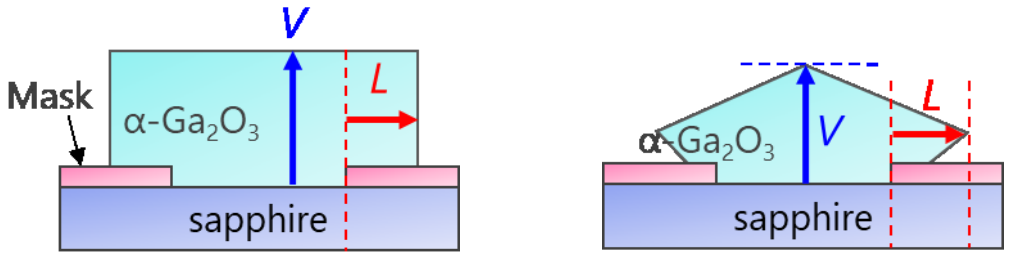

Figure 4.13. Schematics of the SAG α-Ga_2O_3 on sapphire substrates.

M-plane Substrates with A- and C-axes Stripes

As shown in Fig. 4.14(a), a triangular stripe with $\{10\bar{1}1\}$ and $\{10\bar{1}2\}$ facets is formed for the $\langle 11\bar{2}0 \rangle$ stripe. These facets of $\{10\bar{1}1\}$ and $\{10\bar{1}2\}$ are the same planes observed for the same opening axis of $\langle 11\bar{2}0 \rangle$ for the c-plane sapphire [Fig. 4.12(b)]. These results indicate that surface energies of $\{10\bar{1}1\}$ and $\{10\bar{1}2\}$ of α-Ga_2O_3 are lower than that of the {0001} in the present condition. On the other hand, a trapezoidal cross section with a $\{10\bar{1}0\}$ top and $\{11\bar{2}0\}$ facets is observed for the <0001> stripe [Fig. 4.14(b)].

A-plane Substrates with M- and C-axes Stripes

A trapezoidal stripe with the $\{11\bar{2}0\}$ facets is observed for the $\langle 0001 \rangle$ stripe [Fig.4.15 (a)], while a rectangular cross section with (0001) sidewalls is grown for the $\langle 10\bar{1}0 \rangle$ stripe [Fig.4.15(b)]. These facets are corresponding to the $\langle 0001 \rangle$ stripe on the m-plane sapphire and the $\langle 10\bar{1}0 \rangle$ stripe on the c-plane sapphire [Fig.4.14(b) and Fig.4.12(b)].

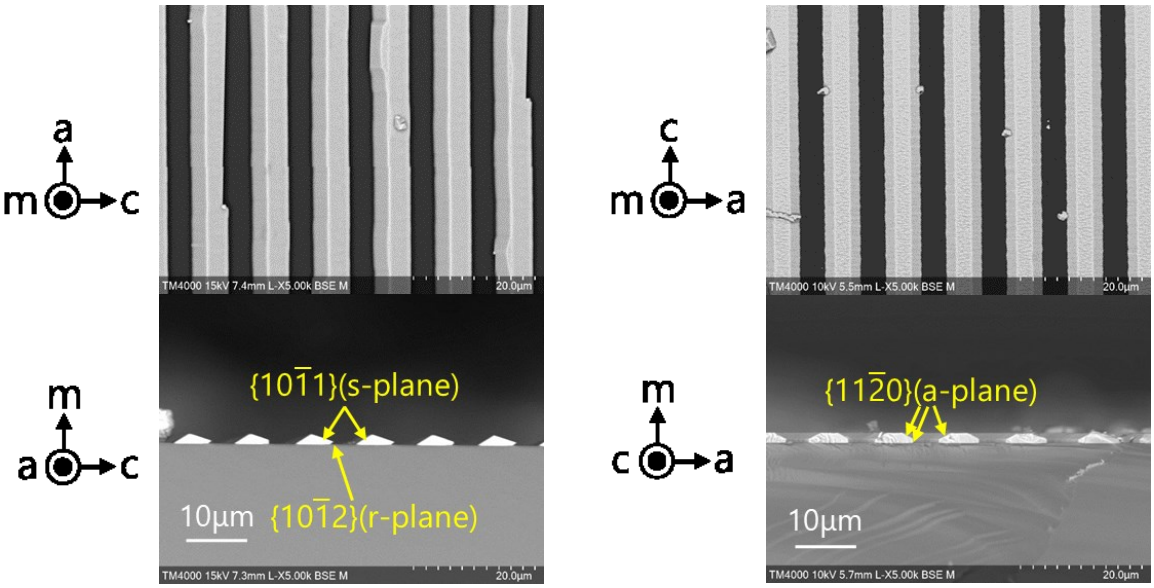

(a) ⟨11$\bar{2}$0⟩ stripe (b) <0001> stripe

Figure 4.14. Bird's-eye (upper) and cross-sectional (lower) SEM images of the SAG Ga_2O_3 on m-plane sapphire grown at 600 ºC with (a) the ⟨11$\bar{2}$0⟩ and (b) ⟨0001⟩ stripes.

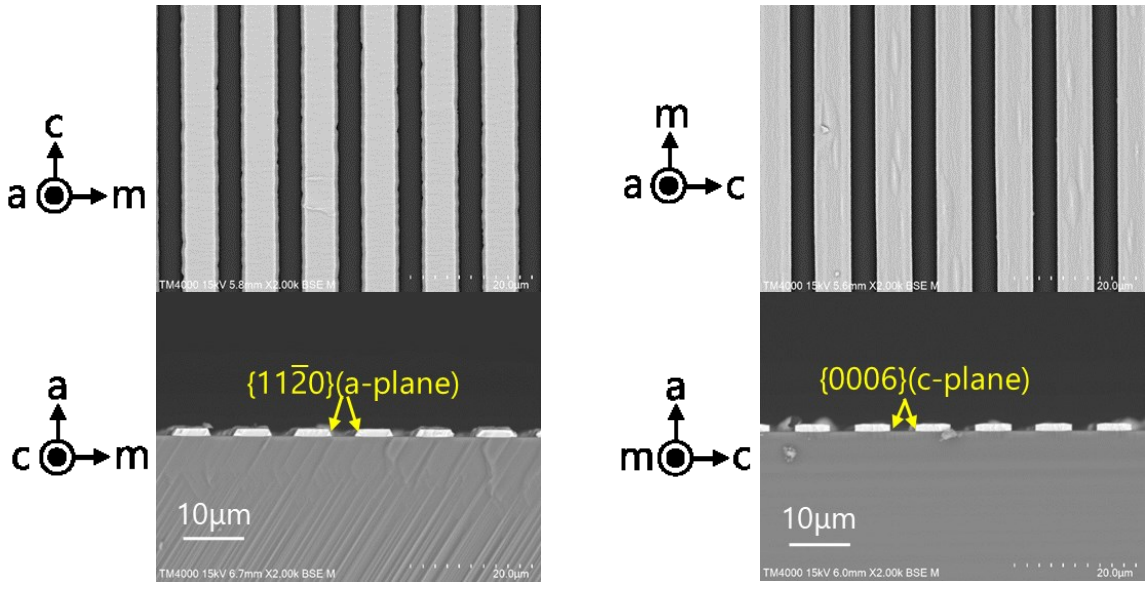

(a) ⟨0001⟩ stripe (b) ⟨10$\bar{1}$0⟩ stripe

Figure 4.15. Bird's-eye (upper) and cross-sectional (lower) SEM images of the SAG Ga_2O_3 on a-plane sapphire grown at 600 ºC with (a) ⟨0001⟩ and (b) the ⟨10$\bar{1}$0⟩ stripes.

Summary

Table 4.3 summarizes the SAG α-Ga_2O_3 on the c-, m-, and a-plane sapphire substrates. The shapes of the SAG α-Ga_2O_3 depended on the orientations of substrates and the direction of the stripes, but all the facets consisted of the basal (c) $\{0001\}$, rhombohedral (r) $\{10\bar{1}2\}$, prismatic (a) $\{1\bar{2}10\}$ and structural rhombohedral (s) $\{10\bar{1}1\}$ except for the prismatic (m) $\{10\bar{1}0\}$ facet on the m-plane sapphire with the $\langle 11\bar{2}0\rangle$ stripe where the $\{10\bar{1}0\}$ top facet was not buried by the inclined a-plane facets [Fig. 4.14(b)]. C-, r-, a- and s-planes are same as the equilibrium facets of cavity in sapphire annealed at 1600 and 1800 °C reported by Choi *et al.* and Kitayama *et al.*, where m-plane, identified as a low energy plane of sapphire in some 0 K lattice simulations, was not observed at either temperature.[20,21] These planes in α-Ga_2O_3 are considered to be stable as well because of the same corundum structure.

The *L*/*V* ratios of the SAG α-Ga_2O_3 were determined as depicted in the Fig. 4.15. The SAG α-Ga_2O_3 on the a-plane substrates showed approximately 4 times as large *L*/*V* ratio as those on c- and m-plane substrates. The SAG α-Ga_2O_3 on the a-plane substrate with the $\langle 10\bar{1}0\rangle$-oriented stripe mask had the largest *L*/*V* ratio of 0.96. The fast lateral growth rate along c-axis indicates that c-plane takes higher surface energy than the other stable planes (r, s, a-planes) in the growth condition, which is consistent with the result of the ELO α-Ga_2O_3 on c-plane sapphire substrates that the c-plane top was buried into the r- and s-plane facets [Fig. 4.12(a)]. From viewpoints of a small mask fill factor, the ELO α-Ga_2O_3 on the a-plane substrate with the largest *L*/*V* ratio is suitable for the ELO α-Ga_2O_3.

Table 4.3. Summary of the SAG α-Ga_2O_3 on c-, m-, and a-plane sapphire substrates with SiO_2 masks.

plane	opening	Lateral axis	Facet structure	Facet planes	*L*/*V* ratio
c	**m**	a	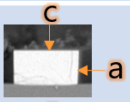	a, c	0.20
	a	m	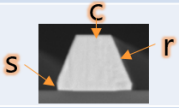	r, s, c	0.23
m	**c**	a	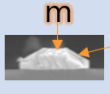	m, a	0.27
	a	c		r, s	0.37
a	**m**	c	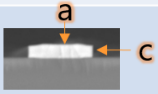	a, c	0.96
	c	m		a	0.93

4.4.4 Epitaxial Lateral Overgrown α-Ga_2O_3 on A-Plane Sapphire

By using the a-plane sapphire substrate with the ⟨10$\bar{1}$0⟩-oriented stripe mask, the full coalescence was achieved by growing for 2 hours, as shown in Fig. 4.16(a). The growth temperature of 550 °C was used since cracks were introduced in the α-Ga_2O_3 layer before a coalescence occurred at T_g= 600 °C. Figure 4.16(b) shows the symmetric XRD 2θ/ω scan spectrum of the ELO α-Ga_2O_3 on the a-plane sapphire substrate with the ⟨10$\bar{1}$0⟩-oriented stripe mask. The spectra exhibits peaks originated from α-Ga_2O_3 11$\bar{2}$0 without any other peaks, meaning there is no inclusion of the different phases or domains in the ELO α-Ga_2O_3. The SAG α-Ga_2O_3 on c- and m-plane sapphire substrates also did not show the diffraction peaks from other phases or domains unlike the ELO α-Ga_2O_3 by HVPE. [22)]

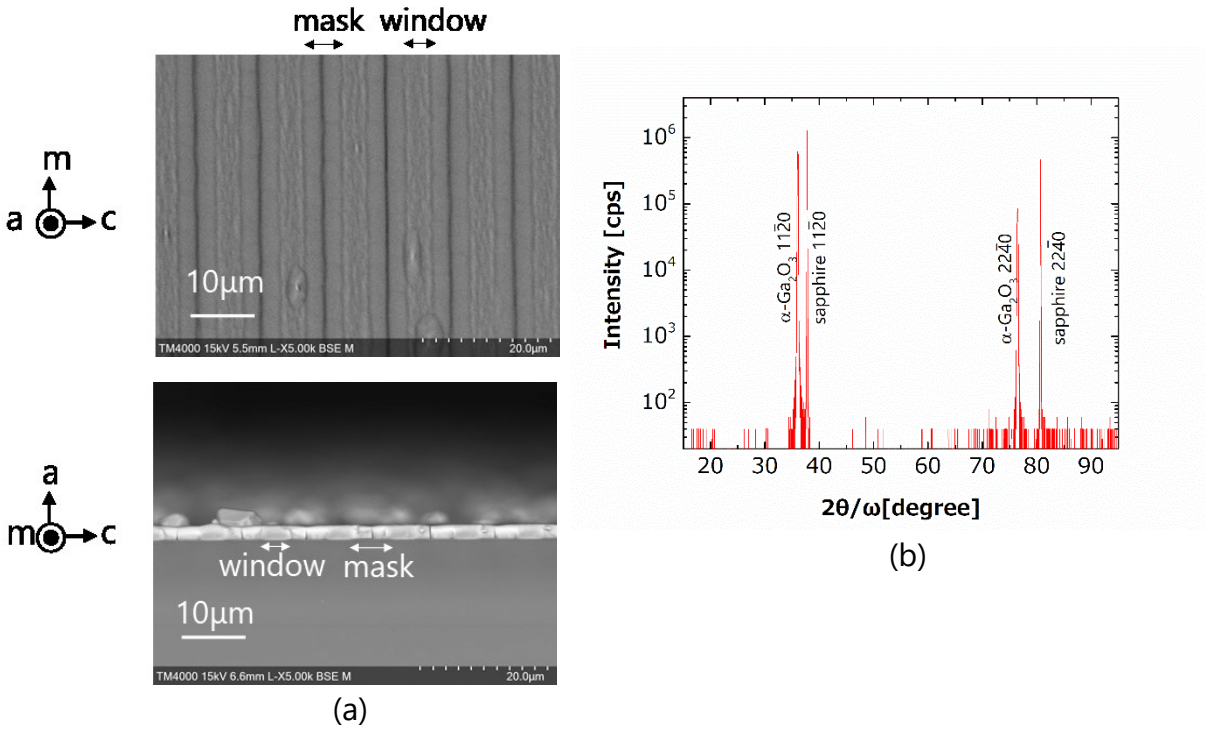

Figure 4.16. (a) Bird's-eye (upper) and cross-sectional (lower) SEM images of ELO Ga_2O_3 on the a-plane sapphire substrate with the ⟨10$\bar{1}$0⟩ stipe grown at 550 °C. Something on the surface of the cross-sectional view may be a fraction of the sample formed in the cleavage process. (b) Symmetric XRD 2θ/ω scan spectra of ELO α-Ga_2O_3 grown on the a-plane sapphire substrate for 3 hours, suggesting successful formation of α-Ga_2O_3.

The cross-sectional TEM observation was conducted for the ELO α-Ga_2O_3 on the a-plane sapphire with the $\langle 10\bar{1}0\rangle$-oriented stripe mask, as shown in Fig. 4.17. The α-Ga_2O_3 was grown for 4 hours to achieve the full coalescence. Figure 4.17(a) reveals that the sharp triangular voids with the height of ca. 1.5 μm remain behind in the coalescence region. The voids are likely to be formed by tilting of the facets on the mask area or less supply of the source to the gap between the facets.

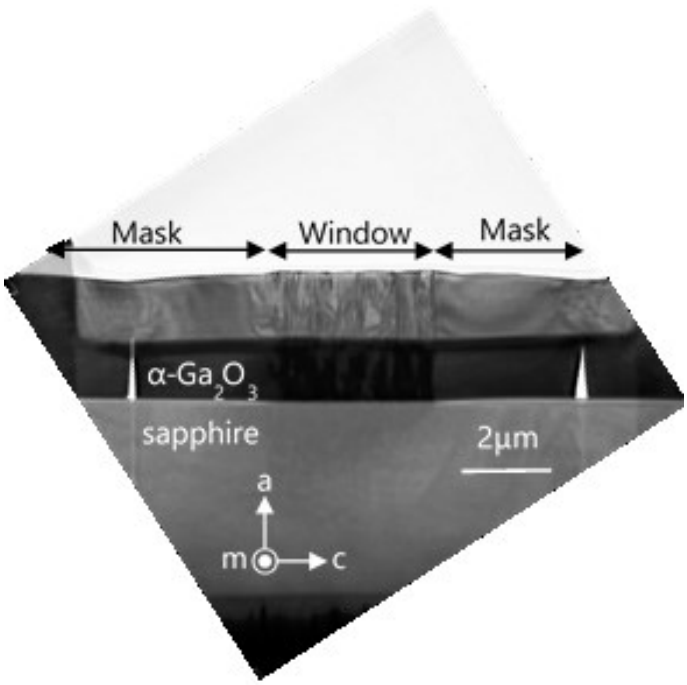

(a)

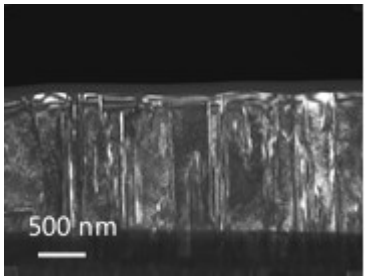

(b) **g**=$11\bar{2}0$ (window region)

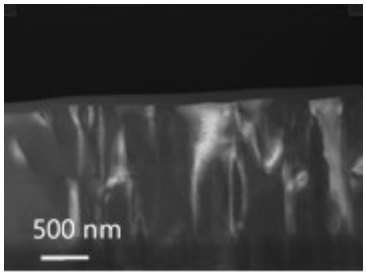

(c) **g**=0003 (window region)

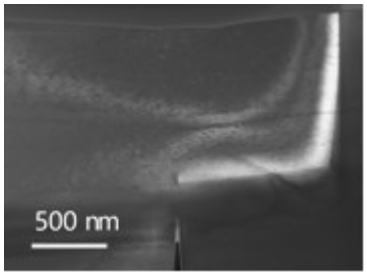

(d) **g**=0003 (mask region)

Figure 4.17. (a) Cross-sectional bright field TEM images of ELO of α-Ga_2O_3 grown on a-plane sapphire substrates at 550 ℃ with the direction of the stripe along $\langle 10\bar{1}0\rangle$ axis. (b) and (c) are the dark field images under two-beam diffraction at the window area in (a) with (b) **g**=$11\bar{2}0$ and (c) **g**=0003. (d) is the dark field images at the coalescence region in the framework shown in (a) with **g**=0003. The color contrast between the upper half and lower half region of the α-Ga_2O_3 layer was due to the different thickness caused in the sample preparation process for the TEM observation.

On the window area, the contrast due to the high density of dislocations is observed, while dislocations generated on the SiO_2 mask are not detected from the cross-sectional TEM image [Fig. 4.17(a)]. On the other hand, the density of dislocations above the window area was estimated to be on the order of 10^{10} cm^{-2} from a plane-view TEM image. As shown in Figs. 4.17(b) and (c), a dark field image of the α-Ga_2O_3 in the window region with $\mathbf{g}=11\bar{2}0$ shows clear white lines originated from the dislocations, while a low contrast due to the strain in the α-Ga_2O_3 is observed for $\mathbf{g}=0003$. These results indicate that there are screw dislocations above the window area in the ELO α-Ga_2O_3 on the a-plane sapphire substrate. On the other hand, a dislocation with $\mathbf{g}=0003$ is introduced just above the void at the coalescence boundary, as shown in Fig. 4.17(d).

In order to discuss the behavior of the dislocation introduced at the coalescence boundary, plane-view TEM images of the ELO α-Ga_2O_3 above the mask region were taken. Figure 4.18(a) reveals that the dislocations are introduced at the coalescence boundary at an interval of a few hundred nm. Figures 4.18(b) and 4.18(c) show the dark field images under two-beam conditions with $\mathbf{g}=0003$ and $10\bar{1}0$, respectively. In the image for $\mathbf{g}=0003$, the dislocations are clearly observed, meaning that the dislocations have the Burgers vector along the $\langle 0001 \rangle$ axis. The endpoints of the dislocations show pits, indicating that the dislocations are bent to 90 degrees there and turned into the threading dislocations. These results are consistent with the results of the cross-sectional TEM observation [Fig. 4.17(d)].

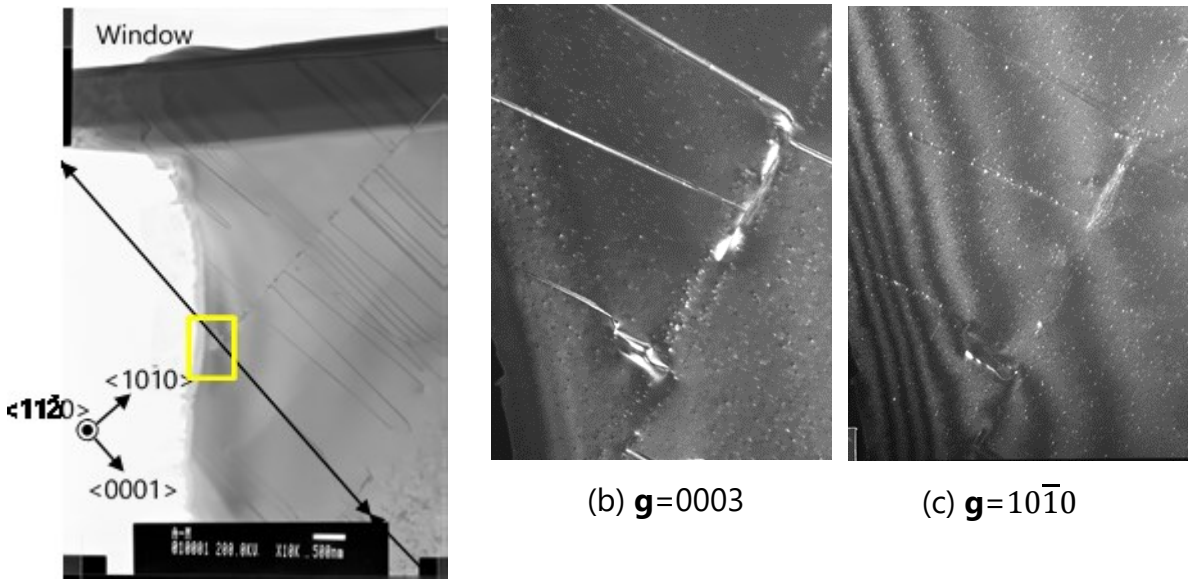

(a) (b) $\mathbf{g}=0003$ (c) $\mathbf{g}=10\bar{1}0$

Figure 4.18. (a) Plane view bright field TEM images of ELO of α-Ga_2O_3 grown on a-plane sapphire substrates at 550 ℃ with the $\langle 10\bar{1}0 \rangle$ stripe. (b) and (c) are the dark field images under two-beam diffraction with (b) $\mathbf{g}=10\bar{1}0$ and (c) $\mathbf{g}=0006$ in the framework shown in (a).

Figure 4.19 shows the schematic of the behavior of the dislocations in the ELO α-Ga_2O_3 on the a-plane sapphire substrate with the $\langle 10\bar{1}0\rangle$-oriented stripe mask. In this condition, the rectangular cross section with the (0001) sidewalls was observed, allowing the largest *L*/*V* ratio of 0.96. Although the inclined facets could help a dramatic reduction of the dislocation density like the FACELO GaN, the two ELO process using rectangular facets is also a promising way to reduce the dislocation density in α-Ga_2O_3; in that process, the dislocation concentrated region above the window area are covered by the second mask. Above the window area, there are the threading screw dislocations whose density was the order of 10^{10} cm^{-2}. In the previous study on the dislocations in the α-Ga_2O_3 film grown on a c-plane sapphire substrate, the edge dislocations generated in the particular plane of $\{\bar{2}110\}$ was reported.[1)] Therefore, α-Ga_2O_3 is considered to have the slip direction of $\langle 11\bar{2}0\rangle$, as hexagonal closed-packed crystals usually do. On the other hand, the dislocations with the Burgers vector along $\langle 0001\rangle$ axis were observed above the mask region. The dislocations seem to arise from a misalignment of facets at the coalescence boundary. Then, they turned upward probably due to the repulsion forced by the screw dislocations above the window area.

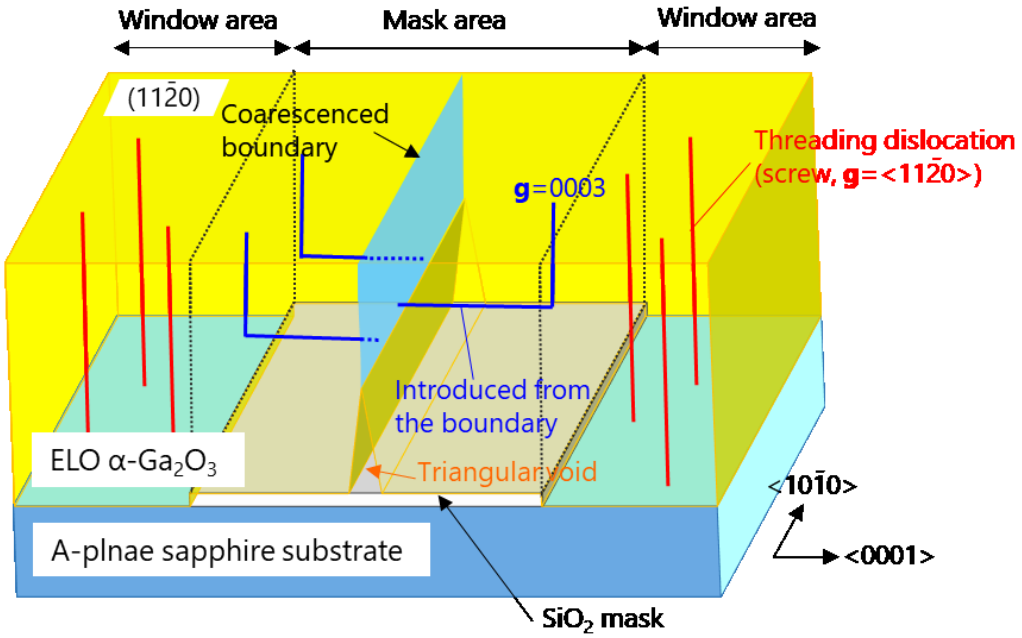

Figure 4.19. Schematic of the dislocations in the ELO α-Ga_2O_3 on a-plane sapphire substrates with the $\langle 11\bar{2}0\rangle$ stipes.

4.5 Summary

Corundum-structured α-Ga_2O_3 thin films were grown using α-$(Al_xGa_{1-x})_2O_3$ buffer layers on c-plane sapphire substrates, and using the epitaxial lateral overgrowth techniques in order to reduce the dislocation density in α-Ga_2O_3 on sapphire.

By introducing the quasi-graded buffer layers, the edge dislocation density in the α-Ga_2O_3 layer was successfully reduced by more than two order of magnitude, compared with α-Ga_2O_3 directly on sapphire. The densities of screw and edge dislocations were about 3×10^8 and 6×10^8 cm^{-2}, respectively. The total density of dislocations was successfully decreased from 7×10^{10} cm^{-2} (in an α-Ga_2O_3 thin film directly grown on a sapphire substrate) to 9×10^8 cm^{-2} by more than one orders of magnitude. However, it should be noted that the screw dislocation density was increased compared to that without the buffer layers.

Secondly, the ELO α-Ga_2O_3 on sapphire was investigated on the c-, m-, and a-plane sapphire substrates with the different mask directions by adopting SiO_2 as the mask material. α-Ga_2O_3 was selectively grown on the window areas without any deposition on the mask at $T_g\geq550$ °C. The shapes of the SAG α-Ga_2O_3 depended on the orientations of substrates and the direction of stripes, but all the facets consisted of the c-, r-, a- and s-planes, indicating these planes have lower surface energies in the growth condition. The ELO α-Ga_2O_3 grown on the a-plane sapphire substrates with the $\langle10\bar{1}0\rangle$-oriented stripe mask showed the rectangular facet structure and the largest L/V ratio of 0.96 due to the (0001) sidewalls having the higher surface energy than the other stable planes. Above the window area, the screw dislocations were observed, while the dislocations with the Burgers vector along $\langle0001\rangle$ axis (the lateral growth direction) were generated from the coalescence boundary probably due to the misalignment of facets at the boundary. The dislocations generated at the coalescence boundary were bent to 90 degrees at the edge of the mask area, turning into the threading dislocations. The bend may arise from a repulsive force between the dislocations and those above the window area. By using the second mask which is formed on the first window area and has a slightly wider mask width than that of the first window to cover the dislocations on the window area as well as those at the edge of the mask generated from the coalescence boundary, the low dislocation density can be achieved in future works.

The reduction of dislocations by the two methods will allow the improvements of electric properties of α-Ga_2O_3, leading to attractive device performance using inexpensive and large-area sapphire substrates. However, the effects of these dislocations on the electrical properties are not studied at the present stage, and it is necessary to identify the type of dislocations which cause fatal problems against electric properties.

References

1) K. Kaneko, H. Kawanowa, H. Ito, and S. Fujita, Jpn. J. Appl. Phys. **51**, 020201 (2012).
2) M. Akiyama, Y. Kawarada, and K. Kaminishi, J. Cryst. Growth **68**, 21 (1984).
3) H. Amano, M. Iwaya, T. Kashima, M. Katsuragawa, I. Akasaki, J. Han, S. Hearne, J.A. Floro, E. Chason, and J. Figiel, Jpn. J. Appl. Phys. **37**, L1540 (1998).
4) T. Soga, S. Hattori, S. Sakai, M. Takeyasu, and M. Umeno, Electron. Lett. **20**, 916 (1984).
5) D.E. Grider, J. Vac. Sci. Technol. B Microelectron. Nanom. Struct. **8**, 301 (1990).
6) I. Mathews, D. O'Mahony, A. Gocalinska, M. Manganaro, E. Pelucchi, M. Schmidt, A.P. Morrison, and B. Corbett, Appl. Phys. Lett. **102**, 033906 (2013).
7) Y.-C. Xin, L.G. Vaughn, L.R. Dawson, A. Stintz, Y. Lin, L.F. Lester, and D.L. Huffaker, J. Appl. Phys. **94**, 2133 (2003).
8) E. Tournié, L. Cerutti, J.-B. Rodriguez, H. Liu, J. Wu, and S. Chen, MRS Bull. **41**, 218 (2016).
9) R.M. France, F. Dimroth, T.J. Grassman, and R.R. King, MRS Bull. **41**, 202 (2016).
10) H. Ito, K. Kaneko, and S. Fujita, Jpn. J. Appl. Phys. **51**, 100207 (2012).
11) A. Usui, H. Sunakawa, A. Sakai, and A.A. Yamaguchi, Jpn. J. Appl. Phys. **36**, L899 (1997).
12) O.-H. Nam, M.D. Bremser, T.S. Zheleva, and R.F. Davis, Appl. Phys. Lett. **71**, 2638 (1997).
13) H. Matsushima, M. Yamaguchi, K. Hiramatsu, and N. Sawaki, J. Cryst. Growth **189**–**190**, 78 (1998).
14) K. Hiramatsu, K. Nishiyama, A. Motogaito, H. Miyake, Y. Iyechika, and T. Maeda, Phys. Status Solidi **176**, 535 (1999).
15) K. Hiramatsu, K. Nishiyama, M. Onishi, H. Mizutani, M. Narukawa, A. Motogaito, H. Miyake, Y. Iyechika, and T. Maeda, J. Cryst. Growth **221**, 316 (2000).
16) D. Shinohara and S. Fujita, Jpn. J. Appl. Phys. **47**, 7311 (2008).
17) T. Kawaharamura, Dang, Giang T., and N. Nitta, Appl. Phys. Lett. **109**, 151603 (2016).
18) S.-D. Lee, Y. Ito, K. Kaneko, and S. Fujita, Jpn. J. Appl. Phys. **54**, 030301 (2015).
19) L.J. Eckert and R.C. Bradt, J. Am. Ceram. Soc. **56**, 229 (1973).
20) J.-H. Choi, D.-Y. Kim, B.J. Hockey, S.M. Wiederhorn, C.A. Handwerker, J.E. Blendell, W.C. Carter, and A.R. Roosen, J. Am. Ceram. Soc. **80**, 62 (1997).
21) M. Kitayama and A.M. Glaeser, J. Am. Ceram. Soc. **85**, 611 (2004).
22) Y. Oshima, K. Kawara, T. Shinohe, T. Hitora, M. Kasu, and S. Fujita, APL Mater. **7**, 022503 (2019).

Chapter 5

Growth of α-Ga_2O_3 and α-$(Al_xGa_{1-x})_2O_3$ on Sapphire Substrates by Plasma-Assisted Molecular Beam Epitaxy

5.1 Introduction

From the perspective of synthesizing heterostructure, molecular beam epitaxy (MBE) is a promising method to control alloy compositions and make a sharp interface. [1–5] However, the research on the MBE growth of α-Ga_2O_3 and α-$(Al_xGa_{1-x})_2O_3$ is still in the early stages since the growth of the α-Ga_2O_3 has been suffered from forming β-Ga_2O_3 especially on a c-plane sapphire substrate. [6,7] In 2018, Kracht *et al*. reported the growth of α-Ga_2O_3 on an r-plane sapphire substrate with a film thickness of 217 nm. [8] They concluded that after c-plane facets were formed on the surface of the α-Ga_2O_3 film, β-Ga_2O_3 appeared with the epitaxial relationship of 0001 α-Ga_2O_3 and $\bar{2}01$ β-Ga_2O_3, suggesting the c-plane facet enhanced the growth of β-Ga_2O_3 in the MBE growth. From these results, a perpendicular plane to c-plane such as a- or m-planes could be suitable for the growth of α-Ga_2O_3. In fact, the Nb-doped α-$(Ga_xAl_{1-x})_2O_3$ and α-Ga_2O_3 with the film thickness of 14 nm were demonstrated on a-plane sapphire in the previous study. [7,9] The epitaxial lateral overgrown (ELO) α-Ga_2O_3 on a-plane sapphire via mist-chemical vapor deposition (mist-CVD) also showed the promising result, as shown in Chapter 4. On the other hand, there is less report on α-$(Al_xGa_{1-x})_2O_3$ on m-plane sapphire using MBE. Kumaran *et al.* referred to Nb-doped α-Ga_2O_3 on m-plane sapphire, but its properties were not discussed in detail there. [9] Although the coalescence of the SAG α-Ga_2O_3 on m-plane sapphire was not achieved at the present stage, Sn-doped α-Ga_2O_3 films on m-plane sapphire grown by mist-CVD has showed high mobility of 65 $cm^2/V\ s$ (n=1.2 × 10^{18} cm^{-3}), [10] suggesting the promising electric properties of α-$(Al_xGa_{1-x})_2O_3$ on m-plane sapphire. This chapter explores the potential of m-plane substrates by reporting the growth of α-$(Al_xGa_{1-x})_2O_3$ on the m-plane sapphire by plasma-assisted MBE (PAMBE) and its bandgap engineering.

5.2 Experimental Procedures

α-$(Al_xGa_{1-x})_2O_3$ ($0 \leqq x \leqq 1$) films were grown on double polished m-plane $(10\bar{1}0)$ sapphire substrates in a Veeco Gen930 PAMBE system equipped with standard effusion cells for elemental Ga and Al, and a radio frequency (RF) plasma source for an active oxygen species. The input RF power and oxygen flow rate were fixed at 250W and 0.50 sccm, respectively, giving the pressure of the growth chamber of ca. 8×10^{-6} Torr during the growth runs.*[1] First, α-Ga_2O_3 films were grown at a substrate thermocouple temperature (T_{sub}) of 650 °C for an hour by varying the beam equivalent pressure (BEP) of Ga from 1.1 $\times10^{-8}$ to 8.2×10^{-8} Torr to obtain the growth rate as a function of the Ga BEP. α-$(Al_xGa_{1-x})_2O_3$ and α-Al_2O_3 films were grown for two hours at T_{sub} of 650 and 750 °C, respectively. The Al concentration (x) in the films was varied from 0 to 1 by regulating the BEPs of Ga [(0–1.1) $\times10^{-8}$ Torr] and Al [(0-1.5) $\times10^{-8}$ Torr]. Structural properties and surface morphology of the samples were characterized by x-ray diffraction (XRD) measurements, cross-sectional scanning transmission electron microscopy (STEM) observations, and atomic force microscopy (AFM). The film thicknesses of the samples were determined by x-ray reflectivity (XRR) measurements. x was estimated by XRD and x-ray photoelectron spectroscopy (XPS). Optical bandgaps E_g of the films were obtained by analyzing the optical transmission spectra using a custom-built far ultraviolet (FUV) spectrophotometer; a m-plane sapphire substrate was used as a reference sample.

5.3 Growth of α-Ga_2O_3 on M-plane Sapphire Substrate

Figure 5.1(a) shows the growth rate of the α-Ga_2O_3 films as a function of the Ga BEPs. For Ga BEPs lower than 2.1×10^{-8} Torr, the growth rate increases in proportion to the Ga BEP, being limited by the Ga supply (O-rich regime). On the other hand, the growth rate does not change when the Ga BEP is between 2.1×10^{-8} and 6×10^{-8} Torr. For Ga BEPs higher than 6×10^{-8} Torr, the growth rate drops to almost zero. The saturation and drop of the growth rate is due to the formation of volatile suboxide (Ga_2O), which has been reported earlier in the study on the MBE growth of β-Ga_2O_3, ε-Ga_2O_3, and α-Ga_2O_3 on r-plane sapphire. [8,11,12] Figure 5.1(b) shows a logarithmic plot of symmetric XRD 2θ/ω scan for the α-Ga_2O_3 film at the Ga BEP of 2.0×10^{-8} Torr. The wide scanning for θ from 15 to 90° reveals the diffraction peaks from $30\bar{3}0$ reflexes of α-Ga_2O_3 and sapphire at 2θ=64.68 and 68.2°. The absence of any other peaks indicates that α-Ga_2O_3 is isomorphically stabilized on m-plane

*[1] This study adopts Torr as a unit of pressure due to the digital display of Torr in the vacuum guage. The vacuum in Torr can be converted to Pa of the International System of Units by 1Torr= 133Pa.

sapphire by overcoming the energy difference between corundum and monoclinic and preventing the formation of the c-plane facets, which contributes the inclusion of the β-phase, as describe in Section 5.1.

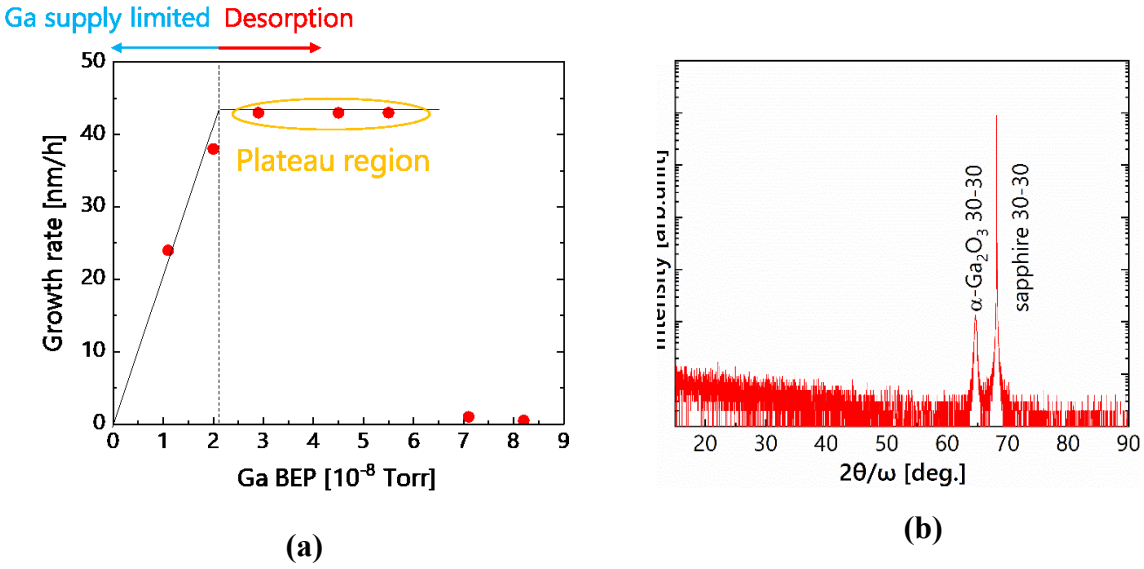

Figure 5.1. (a) Growth rate of α-Ga_2O_3 as a function of Ga BEPs. (b) is a symmetric XRD 2θ/ω scan profile of α-Ga_2O_3 film grown on m-plane sapphire at the Ga BEP of 2.0×10^{-8} Torr.

Table 5.1. The Al and Ga BEPs, film thicknesses, and growth rates of the α-$(Al_xGa_{1-x})_2O_2$ films on m-plane sapphire substrates.

x	**0**	**0.18**	**0.37**	**0.54**	**0.59**	**0.74**	**1**
Al BEP (10^{-9} Torr)	0	2.5	4.9	9	9	9	15
Ga BEP (10^{-9} Torr)	11	9	9	9	4.7	3	0
Film thickness *d* (nm)	51.8	56.7	66	84.3	63.8	58.1	78.2
Growth rate (nm/min)	0.43	0.47	0.55	0.70	0.53	0.48	0.65

5.4 Growth of α-$(Al_xGa_{1-x})_2O_3$ on M-plane Sapphire Substrate

The α-$(Al_xGa_{1-x})_2O_3$ films were grown under the O-rich condition for the α-Ga_2O_3, as shown in Section 5.3: the sum of Al and Ga BEPs was set at lower than 2.0×10^{-8} Torr. Table 5.1 summarizes the growth condition, film thicknesses (*d*), and the growth rates of the samples. The film thicknesses and the growth rates were in the range of 51.8–84.3 nm and 0.43–0.70 nm/min, respectively.

5.4.1 Structural Properties of α-$(Al_xGa_{1-x})_2O_3$

X-Ray Diffraction Analysis

Symmetric XRD 2θ/ω scans of the samples are displayed with logarithmic intensity scale in Fig. 5.2. The profiles reveal the diffraction peak from α-$(Al_xGa_{1-x})_2O_3$ $30\bar{3}0$ at the angles slightly lower than that of the sapphire substrate without peaks originating from other phases and other planes. This indicates that single-phase α-$(Al_xGa_{1-x})_2O_3$ films are grown on m-plane sapphire substrates. With increasing *x*, the peaks from α-$(Al_xGa_{1-x})_2O_3$ $30\bar{3}0$ monotonically shift to higher angle without composition segregation, suggesting the higher Al composition in the films. From these results, single-phase α-$(Al_xGa_{1-x})_2O_3$ films are epitaxially stabilized successfully on m-plane sapphire substrates for the entire range of

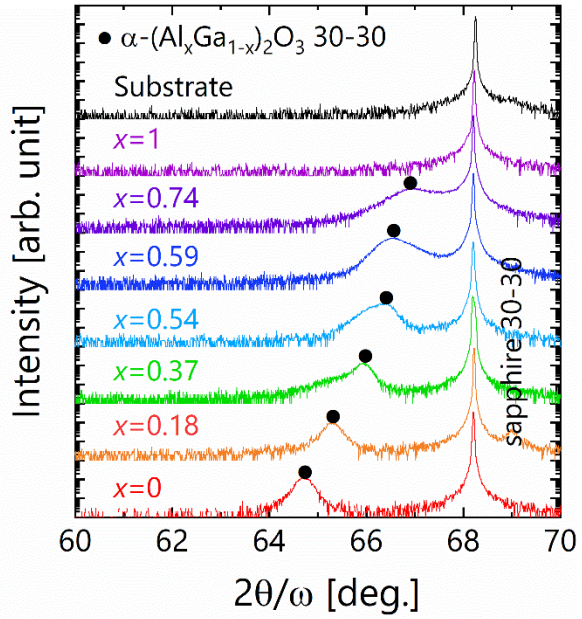

Figure 5.2. Symmetric XRD 2θ/ω scans of α-$(Al_xGa_{1-x})_2O_3$ films grown on m-plane sapphire substrates. Diffraction peaks from the α-$(Al_xGa_{1-x})_2O_3$ are denoted by ●. Note that no diffraction peaks from other phases are observed.

Al compositions. The α-Ga_2O_3 and α-Al_2O_3 films were able to be grown on m-plane sapphire substrates in the same growth temperature range (T_{sub} around 700 ºC), allowing the growth of the α-$(Al_xGa_{1-x})_2O_3$ alloys without phase or composition separation/segregation for the entire range of compositions.

To evaluate strains in the films, asymmetry reciprocal space maps (RSMs) for $22\bar{4}0$ reflections were taken. Figure 5.3(a) shows the positional relation between $(22\bar{4}0)$ and $(10\bar{1}0)$ (m-plane) of the corundum structure. $22\bar{4}0$ is decomposed into $30\bar{3}0+\bar{1}2\bar{1}0$, therefore the directions of Q_z and Q_x are along $10\bar{1}0$ (the growth direction) and $\bar{1}2\bar{1}0$ (one of a-axes), respectively. The dashed red line intersects the theoretical positions of sapphire [(Q_x, Q_z)=(−0.420, 0.728)] and α-Ga_2O_3 $22\bar{4}0$ reflection [(Q_x, Q_z)= (−0.401, 0.695)]. When x is smaller than 0.18, the α-$(Al_xGa_{1-x})_2O_3$ films are lattice-relaxed as shown in Fig. 5.3(b) and (c). On the other hand, two reflection peaks of α-$(Al_xGa_{1-x})_2O_3$ are obtained at x between 0.37 and 0.74: ones are on the same Q_x lines (Q_x=−0.42 Å^{-1}) as that of the sapphire substrate and others are located between the dashed line and Q_x=−0.42 Å^{-1} [Fig. 5.3 (d)-(g)]. These results indicate that the α-$(Al_xGa_{1-x})_2O_3$ films ($0.37 \leqq x_{BEP} \leqq 0.74$) consist of coherent and relaxed layers, and the relaxed layers are subject to slight in-plane compressive strain. The smaller lattice mismatches between α-$(Al_xGa_{1-x})_2O_3$ with lager x and sapphire probably enhanced the coherent growth.

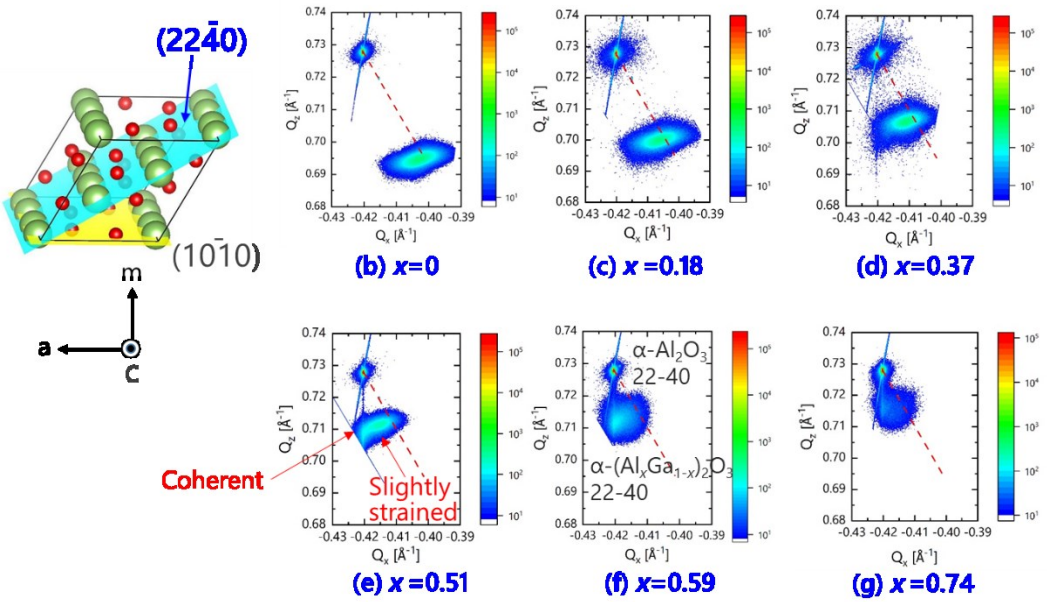

Figure 5.3. (a) Schematic of the crystal structure of α-$(Al_xGa_{1-x})_2O_3$ viewed along 0001 axis. Green and red balls show metal (gallium or aluminum) and oxygen atoms. (b)-(g) are XRD reciprocal space maps in the vicinity of $22\bar{4}0$ spots of the α-$(Al_xGa_{1-x})_2O_3$ films. The directions of Q_z and Q_x are along $10\bar{1}0$ and $\bar{1}2\bar{1}0$, respectively.

Atomic Force Microscopy Observation

Figures 5.4 depicts the surface AFM images of the α-$(Al_xGa_{1-x})_2O_3$ films. When x is smaller than 0.54, the root mean square (RMS) roughness is smaller than 1 nm. On the other hand, the α-$(Al_xGa_{1-x})_2O_3$ films whose x is larger than 0.51 have rough surface morphology due to probably the low substrate temperature for the growth of Al_2O_3. The smoother morphology of α-$(Al_xGa_{1-x})_2O_3$ with larger x is expected to be achieved by increasing the substrate temperature in future works.

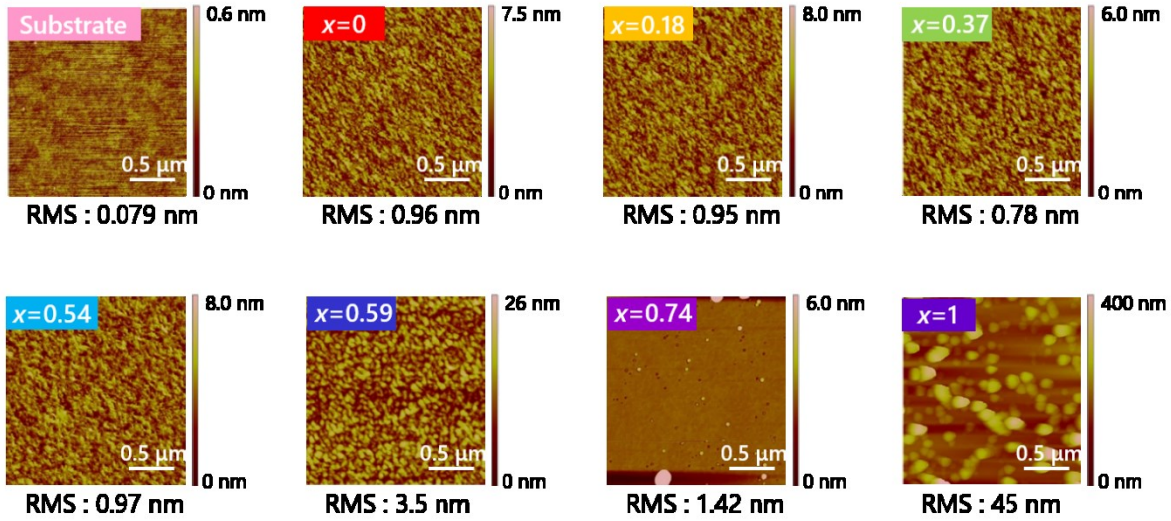

Figure 5.4. Surface AFM images of α-$(Al_xGa_{1-x})_2O_3$ films on m-plane sapphire substrates. The RSM roughness of the α-$(Al_xGa_{1-x})_2O_3$ films for $x < 0.51$ is less than 1 nm.

Scanning Transmission Electron Microscope Observations

In order to discuss the crystal structures of the samples in detail, cross-sectional STEM observations were conducted for α-Ga_2O_3 and α-$(Al_{0.37}Ga_{0.63})_2O_3$ films. The α-Ga_2O_3 sample was grown for an hour at the Ga BEP of 2.1×10^{-8} Torr, which is the intersection of the Ga rich region and the plateau region [Fig. 5.1]. The substrate was annealed in an atmospheric furnace at 1050 ºC for 6 hours, resulting in the slightly rough surface morphology. Figures 5.5(a) and 5.5(b) are low and medium-magnification images for the α-Ga_2O_3/sapphire substrate viewed along the $\langle 11\bar{2}0 \rangle$ zone axis so that a c-plane is going into the image. As shown in both Figs. 5.5(a) and 5.5(b), no c-plane facet was observed because the m-plane substrate prevented forming c-facets, leading to the growth of α-Ga_2O_3 by preventing the inclusion of the β-phase. The image of the α-Ga_2O_3/sapphire interface reveals that the α-Ga_2O_3 film was grown on the m-plane sapphire with the same atomic arrangement as the substrate [Fig. 5.5(c)].

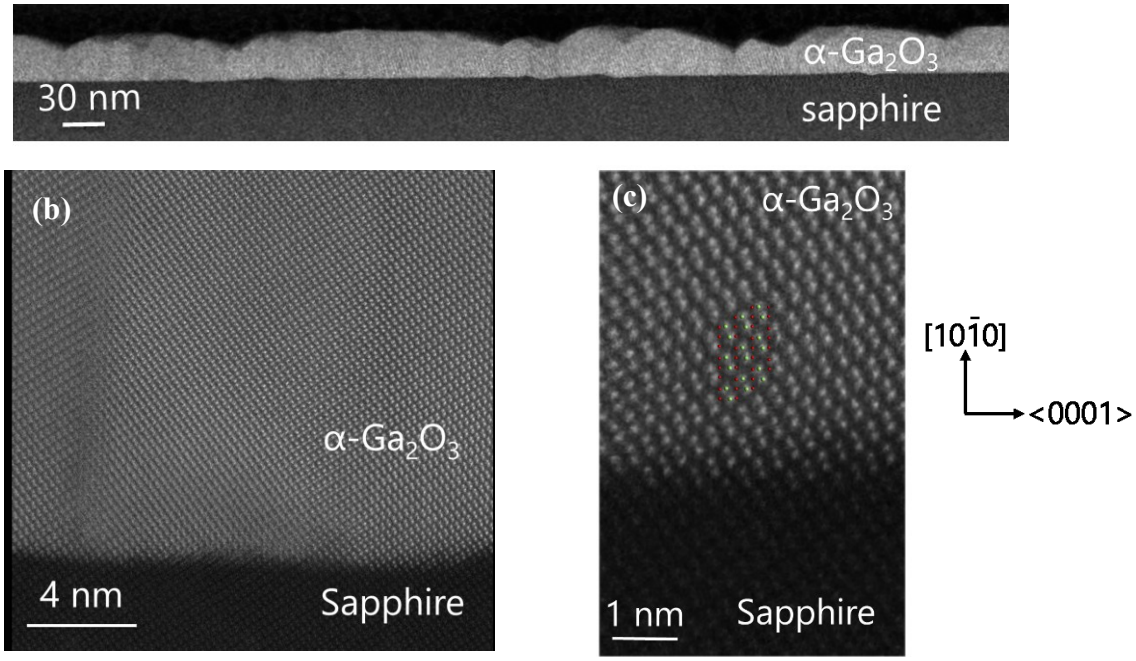

Figure 5.5 Cross-sectional STEM images of the α-Ga_2O_3 sample with the incident beam direction along the $\langle 11\bar{2}0 \rangle$ axis. (a) Low-, (b) medium- and (c) high-magnification images.

The sample was observed along the different zone axis of $\langle 0001 \rangle$. The relaxation of the film was clearly observed at the interface between the film and the substrate due to the large lattice mismatch to sapphire substrate (3.54 and 4.81% along c- and a-axes), as shown in Fig. 5.6(a). When α-Ga_2O_3 is viewed along $\langle 0001 \rangle$, gallium atoms (green balls) arrange in a hexagonal form [Figure 5.6(b)]. In Fig. 5.6(c), the arrangement of the gallium atoms is observed on the left side of the STEM image, while the different arrangement is detected on the right side. Figure 5.6(d) displays the enlarged image of the region including the different arrangement looking hexagonal chains. Here, the displacements are happening along the $\langle 11\bar{2}0 \rangle$ axis (horizontal direction), making the lattice structure overlapped and look the hexagonal structure. The displacement was occurred with different glide direction and distance as well, looking obscure crystal. This stacking fault seems to be caused by the strain from the interface due to the large lattice mismatches between the film and substrate. Although the dislocations and the stacking faults exist, different phases/domains were not detected from the STEM observation viewed along both the $\langle 11\bar{2}0 \rangle$ and $\langle 0001 \rangle$ axes. This indicates single-crystalline α-Ga_2O_3 was grown on the m-plane sapphire substrate.

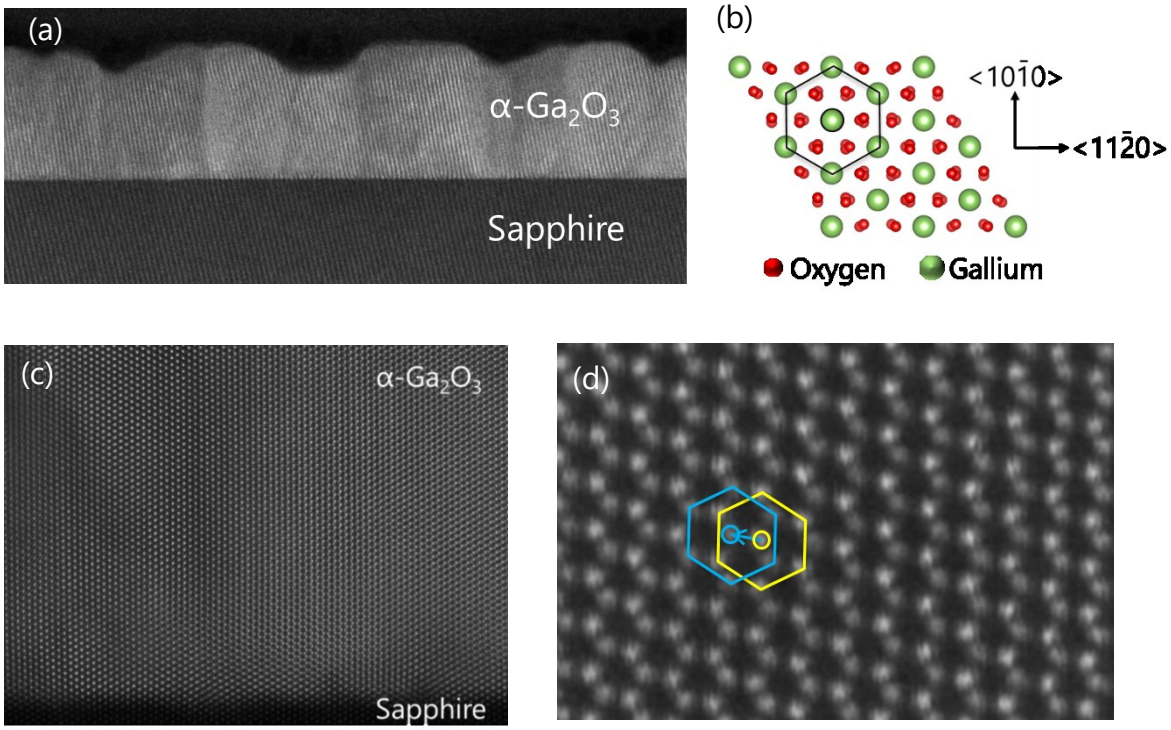

Figure 5.6. Cross sectional STEM images of the α-Ga_2O_3 viewed along the ⟨0001⟩ zone axis. (a) Low and (c) medium-magnification images. (d) is a high-magnification image of the region where the stacking faults were detected. (b) is the schematic of α-Ga_2O_3 viewed along ⟨0001⟩. The red and green balls show oxygen and gallium atoms.

Figure 5.7(a) is the low-magnification cross-sectional STEM image of the α-$(Al_{0.37}Ga_{0.63})_2O_3$ sample viewed along the ⟨0001⟩ axis. The film was uniformly grown on the m-plane sapphire substrate as the AFM image revealed [Fig. 5.4]. Although the color contrast was observed due to the strain from the substrate, neither a significant phase separation or a compositional segregation was not detected. The image closer to the α-$(Al_{0.37}Ga_{0.63})_2O_3$/sapphire interface is shown in Fig. 5.7(b). The α-$(Al_{0.37}Ga_{0.63})_2O_3$ film has the same crystal structure and orientation as the substrate as shown in Fig. 5.7(c). The film also has the staking fault which was seen in the α-Ga_2O_3 film, but the α-$(Al_{0.37}Ga_{0.63})_2O_3$ film is single crystalline.

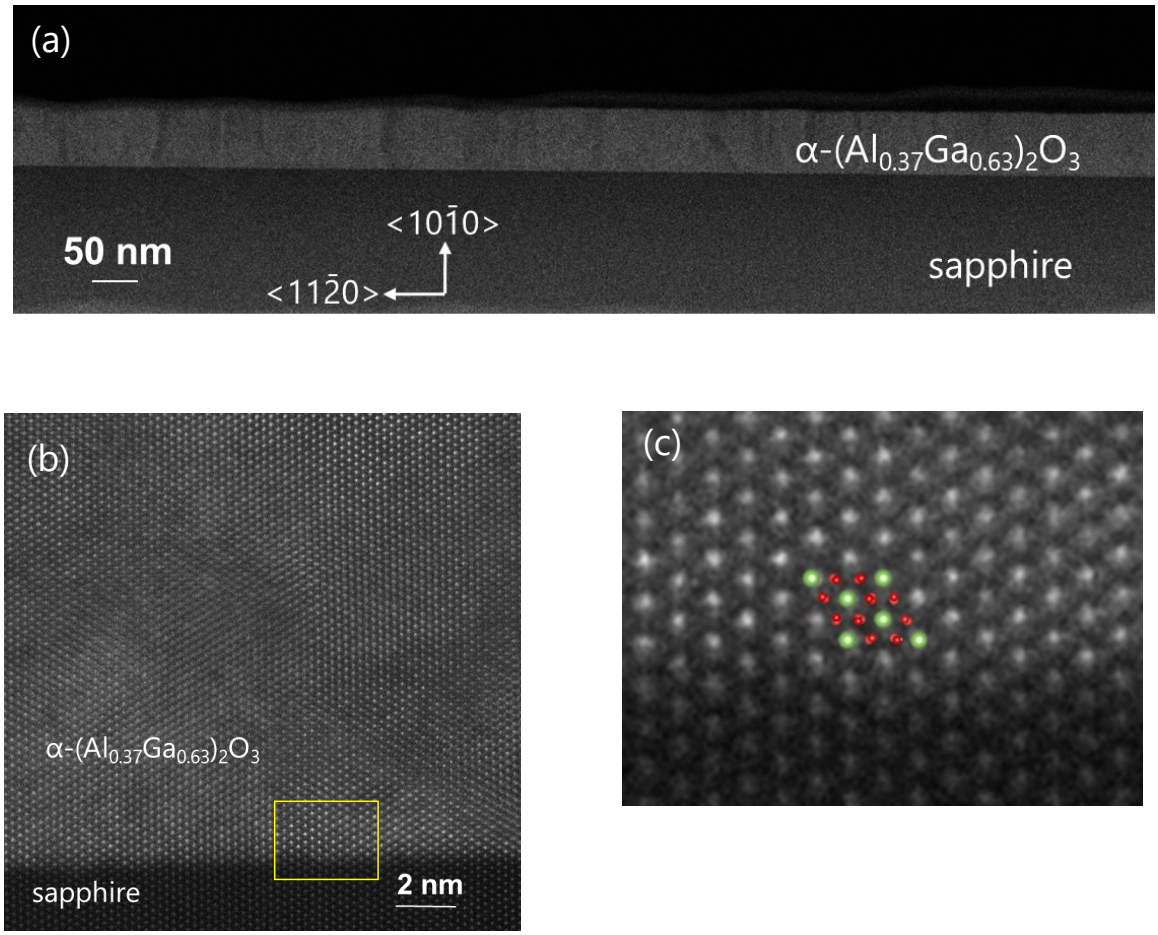

Figure 5.7. (a) low and (b) high-magnification cross-sectional STEM images of the α-$(Al_{0.37}Ga_{0.63})_2O_3$ on *m*-plane sapphire viewed along the <0001> zone axis. (c) is the enlarged image in the frame work shown in (b). Red and green balls represent oxygen and metal (gallium/aluminum) atoms.

5.4.2 Bandgap Energy of α-$(Al_xGa_{1-x})_2O_3$

Figure 5.8(a) shows the optical transmittance spectra of the α-$(Al_xGa_{1-x})_2O_3$ films (T) and a bare m-plane sapphire substrate (T_{sub}) as a function of the photon energy (hv). Each film shows as high transparency as the substrate in the visible and UV spectral ranges. Note the transmittance of α-$(Al_{0.37}Ga_{0.63})_2O_3$ is lower than the other samples since the size of the sample was smaller than that of the aperture used for the measurement. Each absorption coefficient (α) was calculated using the following equation: $T/T_{sub} = \exp(-\alpha d)$. By using the calculated α, $(\alpha hv)^2$ was plotted as a function of hv [Fig. 5.8(b)]. When x=0 and 0.18, the absorption edge exhibits a double steplike onset while the α-$(Al_xGa_{1-x})_2O_3$ films (x>0.37)

have a single step onset. The double steplike onset of the α-Ga_2O_3 thin film has been reported earlier, showing two allowed direct transitions (E_g=5.61 and 6.44 eV). [13] The Ga-rich α-$(Al_xGa_{1-x})_2O_3$ films ($0 \leq x \leq 0.37$) show the broader absorption onsets than the Al-rich samples, which is related to the slightly indirect character of α-Ga_2O_3. Direct bandgap energies of the α-$(Al_xGa_{1-x})_2O_3$ films were estimated from the relationship of $(\alpha hv)^2$ versus $(hv-E_g)$. As drawn by the red closed circles in Fig. 5.8(c), the experimental direct bandgaps monotonically increase with increasing x. The black solid line depicts the calculated direct and indirect bandgap energies reported by Peelaers *et al*. using hybrid density functional theory calculations. [14] The bandgaps of the α-$(Al_xGa_{1-x})_2O_3$ films are approximately 0.2 eV smaller than the theoretical values because the simple Tauc plots [$(\alpha hv)^2$ versus $(hv-E_g)$] are used to estimate the bandgap energies, resulting in the underestimation of the bandgap energies due to an exiton absorption with low energy tail that is related to the slightly indirect character of α-Ga_2O_3. In the Al-rich region, the lower crystalline quality of the films could be the reason as well. Bowing parameters b are obtained from the following equation:

$$E_g(x) = (1-x)E_g[Ga_2O_3] + xE_g[Al_2O_3] - bx(1-x),$$

where $E_g[Ga_2O_3]$ and $E_g[Al_2O_3]$ are the bandgap energies of α-Ga_2O_3 and α-Al_2O_3. By fitting the plot to the above equation, the value of b is estimated to be 1.21 eV. Here $E_g[Ga_2O_3]$= 5.34 eV and $E_g[Al_2O_3]$=8.59 eV were used. The experimental value agrees well with the theoretical value of 1.37 eV (direct).

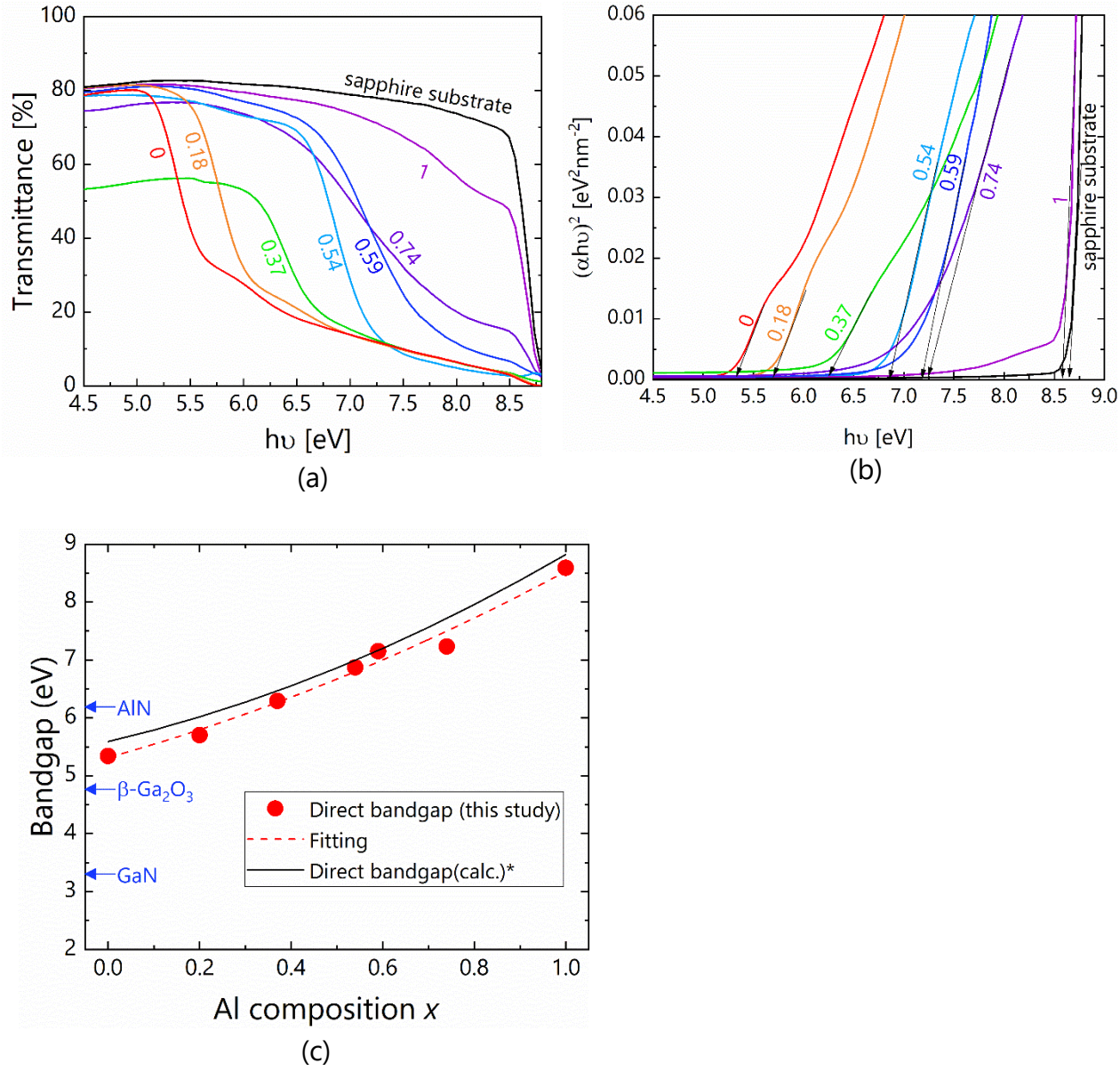

Figure 5.8. (a) External optical transmittance of the α-$(Al_xGa_{1-x})_2O_3$ films and substrate, (b) $(\alpha hv)^2$-hv plot as a function of the Al composition. The α-$(Al_{0.37}Ga_{0.63})_2O_3$ film exhibited a lower transmittance than the other samples since the sample was smaller than the aperture for the transmittance measurement. (c) Direct bandgaps for the α-$(Al_xGa_{1-x})_2O_3$ films as a function of the Al composition. The solid red line is a quadratic fit to the direct bandgaps. The black and purple solid (dashed) lines are quadratic fits to the computed direct (indirect) bandgaps for the corundum and monoclinic structures as reported [14].

5.5 Summary

This chapter demonstrated the epitaxial stabilization of the single-α-phase $(Al_xGa_{1-x})_2O_3$ films for the entire range of x on m-plane sapphire substrates without phase separation by PAMBE. The cross-sectional STEM observation revealed that the α-$(Al_xGa_{1-x})_2O_3$ films were single crystal by preventing the formation of c-plane facets, which is considered to contribute the formation of the β-phase in the MBE growth. However, the stacking faults were observed in the α-Ga_2O_3 and α-$(Al_{0.37}Ga_{0.63})_2O_3$ films due to the strain arisen from the lattice mismatch between the films and substrate. The bandgap energy was controlled from 5.34 to 8.59 eV with the bowing parameter of 1.21 eV. Although the promising result was achieved for the m-plane substrate, further studies are required to investigate the electric properties of the MBE grown $(Al_xGa_{1-x})_2O_3$ films on sapphire substrates with various orientations.

References

1) S.W. Kaun, F. Wu, and J.S. Speck, J. Vac. Sci. Technol. A Vacuum, Surfaces, Film. **33**, 041508 (2015).
2) E. Ahmadi, O.S. Koksaldi, X. Zheng, T. Mates, Y. Oshima, U.K. Mishra, and J.S. Speck, Appl. Phys. Express **10**, 071101 (2017).
3) S. Krishnamoorthy, Z. Xia, C. Joishi, Y. Zhang, J. McGlone, J. Johnson, M. Brenner, A.R. Arehart, J. Hwang, S. Lodha, and S. Rajan, Appl. Phys. Lett. **111**, 023502 (2017).
4) Y. Zhang, C. Joishi, Z. Xia, M. Brenner, S. Lodha, and S. Rajan, Appl. Phys. Lett. **112**, 233503 (2018).
5) T. Oshima, Y. Kato, M. Imura, Y. Nakayama, and M. Takeguchi, Appl. Phys. Express **11**, 065501 (2018).
6) R. Schewski, G. Wagner, M. Baldini, D. Gogova, Z. Galazka, T. Schulz, T. Remmele, T. Markurt, H. von Wenckstern, M. Grundmann, O. Bierwagen, P. Vogt, and M. Albrecht, Appl. Phys. Express **8**, 011101 (2015).
7) Z. Cheng, M. Hanke, P. Vogt, O. Bierwagen, and A. Trampert, Appl. Phys. Lett. **111**, 162104 (2017).
8) M. Kracht, A. Karg, M. Feneberg, J. Bläsing, J. Schörmann, R. Goldhahn, and M. Eickhoff, Phys. Rev. Appl. **10**, 024047 (2018).
9) R. Kumaran, T. Tiedje, S.E. Webster, S. Penson, and W. Li, Opt. Lett. **35**, 3793 (2010).
10) K. Akaiwa, K. Ota, T. Sekiyama, T. Abe, T. Shinohe, and K. Ichino, Phys. Status Solidi **1900632**, 1900632 (2020).

11) P. Vogt and O. Bierwagen, Appl. Phys. Lett. **108**, 072101 (2016).
12) M. Kracht, A. Karg, J. Schörmann, M. Weinhold, D. Zink, F. Michel, M. Rohnke, M. Schowalter, B. Gerken, A. Rosenauer, P.J. Klar, J. Janek, and M. Eickhoff, Phys. Rev. Appl. **8**, 054002 (2017).
13) A. Segura, L. Artús, R. Cuscó, R. Goldhahn, and M. Feneberg, Phys. Rev. Mater. **1**, 024604 (2017).
14) H. Peelaers, J.B. Varley, J.S. Speck, and C.G. Van de Walle, Appl. Phys. Lett. **112**, 242101 (2018).

Chapter 6

Phase Transition Temperature of α-Ga_2O_3 Films on Sapphire Substrates

6.1 Introduction

α-Ga_2O_3 has been reported to convert to the thermodynamically most stable β-phase upon heating at atmospheric pressure at 600-650 ºC owing to its metastable characteristic. [1,2] The α-Ga_2O_3 film grown on sapphire substrates by mist-CVD also has changed to the β-phase at temperatures higher than 600 ºC. [3,4] This is a severe limit for fabrication of α-Ga_2O_3 based device because the temperature of the film has to be set at lower than 600 ºC in some device processes. Especially, the doping technique for α-Ga_2O_3 by using ion-implantation has not been achieved yet due to the low phase transition temperature. The Si-ion implanted in β-Ga_2O_3 has been activated at 900-1000 ºC. [5] The similar activation annealing temperature is predicted to be required for the ion implantation in α-Ga_2O_3, but it is higher than the phase transition temperature of α-Ga_2O_3. However, against the phase transition temperature around 600 ºC, the growth of α-Ga_2O_3 films has been conducted at the growth temperature of 800 ºC, corresponding with the surface temperature of 700 ºC, as described in Chapter 2. The result indicates the possibility that α-Ga_2O_3 maintains the corundum structure at higher temperature than 650 ºC by some kind of techniques. This chapter investigates the phase transition temperature of α-Ga_2O_3 films grown on sapphire substrates by changing the Ga precursors, growth temperatures, and film thicknesses.

6.2 Experimental Procedures

α-Ga_2O_3 films were grown on c-plane sapphire substrates. Gallium tri-chloride ($GaCl_3$) or gallium(III) acetylacetonate [$Ga(acac)_3$] was dissolved in the mixed solution of H_2O and HCl. N_2 was used as both carrier and dilution gases. The growth temperature (T_g) was changed between 500 and 700 ºC. Selective area growths of α-Ga_2O_3 were carried out on c-plane sapphire substrates, where a dot-patterned SiO_2 mask with the diameter 5 μm was used as a mask material. The α-Ga_2O_3 films were annealed in an atmospheric furnace for 30 min at annealing temperatures (T_A) between 600 and 950 ºC. The phase transition

temperature was determined by symmetric X-ray diffraction (XRD) 2θ/ω measurements for the samples after annealing at T_A. Phase transition temperature was defined as the annealing temperature at which the β-phase became visible in XRD spectra. High-temperature XRD of a Rigaku SmartLab system was also used to assess lattice lengths of the α-Ga_2O_3 films and sapphire substrates. The measurement was carried out under air atmosphere and the temperature in a black synthetic quartz glass, where the sample was put on, was monitored.

6.3 Dependence on Ga Precursors

α-Ga_2O_3 films were grown on c-plane sapphire substrates at T_g=500 ºC using $Ga(acac)_3$ and $GaCl_3$ as Ga precursors. As described in Chapter 2, $Ga(acac)_3$ causes the high carbon impurity concentration in α-Ga_2O_3 films (1×10^{19} cm^{-3}), while $GaCl_3$ reduced the carbon impurity in the films to lower than 1×10^{17} cm^{-3}. The films thicknesses of the samples were 130 nm for the $Ga(acac)_3$ and 150 nm for the $GaCl_3$ precursor. Figure 6.1(a) and 6.1(b) are symmetric XRD 2θ/ω scan profiles of the sample grown using the $Ga(acac)_3$ and $GaCl_3$ precursors. Both α-Ga_2O_3 samples show α-Ga_2O_3 0006 reflex for T_A≤650 ºC, while β-Ga_2O_3 $\bar{4}02$ for T_A=700 ºC. This result reveals that the samples grown using both precursors convert to the β-phase after annealing at 700 ºC and the phase transition temperature does not depend on the Ga precursors (the impurity concentrations), when the

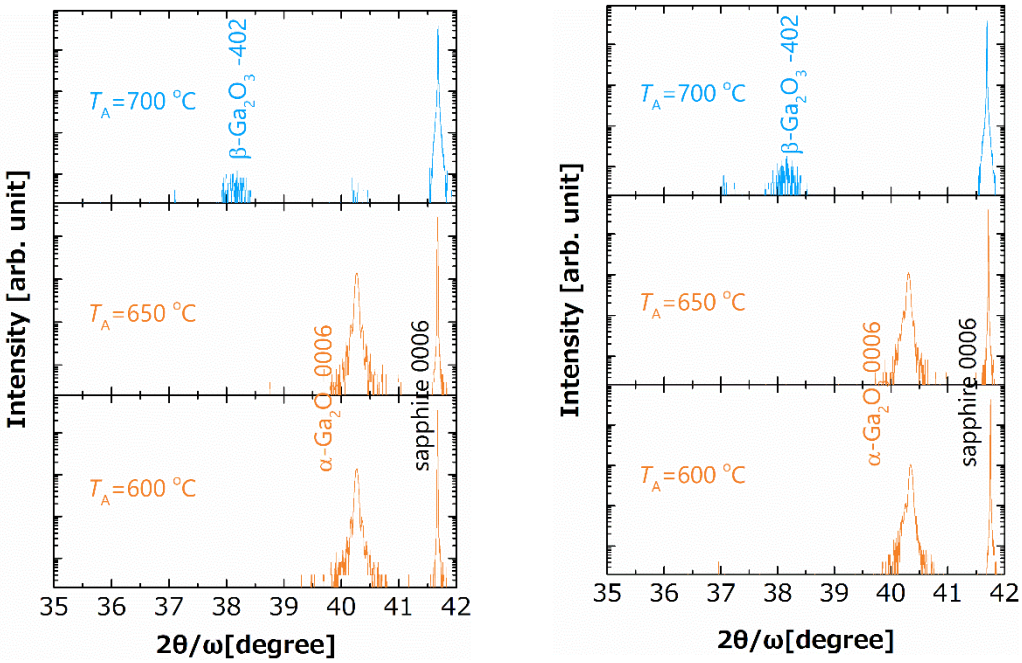

Figure 6.1. XRD 2θ/ω scans of the Ga_2O_3 films with the film thickness of 130-150 nm on c-plane sapphire substrates after annealing at 600, 650 and 700 ºC. (a) $Ga(acac)_3$ and (b) $GaCl_3$ were used as a Ga precursor.

films have the same film thickness.

6.4 Dependence on Thicknesses of α-Ga_2O_3 Films

α-Ga_2O_3 films were grown on c-plane sapphire substrates by changing film thicknesses and growth temperatures. Then they were exposed to thermal annealing, as described in Section 6.2.

The phase transition temperature is summarized in Fig. 6.2. Open and solid symbols show samples that maintained the α-phase and completely converted to β-Ga_2O_3 from XRD 2θ/ω scan profiles. The phase transition temperature and film thickness have a strong correlation regardless of the growth temperature and the Ga precursor (impurity concentrations in the films). When thicker than 1 μm, the α-Ga_2O_3 film was converted to the β-phase at T_A= 600 ºC as reported by Lee *et. al.* [3] On the other hand, as the film thickness becomes smaller, the α-Ga_2O_3 films maintain the corundum structure at higher temperature. When the film thickness is as small as 20 nm, the α-Ga_2O_3 film maintained the corundum structure at T_A=750 ºC, which is 150 ºC higher than that of the film with the thickness of several hundred nm. The dependence on the film thickness allowed the growth of α-Ga_2O_3 films with thinner thicknesses than 100 nm at growth temperatures higher than 600 ºC [Chapter 2], that is the phase transition temperature reported in the previous study. In addition, the selective area grown (SAG) α-Ga_2O_3 on c-plane sapphire maintains the

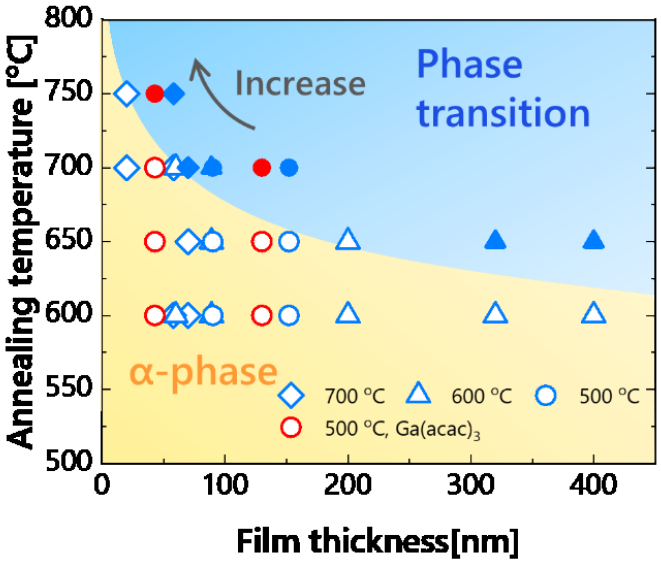

Figure 6.2. Open and solid symbols show samples that maintained α-phase and completely converted to the β-phase at an annealing temperature as a function of the film thickness. Samples drawn in blue and red colors were grown using $Ga(acac)_3$ and $GaCl_3$ as a Ga precursor. The circular, triangular and rhomboid symbols show the growth temperature of 500, 600 and 700 ºC, respectively.

corundum structure at T_A=750 °C when the thickness is around 400 nm. The enhancement of the thermal stability led to the SAG α-Ga_2O_3 with the thickness of the micrometer order at T_g=600 and 700 °C, as reported in Chapter 4.

6.5 Transmission Electron Microscope Observation

Transmission electron microscope (TEM) observation was conducted to discuss how the α-Ga_2O_3 films convert to the β-phase by annealing.

In order to obtain more detailed phase transition temperatures of α-Ga_2O_3 films, T_A for α-Ga_2O_3 films was changed from 650 to 700 ºC at an interval of 5-25 ºC. The samples were grown at T_g =700 ºC using the $GaCl_3$ precursor and the films thickness was around 100-200 nm. Symmetric XRD 2θ/ω scan profiles reveals that the sample maintains the corundum structure at T_A =660 ºC, while a weak diffraction peak originated form β-Ga_2O_3 $\bar{4}02$ appears at T_A =670 ºC, as shown in Fig. 6.3. The α-Ga_2O_3 film completely converts to β-Ga_2O_3 at T_A =700 ºC. TEM images were obtained for the samples annealed at T_A= 660 and 670 ºC in order to observe the initial behavior of the conversion to the β-phase.

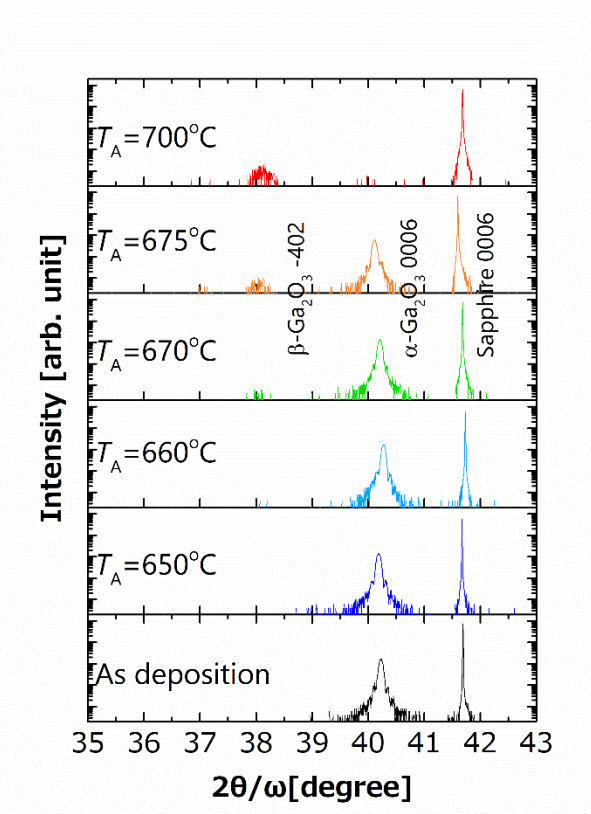

Figure 6.3. Symmetric XRD 2θ/ω scans of the Ga_2O_3 film with the film thickness of ca. 100 nm on c-plane sapphire substrates before and after annealing at 650, 660, 670, 675 and 700°C.

***T_A*=660 ºC**

Figure 6.4(a) is a cross-sectional TEM image of the α-Ga_2O_3 film annealed at T_A =660 ºC viewed along the ⟨10$\bar{1}$0⟩ axis. At this T_A, the sample maintained the corundum structure judging from the XRD measurement [Fig. 6.3]. The TEM image reveals that the film homogeneously remains on the substrate and different phases or domains do not appear although the strain contrast, which arises from the lattice mismatches between the film and the substrate, is observed. Transmission electron beam diffraction spots were obtained for the sapphire substrate, the α-Ga_2O_3/sapphire interface, the middle region of the α-Ga_2O_3

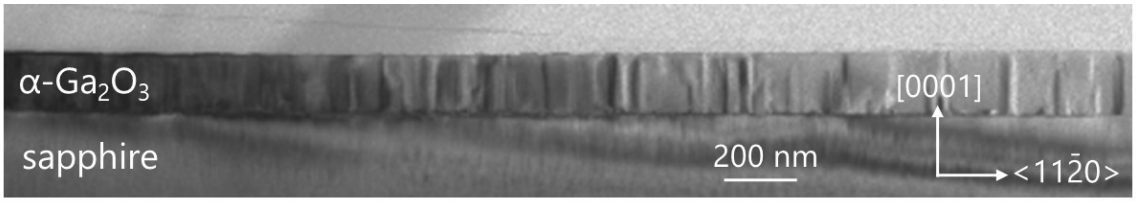

(a) ⟨10$\bar{1}$0⟩ zone axis

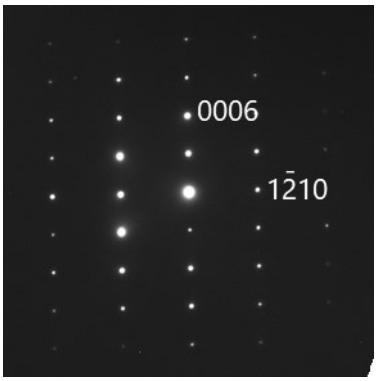

(b) Sapphire substrate

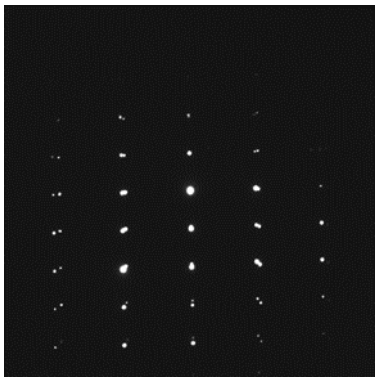

(c) α-Ga_2O_3/sapphire interface

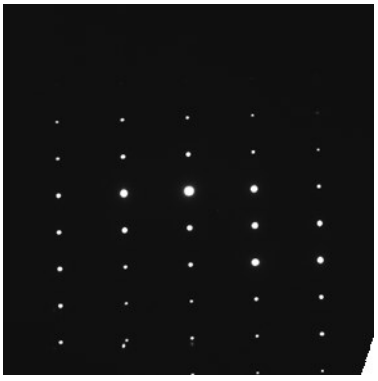

(d) Middle part of α-Ga_2O_3 film

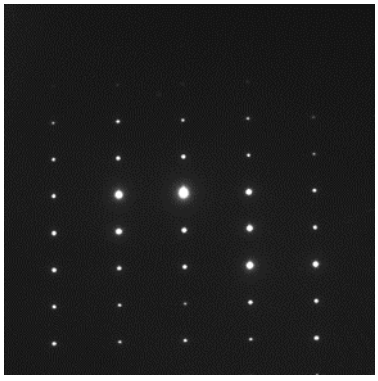

(e) Surface of α-Ga_2O_3 film

Figure 6.4. (a) A cross-sectional TEM image of the α-Ga_2O_3 film on sapphire substrate with the film thickness of ca. 200 nm after annealing at 660℃ viewed along the ⟨10$\bar{1}$0⟩ axis. Transmission electron beam diffraction spots for the (a) sapphire, (b) α-Ga_2O_3/sapphire interface, (c) middle part of the α-Ga_2O_3 film and (d) vicinity of surface of the α-Ga_2O_3 film.

film, and the vicinity of the surface of the film [Figs. 6.4(b)-(e)]. All the diffraction patterns are from the corundum structure viewed along the ⟨$10\bar{1}0$⟩ axis, indicating the film maintains the α-phase after annealing at 660 ºC, as the XRD 2θ/ω profile revealed [Fig. 6.3].

T_A=670 ºC

Figure 6.5(a) is an overview of cross-sectional TEM image of the α-Ga_2O_3 film annealed at T_A=670 ºC viewed along the ⟨$11\bar{2}0$⟩ axis. This is the sample partially converted to β-Ga_2O_3 from the XRD 2θ/ω scan [Fig. 6.3]. The film thickness in the TEM is thinner on the right side of the image due to the sample preparation process for the TEM observation. Unlike the TEM image for T_A=660 ºC [Fig. 6.4(a)], brighter regions are observed in the TEM image of the film, which could arise from different phases/domains. Figure 6.5(b) is a dark filed image in the red framework drawn in Fig. 6.5(a). The color contrasts invert that of the bright filed image, and different phases/domains look black.

Figure 6.6(a) and 6.6(b) are the high magnification (a) bright-filed and (b) dark-filed TEM images, respectively, in the yellow framework ① drawn in Fig. 6.5(b). These images reveals that the semielliptic different phase/domain is introduced from the surface. Diffraction patterns for the sapphire substrate, film in the vicinity of the interface, and in the semielliptic region were taken to discuss the crystal structures of each region. The diffraction pattern for the film at the interface has the same pattern for the substrate [Figs. 6.4 (a) and 6.4(b)], resulting in the α-phase, while the patterns for the semielliptic regions arise from β-Ga_2O_3. The epitaxial relationships are β-Ga_2O_3 [$\bar{2}01$] ‖ α-Ga_2O_3 (0001) and β-Ga_2O_3 [010] ‖ α-Ga_2O_3 [$10\bar{1}0$]. β-Ga_2O_3 grown on c-plane sapphire also has been reported to have the same epitaxial relationship: β-Ga_2O_3 [$\bar{2}01$] ‖ sapphire (0001).

The same observations were conducted for the views ② and ③ shown in Fig. 6.5(b).

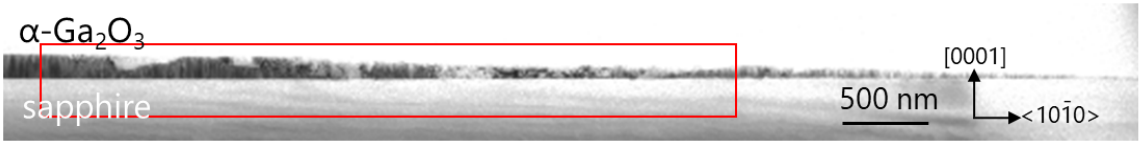

(a)

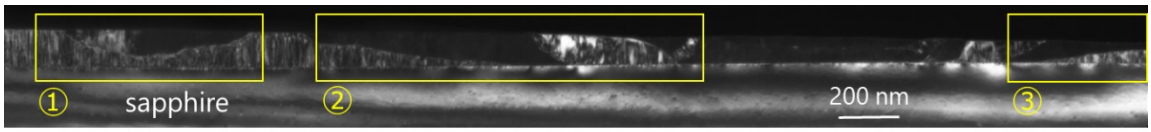

(b)

Figure 6.5. (a) A cross-sectional bright field TEM image of the α-Ga_2O_3 film on sapphire substrate after annealing at 670°C viewed along the ⟨$11\bar{2}0$⟩ axis. (b) A dark-filed image in the red framework shown in (a).

The black regions in the dark field images are found to be the β-phase, while the α-phase remains in the whitish areas for the both views [Figs. 6.7(b) and 6.7(e)]. On the other hand, the bright filed image for the view ② shows the unclear boundary between the α- and β-phase as a yellow framework depicts in Fig. 6.7(a). The high magnitude TEM image in

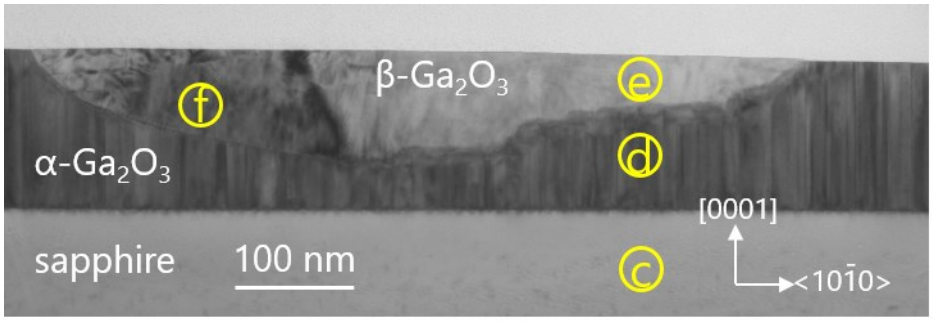

(a) Bright field

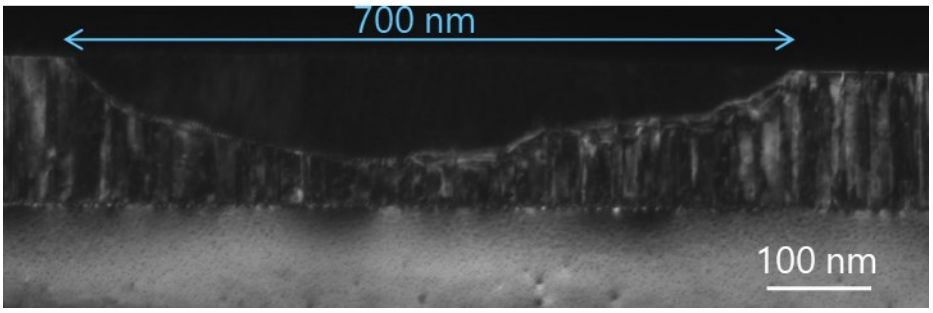

(b) Dark field

(c)

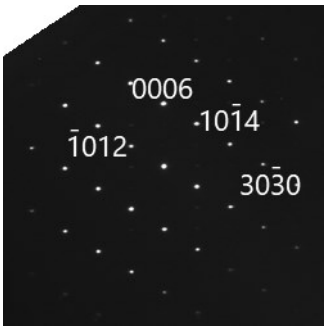

(d)

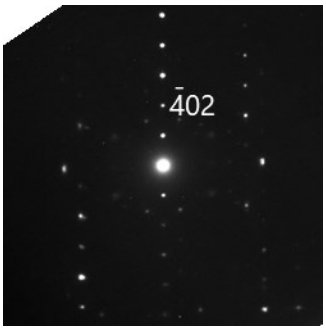

(e)

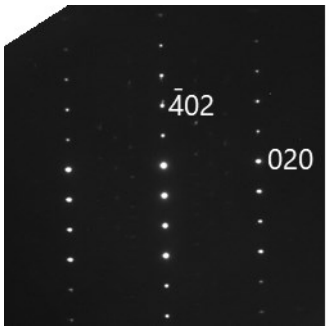

(f)

Figure 6.6. Cross-sectional TEM images in the yellow framework ① shown in Fig. 6.5(b). (a) bright field and (b) dark-filed images. (c)-(f) are diffraction spots for the area shown in (a).

the yellow framework reveals that the α- and β-Ga_2O_3 are overlapping at the boundary, resulting in the obscure interface in the bright-filed image [Fig. 6.7(c)]. The β-Ga_2O_3 observed in the views ② and ③ have the same orientation relationships as those for the view ①, but they have the different shapes of the trapezoidal cross-section spread from the surface of the films toward the substrate.

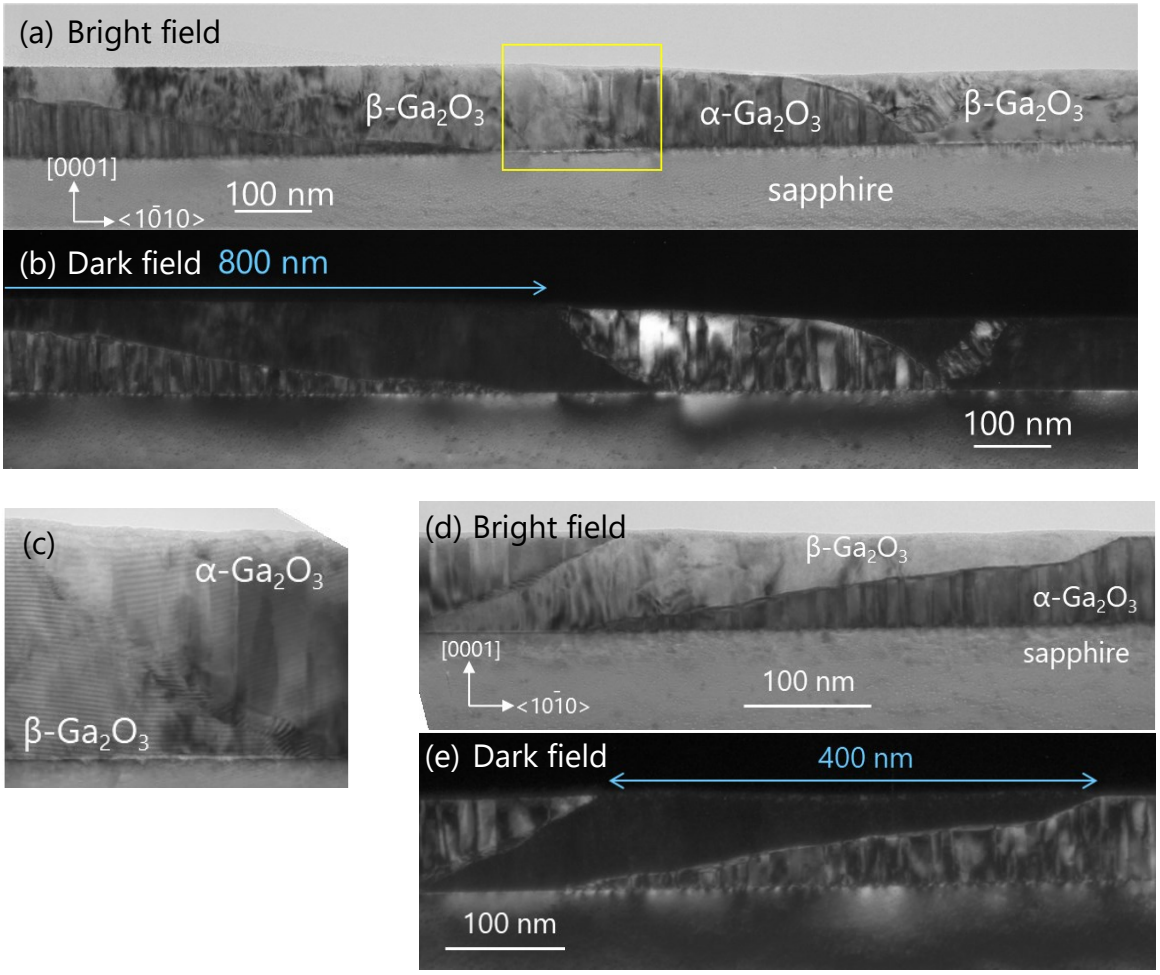

Figure 6.7. Cross-sectional TEM images in the yellow frameworks shown in Fig. 6.5(b). (a) bright field and (b) dark-filed images for the framework ②, and (d) bright field and (e) dark-filed images for the framework ③. (c) is the high magnification bright field image of the yellow framework shown in (a).

From these results, the α-Ga_2O_3 film grown on sapphire appear to convert to β-Ga_2O_3 from the surface of the film. α-Ga_2O_3 has a larger thermal expansion coefficient than sapphire and the difference of the coefficients becomes larger at higher temperature, [6,7] suggesting that α-Ga_2O_3 films on sapphire has larger compressive stress at the interface and tensile stress near the surface at higher temperature. β-Ga_2O_3 has the larger density than α-Ga_2O_3, therefore the tensile stress could convert α-Ga_2O_3 to β-Ga_2O_3 or the compressive stress help α-Ga_2O_3 maintain its phase. The smaller crystal size of the SAG α-Ga_2O_3 contributes to relaxing the tensile stress or maintaining the compressive stress in the α-Ga_2O_3, leading to the higher thermal stability.

6.6 High-Temperature XRD Analysis for α-Ga_2O_3 Film on C-Plane Sapphire Substrate

In order to evaluate strains in the α-Ga_2O_3 films at high temperature, the lattice lengths of the α-Ga_2O_3 films and sapphire substrates were assessed by using high-temperature XRD of a Rigaku SmartLab system. The α-Ga_2O_3 films were grown at T_g=700 ºC on c-plane sapphire substrates with/without the SiO_2 dot-patterned mask in the same growth condition. The film thickness of the sample grown on the unpatterned substrate was ca. 100 nm and the film converted to the β-phase by annealing at T_A=670 ºC in the air furnace described in Section 6.5. On the other hand, the sample started to convert to β-Ga_2O_3 at 640 ºC in the high-temperature XRD system. The temperature difference probably arises from using the different annealing systems. The SAG α-Ga_2O_3 layer on the patterned substrate showed a small diffraction peak from β-Ga_2O_3 at 680 ºC.

As references, the XRD measurements were conducted for a c-plane sapphire substrate without any growth as well. The measured lattice parameter (*c*) of the c-plane sapphire substrate agrees well with that reported by Yim, and the growth of the α-Ga_2O_3 films on the sapphire does not change the lattice parameter of the substrates, indicating that the sapphire substrate is not strained by the growth of the α-Ga_2O_3 film, as shown in Fig. 6.8(a).

Figure 6.8(b) shows the lattice parameter (*c*) of the α-Ga_2O_3 on patterned/unpatterned sapphire substrates. The α-Ga_2O_3 film grown on the unpatterned substrate has a slightly larger lattice length than the reported value, suggesting the in-plane compressive strain in the α-Ga_2O_3 film. As explained in Chapter 2, the film grown at growth temperatures higher than 600 ºC with the thickness of ca. 100 nm is not completely relaxed and subject to the compressive strain at the room temperature of 25 ºC after the growth. The difference between the lattice parameter of the α-Ga_2O_3 film and the reported value becomes smaller as the annealing temperature increases. After the conversion to β-Ga_2O_3 begins (640 ºC), the lattice length of the film saturates and the difference reaches almost zero. On the other hand, the lattice length of the SAG α-Ga_2O_3 layer agrees with the reported value, indicating

the α-Ga_2O_3 layer is completely relaxed. This is because the thickness of the SAG α-Ga_2O_3 is several times as large as that of the film on the unpatterned substrate due to the incorporation of the source materials supplied on the mask into the α-Ga_2O_3 facet on the

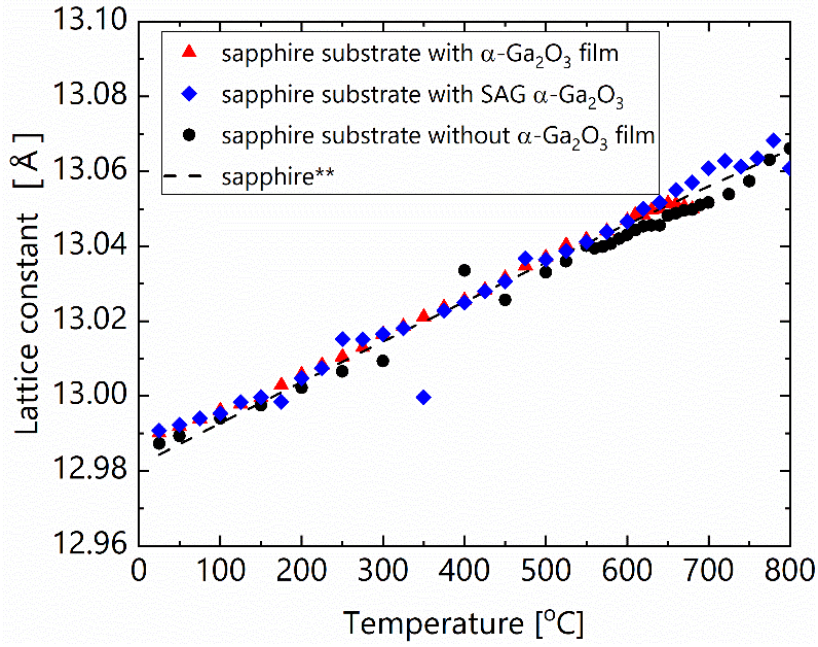

(a) sapphire

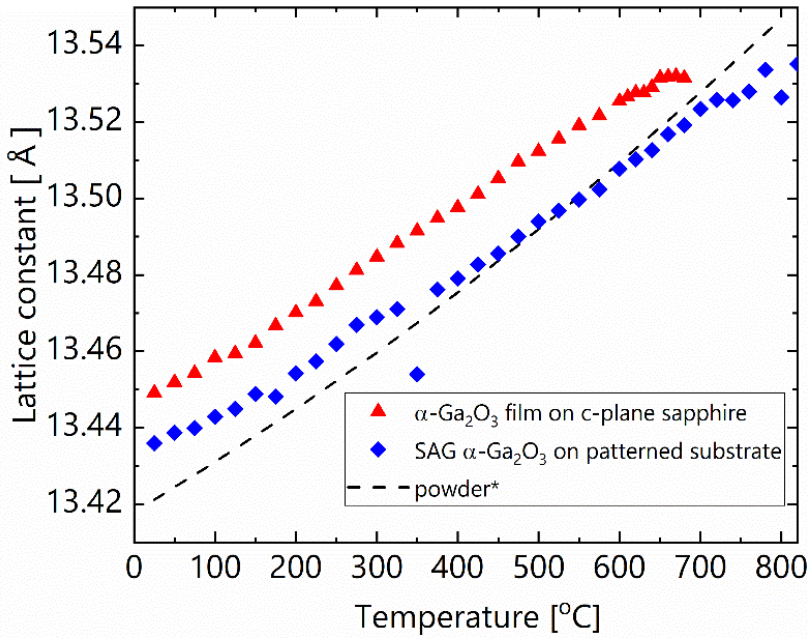

(b) α-Ga_2O_3

Figure 6.8. The c lattice parameter of (a) sapphire and (b) α-Ga_2O_3. The blue diamond and red triangle show the parameters of the SAG α-Ga_2O_3 and α-Ga_2O_3 film on c-plane sapphire substrates. The solid black symbol is a c-plane sapphire as recieved. The black dashed line shows the reported values in the previous studies.

window area. The detail was described in Chapter 4.

From all the results, the remain compressive strain does not contribute the phase transition temperature of α-Ga_2O_3 and the phase transition seems to arise from the tensile stress caused by the difference of the thermal expansion coefficients between α-Ga_2O_3 and sapphire. With increasing the annealing temperature, the tensile stress is applied to the vicinity of surface, as shown in Fig.6.9. β-Ga_2O_3 has the larger density than α-Ga_2O_3, therefore the tensile stress could convert α-Ga_2O_3 to β-Ga_2O_3 from the surface. The thicker film has the larger strain, resulting in the phase transition at lower annealing temperature. Using the patterned substrate can prevent α-Ga_2O_3 films from the tensile strain, leading to the higher phase transition temperature. It is also possible that the phase transition to the β-phase arise from an inhomogeneous strain in α-Ga_2O_3.

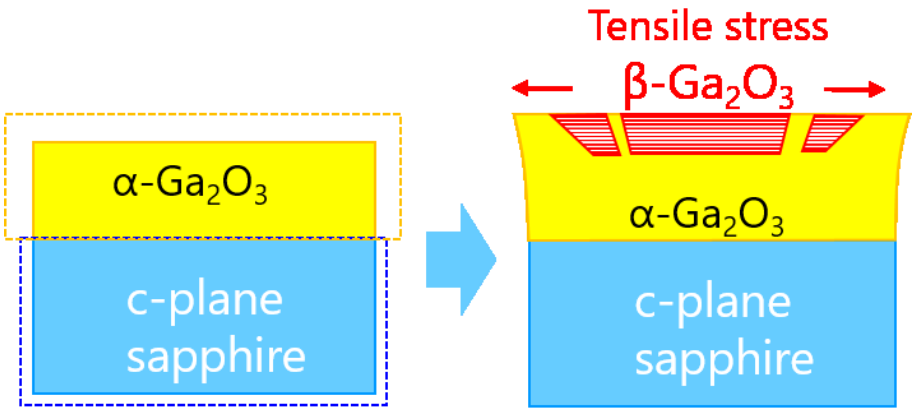

Figure 6.9. Schematics of relationship between a α-Ga_2O_3 film and a sapphire substrate at (a) room temperature and (b) phase transition temperature.

6.7 Summary

In this chapter, the phase transition temperature of α-Ga_2O_3 films on c-plane sapphire substrates was investigated. The phase transition temperature of the α-Ga_2O_3 films increased as the film thickness decreased regardless of the growth conditions. The TEM observations revealed that the phase transition to the β-phase occurred from the surface of the film. α-Ga_2O_3 has a larger thermal expansion coefficient than sapphire, resulting in the tensile one near the surface. β-Ga_2O_3 has the larger density than α-Ga_2O_3, therefore the tensile stress contributes to convert α-Ga_2O_3 to β-Ga_2O_3. From these results, α-Ga_2O_3 is expected to maintain corundum structure at higher than 750 ºC by removing the stress in α-Ga_2O_3 such as the fabrication of α-Ga_2O_3 bulk grown by using the ELO technique.

References

1) R. Roy, V.G. Hill, and E.F. Osborn, J. Am. Chem. Soc. **74**, 719 (1952).
2) H.Y. Playford, A.C. Hannon, E.R. Barney, and R.I. Walton, Chem. - A Eur. J. **19**, 2803 (2013).
3) S.-D. Lee, K. Akaiwa, and S. Fujita, Phys. Status Solidi **10**, 1592 (2013).
4) S.-D. Lee, Y. Ito, K. Kaneko, and S. Fujita, Jpn. J. Appl. Phys. **54**, 030301 (2015).
5) K. Sasaki, M. Higashiwaki, A. Kuramata, T. Masui, and S. Yamakoshi, Appl. Phys. Express **6**, 086502 (2013).
6) L.J. Eckert and R.C. Bradt, J. Am. Ceram. Soc. **56**, 229 (1973).
7) W.M. Yim and R.J. Paff, J. Appl. Phys. **45**, 1456 (1974).
8) Y. Oshima, K. Kawara, T. Shinohe, T. Hitora, M. Kasu, and S. Fujita, APL Mater. **7**, 022503 (2019).

Chapter 7

Conclusion

7.1 Conclusions

In this thesis, the growth of high quality corundum gallium oxide (α-Ga_2O_3) on sapphire substrates has been investigated toward high-performance α-Ga_2O_3 based power devices. Here, "high quality" α-Ga_2O_3 includes the excellent control of polymorphic of Ga_2O_3, impurity concentrations, and dislocation densities, composition of Ga_2O_3 based alloys, and the thermal stability of α-Ga_2O_3.

In Chapter 2, the mist-chemical vapor deposition (mist-CVD) growth of α-Ga_2O_3 was conducted using a carbon-free gallium tri-chloride ($GaCl_3$) as a gallium (Ga) precursor in order to eliminate the residual high carbon (C) impurity concentration of 1×10^{19} cm^{-3} in α-Ga_2O_3 films even grown using gallium(III) acetylacetonate [$Ga(acac)_3$] precursor. The concentrations of the C and chloride (Cl) impurities were decreased to below the detection limits (1×10^{17} cm^{-3} for C and 1×10^{17} cm^{-3} for Cl) by optimizing the growth condition. In addition, the author revealed that α-Ga_2O_3 is able to be grown at the growth temperature up to 800 ºC, while the low temperature around 500 ºC has been preferably used for the growth from the $Ga(acac)_3$ precursor. Atomic force microscopy (AFM) images showed that the high growth temperature allowed the smooth surface morphology of the α-Ga_2O_3 film with the root-square-mean (RMS) roughness of 0.19 nm. The growth reaction can be explained by that of halide vapor phase epitaxy using H_2O as an O precursor, resulting in the high growth rate of ~7.8 μm/h.

In Chapter 3, the polymorphic of Ga_2O_3 grown on α-$(Al_xGa_{1-x})_2O_3$ was studied toward devices with a multilayer structure. When the α-$(Al_xGa_{1-x})_2O_3$ layers were annealed and the AFM images showed atomic steps, ε-Ga_2O_3 was grown on the layer at 500 ºC regardless of the Al composition x. On the other hand, α-Ga_2O_3 was obtained on the as grown α-$(Al_xGa_{1-x})_2O_3$ layer at the same temperature. These results indicate that the surface morphology or termination change the formation energy of each phase. When the growth temperature was higher than 700 ºC, α-Ga_2O_3 was grown on the both annealed and as-grown α-$(Al_xGa_{1-x})_2O_3$ layer due to the longer diffusion length.

In Chapter 4, two approaches to the reduction of the dislocation density in α-Ga_2O_3 were proposed. First, a quasi-graded α-$(Al_xGa_{1-x})_2O_3$ buffer layer was introduced between a α-Ga_2O_3 film and a sapphire substrate using the mist-CVD method. The author devised

the compositionally quasi-graded buffer layer to enhance the controllability of changing the Al composition and to prevent the dislocation from propagating upward. With the buffer layer, the dislocations were concentrated in the buffer layers and the edge dislocation density was decreased nearly by two orders in magnitude. Secondly, the epitaxial lateral overgrowth of α-Ga_2O_3 was investigated. By using SiO_2 as a mask material, α-Ga_2O_3 was selectively grown on the patterned substrate when the growth temperature was higher than 550 ºC due to the longer diffusion length of source materials on the mask region. The epitaxial lateral overgrown (ELO) α-Ga_2O_3 on a-plane sapphire substrates with the stripes along m-axis showed the largest ratio of lateral and vertical growth rates (L/V ratio) of 0.96, resulting in the full coalescence. The generation of dislocations on the mask region was prevented, leading to the reduction the threading dislocation density on the center of the mask area to less than 1.6×10^7 cm^{-2}.

In Chapter 5, the growth of α-$(Al_xGa_{1-x})_2O_3$ films on sapphire substrates by plasma-assisted molecular beam epitaxy (PAMBE) was described toward α-$(Al_xGa_{1-x})_2O_3$ based heterostructure devices. By using m-plane sapphire substrates, which is perpendicular to c-plane, single-phase α-$(Al_xGa_{1-x})_2O_3$ films were stabilized in the entire range of x by preventing the formation of c-plane facets, which is considered to cause the growth of β-Ga_2O_3. The different phases/domains were not detected from both x-ray diffraction (XRD) measurement and cross-sectional scanning transmission electron microscopy (STEM) observations. However, the α-Ga_2O_3 and Ga-rich α-$(Al_xGa_{1-x})_2O_3$ films had stacking faults due to the strain from the substrates having the large lattice mismatched to the films. The bandgap energy of the α-$(Al_xGa_{1-x})_2O_3$ films was in the wide range from 5.34 to 8.56 eV.

In Chapter 6, the phase transition of α-Ga_2O_3 on sapphire to the β-phase was investigated. The phase transition temperature of α-Ga_2O_3 films increased as the film thickness decreased regardless of the growth conditions. Transmission electron microscopy (TEM) observations revealed that the phase transition to the β-phase occurred from the surface of the film. α-Ga_2O_3 has a larger thermal expansion coefficient than sapphire, suggesting that α-Ga_2O_3 films on sapphire substrates have the tensile stress near the surface. β- Ga_2O_3 has the larger density than α- Ga_2O_3, therefore the tensile stress could convert α-Ga_2O_3 to β-Ga_2O_3.

7.2 Future Works

The author studied high quality α-Ga_2O_3 on sapphire substrates in this thesis. However, there remain several issues to be solved, and there have emerged several goals to be accomplished in the future.

- **Relationship between electric property and dislocations in α-Ga_2O_3**

In this thesis, the reduction of the dislocation density in α-Ga_2O_3 has been reported by utilizing the α-$(Al_xGa_{1-x})_2O_3$ buffer layers and the epitaxial lateral overgrowth technique. Further studies on these approaches will lead to much less dislocation density in α-Ga_2O_3, but it is difficult to eliminate all the dislocations in α-Ga_2O_3 by heteroepitaxial growth. This study revealed some types of dislocations in α-Ga_2O_3 such as screw and edge dislocations, which can be controlled by selecting substrate orientations or designing the buffer layers. In order to achieve better device performance, it is necessary to identify the type of dislocations which causes fatal problems against electric properties and decrease the dislocation.

- **Electric property of n-type α-$(Al_xGa_{1-x})_2O_3$:** Though the growth of single-phase α-$(Al_xGa_{1-x})_2O_3$ and its bandgap engineering has been achieved by mist-CVD in the previous study and PAMBE in this study, its electric characteristic has not been studied yet. Especially n-type α-$(Al_xGa_{1-x})_2O_3$ is essential for the α-Ga_2O_3 based heterostructured devices. Mist-CVD is promising for the growth of α-$(Al_xGa_{1-x})_2O_3$, but the aqueous solution of precursors makes it difficult to control doping for alloy. Therefore, the fundamental study on the n-type control for α-$(Al_xGa_{1-x})_2O_3$ is required using MBE. Another possibility for achieving n-type α-$(Al_xGa_{1-x})_2O_3$ is to use metal-organic CVD (MOCVD). The MOCVD growth of β-Ga_2O_3 and β-$(Al_xGa_{1-x})_2O_3$ has been dramatically improved in the very recent years, yielding the much better electric properties than those grown by MBE. Although MOCVD has not accomplished the phase controlled growth of α-$(Al_xGa_{1-x})_2O_3$, it can be solved by selecting the proper substrate or growth condition. In addition to the growth method, the reduction of the dislocation density in α-$(Al_xGa_{1-x})_2O_3$ is crucial since materials with larger bandgaps is expected to be more sensitive to defects. The buffer layer and the epitaxial lateral overgrowth technology are useful to grow α-$(Al_xGa_{1-x})_2O_3$ with lower dislocation densities as well as α-Ga_2O_3.

- **Growth of high quality α-Ga_2O_3 bulk:** The enhancement of the phase transition temperature of α-Ga_2O_3 on sapphire was shown by decreasing the film thickness in this study. The result suggested the possibility that less strain in α-Ga_2O_3 enhances the thermal stability. However, the intrinsic phase transition temperature of α-Ga_2O_3 has not been revealed because of the heteroepitaxial growth of α-Ga_2O_3 on sapphire. For the growth of α-Ga_2O_3 on sapphire, the residual strain in α-Ga_2O_3 cannot be completely removed at high temperature due to the difference in the thermal expansion coefficient between α-Ga_2O_3 and sapphire. In order to reveal the intrinsic characteristic of α-Ga_2O_3, high purity α-Ga_2O_3 bulk is essential. The ELO α-Ga_2O_3 is a promising way, but one has to care strain in the ELO α-Ga_2O_3 originated from the distribution of dislocations

and coalescence of facets. Therefore, the residual stress is needed to be reduced by using a low temperature grown buffer layers or strained super lattice buffer layers. The high quality α-Ga_2O_3 bulk is also helpful to understand the other intrinsic properties of α-Ga_2O_3 such as mobility, breakdown field, heat capacity, and so on.

List of Publications

A. Full Length Papers and Letters

1) ◦Riena Jinno, Takayuki Uchida, Kentaro Kaneko, and Shizuo Fujita
"*Control of Crystal Structure of Ga_2O_3 on Sapphire Substrate by Introduction of α-$(Al_xGa_{1-x})_2O_3$ buffer layer*", Physica Status Solidi B 225, 1700326-1-5 (2018)

2) ◦Riena Jinno, Takayuki Uchida, Kentaro Kaneko, and Shizuo Fujita
"*Reduction in edge dislocation density in corundum-structured α-Ga_2O_3 layers on sapphire substrates with quasi-graded α-$(Al,Ga)_2O_3$ buffer layers*", Applied Physics Express **9**, 071101-1-4 (2016)

3) ◦Riena Jinno, Nobuhiro Yoshimura, Kentaro Kaneko, and Shizuo Fujita
"*Enhancement of Epitaxial Lateral Overgrowth in the Mist Chemical Vapor Deposition of α-Ga_2O_3 by Using A-Plane Sapphire Substrate*", Japanese Journal of Applied Physics **58**, 120912 (2019)

4) ◦Riena Jinno, Celesta Chang, Yongjin Cho, Kevin Lee, Vladimir Protasenko, David A. Muller, Huili Grace Xing, and Debdeep Jena,
"*α-$(Al,Ga)_2O_3$ on m-plane Sapphire Substrates by Plasma-Assisted MBE"* (to be submitted)

5) ◦Riena Jinno, Shu Takemoto, Kentaro Kaneko, and Shizuo Fujita
"*Fabrication of α-Ga_2O_3 using carbon-free precursor by mist CVD method*" (to be submitted)

6) ◦Riena Jinno, Yasutaka Masuda, Kentaro Kaneko, and Shizuo Fujita
"*Phase Transition Temperature of α-Ga_2O_3 Films on Sapphire Substrates*" (to be submitted)

Related papers

7) ◦Kentaro Kaneko, Takeyoshi Onuma, Keiichi Tsumura, Takayuki Uchida, Riena Jinno, Tomohiro Yamaguchi, Tohru Honda, and Shizuo Fujita
"*Growth of rocksalt-structured $Mg_xZn_{1-x}O$ (x> 0.5) films on MgO substrates and their deep-ultraviolet luminescence*", Applied Physics Express **9**, 111102 (2016)

8) º Takayuki Uchida, Riena Jinno, Shu Takemoto, Kentaro Kaneko, Shizuo Fujita
"*Evaluation of band alignment of α-Ga_2O_3/α-$(Al_xGa_{1-x})_2O_3$ heterostructures by X-ray photoelectron spectroscopy*", Japanese Journal of Applied Physics, **57**, 040314 (2018)

B. International Conferences

1) ◦Riena Jinno, Celesta S. Chang, Yongjin Cho, Kevin Lee, Vladimir Protasenko, David A. Muller, Huili Grace Xing and Debdeep Jena,
"Single-Phase α-$(Al_xGa_{1-x})_2O_3$ Films Grown on m-Plane Sapphire Substrates by Plasma-Assisted Molecular Beam Epitaxy", 3rd International Workshop Gallium Oxide and Related Materials, #EPI3-4, Ohio, USA August 2019 (oral)

2) ◦Riena Jinno, Nobuhiro Yoshimura, Kentaro Kaneko, and Shizuo Fujita,
"Epitaxial Lateral Overgrowth *of α-Ga_2O_3 on Sapphire Substrates*", Materials Research Society Fall Meeting, #EP08.10.16, Boston, USA, November 2018 (oral)

3) ◦Riena Jinno, Kentaro Kaneko, and Shizuo Fujita,
"Phase Transition Temperature of α-Ga_2O_3 on Sapphire Substrate", 45th International Symposium on Compound Semiconductors, #Fr1PP-Ga, Boston, June 2018 (poster)

4) ◦Riena Jinno, Takayuki Uchida, Kentaro Kaneko, and Shizuo Fujita
"*Growth behavior of Ga_2O_3 on sapphire substrate by controlling interface*",
Materials Research Society Fall Meeting, #EM04.10.09, Boston, USA, November 2017 (oral)

5) ◦Riena Jinno, Takayuki Uchida, Kentaro Kaneko, and Shizuo Fujita
"*Fabrication of α-$(Al_xGa_{1-x})_2O_3$ using carbon-free precursor by the mist CVD method*",
Materials Research Society Fall Meeting, #EM04.09.06, Boston, USA, November 2017 (poster)

6) ◦Riena Jinno, Takayuki Uchida, Kentaro Kaneko, and Shizuo Fujita
"*Control of crystallographic structure of Ga_2O_3 on sapphire*",
2nd International Workshop Gallium Oxide and Related Materials, #P94, Parma, Italy, September 2017 (poster)

7) ◦Riena Jinno, Takayuki Uchida, Kentaro Kaneko, and Shizuo Fujita
"*Control of Ga_2O_3 crystal structure on sapphire substrates by introducing α-$(Al_xGa_{1-x})_2O_3$ buffer Layers*",
44th International Symposium on Compound Semiconductors, #A2.3, Berlin, May 2017 (oral)

8) ◦Riena Jinno, Takayuki Uchida, Kentaro Kaneko, and Shizuo Fujita
"*Fabrication of α-Ga_2O_3 using carbon-free precursor by the mist CVD method*",
44th International Symposium on Compound Semiconductors, #P2.58, Berlin, May 2017 (poster)

9) ◦Riena Jinno, Takayuki Uchida, Kentaro Kaneko, and Shizuo Fujita,
"*Fabrication of α-Ga_2O_3 thin films using α-$(Al_xGa_{1-x})_2O_3$ multi buffer layers and its crystal structure properties*"
Pacific Rim Meeting on Electrochemical and Solid-State Science (PRiME), #2063, Hawaii, October 2016 (oral)

10) ◦Riena Jinno, Takayuki Uchida, Kentaro Kaneko, and Shizuo Fujita
"*Fabrication of α-Ga_2O_3 Thin Films Using α-$(Al_xGa_{1-x})_2O_3$ Buffer Layers and its Crystal Structure Properties*", 43rd International Symposium on Compound Semiconductors, #TuC2-3, Toyama, June 2016 (oral)

Awards

1) IWGO Best Student Paper Award (August, 2019)
   The 3rd International Workshop on Gallium Oxide and Related Materials, Ohio, USA, August 2019

2) EMS Award (November, 2017)
   The 36th Electronic Materials Symposium, Shiga, Japan, November 2017

3) Young Scientist Presentation Award (September, 2017)
   The 42th JSPS (Japan Society of Applied Physics) Spring Meeting 2017, Kanagawa, Japan, March 2017

4) The Best Student Presentation Award (February,2017)
   Research Meeting of Semiconductor Electronics Committee, JSMS (Society of Materials Science, Japan), Tottori, Japan, January 2017

5) Best Symposium Paper Award (November, 2016)
   PRiME (Pacific Rim Meeting on Electrochemical and Solid-State Science) 2016, Hawaii, USA, October 2016